ION SEPARATIONS BASED ON ELECTRICAL POTENTIALS NANOPOROUS AND MICROPOROUS MEMBRANES

By

Jason Armstrong

A DISSERTATION

Submitted to
Michigan State University
in partial fulfillment of the requirements
for the degree of

Chemistry—Doctor of Philosophy

2015

ABSTRACT

ION SEPARATIONS BASED ON ELECTRICAL POTENTIALS IN NANOPOROUS AND MICROPOROUS MEMBRANES

By

Jason Armstrong

This dissertation examines several types of ion separations in nanometer to micrometer pores in membranes. Membranes provide an attractive platform for ion separations, primarily because they operate continuously (i.e. not in a batch mode), and small pores offer the potential for ion separation based on charge and electrophoretic mobility differences. Initial studies employed charged, nanoporous membranes to separate monovalent and divalent ions. Adsorption of polyelectrolyte multilayers in nanoporous membranes afforded control over the surface charge and pore radii in track-etched membranes, and electrostatic ion-exclusion, particularly for divalent ions, occurred in these membranes because the electrical double layer filled the entire nanopore. Initial experiments employed adsorption of (PSS/PAH) multilayers in the 50-nm diameter pores of PCTE membranes to give a K^+/Mg^{2+} selectivity of ~10 in pressure-driven dead-end filtration. Adsorption of $(PSS/PAH)_1$ films in 30-nm pores gave a similar K^+/Mg^{2+}selectivity with a simpler modification procedure.

Separations utilizing $(PSS/PAH)_1$ films in 30-nm pores showed the lowest ion rejections with high ion concentrations, consistent with enhanced screening of the electrical double layer at high ionic strength. However, solutions with < 5 mM ionic strength exhibited essentially 100% Mg^{2+} rejections (the Mg^{2+} concentration in the permeate was below the method detection limit). Moreover, K^+ rejections increased in the presence of Mg^{2+}, which may stem from Mg^{2+}-adsorption within the PEM and increased surface charge. Finally, separation of Br^- and SO_4^{2-} with a PSS_1-modified, 30-nm PCTE membrane validated the exclusion mechanism for anions.

The average Br^-/SO_4^{2-} selectivity was 3.4 ± 0.8 for a solution containing 0.5 mM NaBr and 0.5 mM Na_2SO_4. The low selectivity in this case likely stems from a relatively large pore.

The membranes used for the separation of monovalent and divalent ions also facilitated separation of monovalent ions (e.g. Li^+ and Cs^+), via a streaming-potential mechanism. In these separations, flow through a negatively charged membrane yields a positive (permeate minus feed) streaming potential, which retards the transport of a more mobile cation to a greater extent than transport of a less mobile cation. Thus, $(PSS)_1$-modified, 30-nm PCTE membranes enabled Li^+ and Cs^+ separation, whereas $(PSS\text{-}PAH)_1$-modified membranes separated $acetate^-$ and Br^-. Cation slectivities were ~3 for solutions containing 1.5 mM Li_2SO_4 and 1.5 mM Cs_2SO_4, whereas anion selectivities were ~6 for 0.5 mM $Mg(Acetate)_2$, 0.5 mM $MgBr_2$. The streaming potential method gave only modest selectivities, however, and required low ion concentrations.

Electrical potentials applied across microporous glass membranes also facilitate separation of monovalent ions with different electrophoretic mobilities. This dissertation describes a filtration cell with porous electrodes to enable cross-flow filtration with an applied potential. With the appropriate potentials, the cell afforded some separation of K^+ and Li^+, but the average selectivities were ~3. Moreover, the rejection of both ions plateaued near 90% at sufficiently high current to flow rate ratios. Buffer depletion or nonuniform cross-flow and electric fields may lead to membrane areas with low rejection and prevent high selectivities. Fabrication of a dual cross-flow cell (cross-flow on feed and permeate sides) limits buffer depletion issues and may provide higher monovalent ion selectivities.

Copyright by
JASON ARMSTRONG
2015

For Emilia and Sam

ACKNOWLEDGEMENTS

The work presented herein would not have been possible without the guidance of my advisor, Merlin Bruening. Aside from providing simple suggestions, Professor Bruening has served as my mentor through the many facets of science outside the realm of research (writing, presenting, teaching, etc.). I also wish to thank my committee members for their numerous contributions to my research. Whether it was Professor Tarabara explaining a complex equation, Professor Blanchard giving a sterling lecture on surface science, or Professor Spence discussing 3D-printing, I have gained something valuable from my interactions with the committee members. Though I didn't have the pleasure of working with Professor Greg Baker for an extended period of time, I am sure it is my loss.

In addition to professorial guidance, I must acknowledge the teachings of the graduate students that have since graduated from the Bruening group, particularly Seth Hogg and Chao Cheng. I am fortunate to have had our graduate careers overlap by several years, and have benefited enormously. I also appreciate the contributions of various labmates for their fruitful discussions and suggestions. Much thanks to Yanlyang Pan (ERC lab manager), Scott Bankroff (glassblower), and especially Glenn Wesley (for his help in designing and fabricating numerous cells, electrodes, and membranes).

Last, but certainly not least, I owe half of the degree to my wife Jon'elle (You can have the Ph). Without her proofreading, suggestions, and wisdom, I would never have made it this far. I must also give a special thanks to my kids, Sam and Milly; without your entropy this dissertation would have been completed weeks earlier.

TABLE OF CONTENTS

LIST OF TABLES

LIST OF FIGURES

KEY TO ABBREVIATIONS

AA	Atomic absorption spectroscopy
AE	Atomic emission spectroscopy
α_y^x	Transport selectivity of ion *x* over ion *y*
c_x	Concentration of ion *x*
D_x	Diffusion coefficient of ion *x*
DCF	Dual cross-flow
IC	Ion chromatography
ICP-OES	Inductively-coupled plasma-optical emission spectroscopy
J_x	Flux of ion *x*
LbL	Layer-by-layer deposition (of PEM films)
PAH	Protonated poly(allylamine)
PCTE	Polycarbonate track-etched membranes
PE	Polyelectrolyte
PEM	Polyelectrolyte multilayer
PSS	Poly(sodium 4-styrenesulfonate)
R_x	Percent rejection of ion *x*
SEM	Scanning electron microscopy
μ_x	Electrical mobility of ion *x* in solution
ν_x	Electrophoretic velocity of ion *x* in solution

Chapter 1: Introduction

Portions of this chapter are being reproduced from JA Armstrong, EEL Bernal, AE Yaroshchuk, and ML Bruening. *Langmuir*, 29 (32), 10287-10296 (2013).

1.1. Membrane-based ion separations and a niche for charged nanopores

Membranes with small (i.e. nm to μm diameters), electrically charged pores provide a unique framework for separating ions. The separations reported herein exploit charge and electrophoretic mobility differences between ions, rather than size-exclusion, to preferentially transport a specific ion through membranes with small cylindrical pores.[1, 2] Improving the separation of ions is critical to many endeavors, such as preconcentration of biological samples,[3-5] isotope separations,[6] water softening,[7-9] salt recovery,[10-14] and desalination.[15-18] Although there are many ion-separation schemes, membrane-based techniques present viable alternatives to traditional methods such as precipitation and ion-exchange, primarily because membrane-based separations operate continuously.

Reverse osmosis,[19, 20] electrodialysis,[21-23] and nanofiltration[7, 9, 17, 24-28] are established, industrial-scale ion-removal techniques that employ membranes to produce potable water.[29-34] Reverse osmosis utilizes dense, nonporous membranes to reject nearly all salt ions,[19, 20] whereas nanofiltration employs membranes with nanometer-scale pores to preferentially reject divalent ions.[7, 16, 17, 19, 20, 29] In contrast, electrodialysis uses an electrical potential across a stack of ion-selective membranes (arranged parallel to the direction of flow), to remove ions from a salt solution.[21-23] Although all of these techniques effectively remove salt from water, they typically show modest selectivities among ions, especially among ions possessing the same charge (e.g. K^+ and Li^+).[9, 20, 35-39]

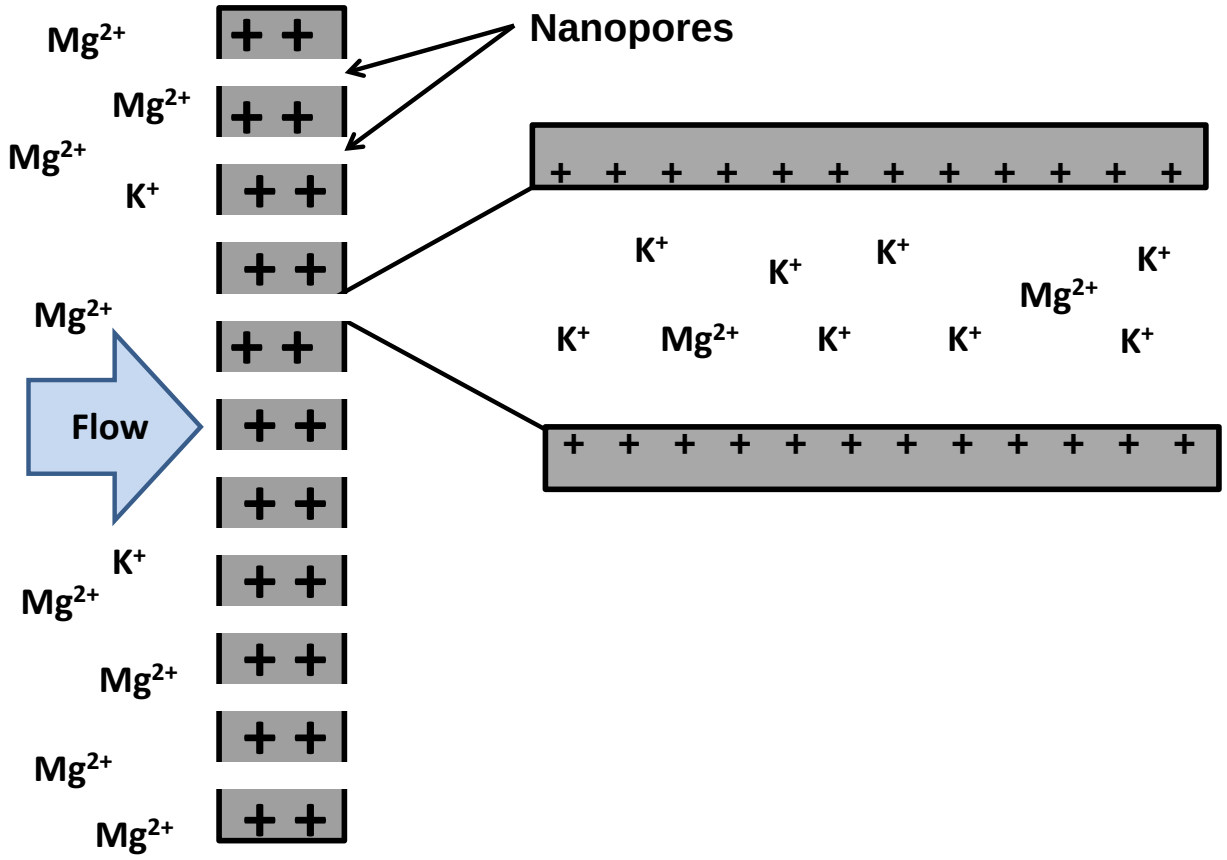

Figure 1.1. Separation of ions possessing different valence (anions omitted for clarity). The grey rectangle (left) represents a nanoporous membrane containing charged nanopores, and with convective flow occurring from left to right. The expanded view (right) represents a single nanopore. The positively charged nanopore excludes Mg^{2+} more than K^{+}, which gives rise to selective permeation of K^{+} over Mg^{2+}.

Small (i.e. nm-scale diameters), highly charged membrane pores can, in principle, separate monovalent and divalent ions via more extensive exclusion of divalent ions from the pore (Figure 1.1). The double-layer that results from surface charge excludes ions with the same sign of charge as the surface, and especially divalent ions. Separation of ions with the same charge is more difficult, and relies on differences in ion mobilities rather than charge. The streaming potential generated by convective transport of excess ions in the double-layer impedes ion transport, especially for highly mobile ions (Figure 1.2). Thus, porous membranes may show selectivities between ions with the same valence (e.g. acetate^{-} and Br^{-}, or K^{+} and Li^{+}), as well as

between mono- and divalent ions (e.g. K^+ and Mg^{2+}) (Figure 1.1). However, these separations require fine control over the size and charge of the nanopores. Such separations are attractive because porous membranes may achieve much higher permeabilities than dense membranes, such as those employed for reverse osmosis and nanofiltration. Additionally, the porous membrane may be more selective.

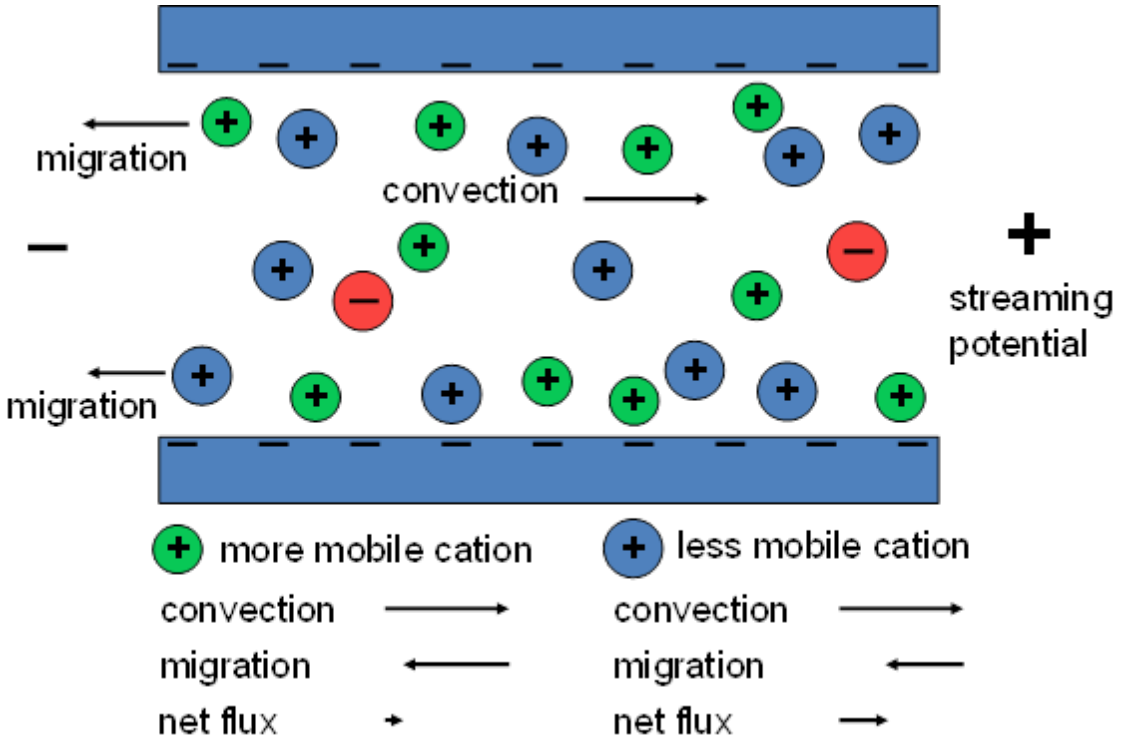

Figure 1.2. Separation of ions possessing the same valence, but different electrophoretic mobilities. The initial flow through the membrane gives rise to an excess of cations in the permeate (right side), which generates an electrical potential across the membrane (streaming potential). Convection brings Li^+ and K^+ ions to the membrane surface at the same rate, and transmembrane pressure causes the ions to transit the pore (left to right in the above diagram). In response to the streaming potential, electromigration of the more-mobile ion is greater than electromigration of the less-mobile ion, which results in a higher net flux for the less-mobile ion. Chapter 4 covers this mechanism in greater detail. This figure is taken from reference 41 with permission of the American Chemical Society.

This dissertation employs layer-by-layer (LbL) adsorption (Figure 1.3) of polyelectrolyte multilayers (PEMs) as a means of controlling the surface charge density and the diameter of the nanopores. These charged nanopores separate mono-/divalent ions, as well as monovalent ions.

Additionally, we employ countercurrent electrical potentials to control ion transport in membranes containing well-defined 5-μm pores. The sections below aim to put this work in perspective through a review of prior studies of charged nanopores for ion separations, layer-by-layer polyelectrolyte deposition in nanopores, and countercurrent electrophoresis.

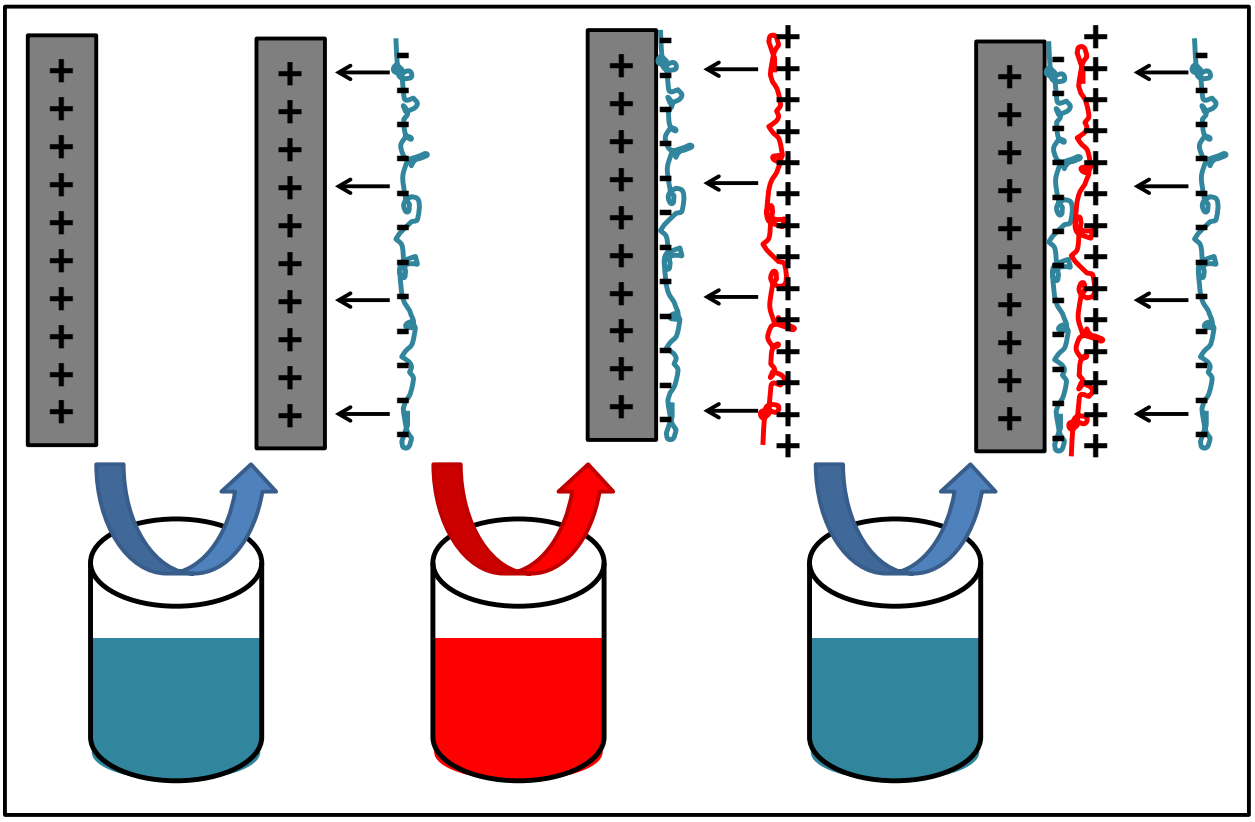

Figure 1.3. Layer-by-Layer (LbL) adsorption of polyelectrolyte multilayers (PEMs). A negatively charged polymer first adsorbs to the positively charged substrate (left). After a rinsing step (not shown), a positively charged polymer adsorbs to the previous, negatively charged layer. This process can be repeated as necessary to increase the film thickness and control the surface charge of the substrate.[40]

1.2. Charged nanoporous membranes for ion separations

Depending on the pore size, separations in nanopores can occur due to a combination of charge-based or size-based exclusion from pores.[41-45] In early studies, Martin and coworkers utilized porous alumina[46, 47] and PCTE membranes[48, 49] as sacrificial templates for growing various nm-scale structures.[50-55] In addition to forming these nanostructures, the Martin group plated Au into PCTE membrane pores to reduce the diameter from (nominal) 30 nm to 10 nm or even < 1 nm, depending on the plating time.[56, 57] Such membranes demonstrate selective ion transport via molecular size exclusion (< 1-nm diameter pores).[57] Adsorption of different charged thiols[56,57] further reduces pore size and introduces charge-based separation. L-cysteine-modified membranes exhibited pH-switchable transport selectivity, in which low pH causes preferential transport of large anions over large cations (both the amino and carboxyl groups of the cysteine are protonated, and small counterions pass through the membrane to maintain electrical neutrality). In contrast, high pH gives rise to preferential transport of large cations over large anions (the carboxyl groups of cysteine are deprotonated and the amino groups are neutral).[57] At pH 6, the isoelectric point of cysteine, there is no transport selectivity.[57] The same group also employed modified membranes to detect trace molecules[58-62] and to rectify current.[63-66]

Baker and colleagues fabricated membranes with single and multiple nanopores.[67, 68] Membranes containing a solitary conical nanopore provide a means for single molecule detection, as just one analyte molecule physically blocks the electrical current when that molecule passes through the nanopore.[68] In addition to single molecule detection,[69, 70] Siwy and coworkers showed that the conical nanopores exhibit current rectification (i.e. the magnitude of the current depends on the direction in which ions pass through the nanopore).[71-74] The

rectification phenomenon occurs because asymmetric ion concentration gradients within and just proximal to the nanopore generate regions of high and low conductivities. Cervera and coworkers studied the effects of pore geometry on current, and found that the smaller end of the conical nanopore affects ion transport more than the larger end.[75, 76] They also deposited (polystyrene sulfonate/polyallylamine) (PSS/PAH) PEMs within the conical pore of the current rectifier to govern surface charge and pore size, and explored the feasibility of conical nanopores as ion pumps using a periodic applied potential.[77]

Hollman and Bhattacharyya employed poly(L-lysine) (PLL) and poly(L-glutamic acid) (PLGA) films within 200-nm PCTE pores to reject Dextran and separate ions.[43] (PLL/PLGA) films within the pores were thicker than previous PEMs formed on flat substrates (33.4 nm[43] compared to 21.6 nm[78]). After deposition of a $(PLL/PLGA)_2$ film, the modified pores were ~63 nm in diameter, and these membranes demonstrated ~69% rejection of 482 kDa Dextran (~37-nm diameter).[43, 79] The authors also showed Cl^-/SO_4^{2-}-selectivities of 6.4-8.2 for single salt solutions containing 0.1-1.0 mM NaCl or Na_2SO_4.[43] These selectivities are remarkably high for such large pores. As mentioned, there is certainly a precedent for depositing PEMs in micro- and nanopores to affect ion transport; however, the work described in this dissertation aims to characterize, and then control ion transport in small pores to enable more difficult separations (e.g. separation of monovalent ions).

1.3. PEMs in nanopores

Layer-by-Layer (LbL) adsorption of PEM films occurs by exposing a surface to a series of polyelectrolyte and rinsing solutions.[40] The initial PE adsorbs to the charged surface through electrostatic or hydrophobic interactions,[80-83] and in the electrostatic case, the release of

counterions helps to drive the deposition.[84, 85] Rinsing removes loosely bound PE and exposure to a solution containing an oppositely charged PE leads to formation of a polyelectrolyte bilayer.[40, 86, 87] Subsequent bilayers adsorb in a similar manner, where each layer overcompensates (and reverses) the surface charge, thereby allowing further deposition.[84, 87] Multilayer adsorption can yield relatively thick films, and the choice of polyelectrolyte and deposition conditions can tailor film properties for specific applications.[43, 88-92] This section reviews prior work on characterizing PEM films within nanopores and comparing these films to those deposited on flat substrates.

Adsorption of PEMs in membrane pores provides a versatile method for controlling both surface charge and pore diameter. However, early work on modifying membranes with PEMs focused on coating the surfaces of membranes to create a selective skin for gas-separation,[93, 94] ion-separation,[95] or pervaporation membranes.[96] The Bruening group performed gas separations,[97] selective F^- removal from solutions also containing Cl^- and Br^-,[98] and separation of sugars[45] with a range of PEMs adsorbed on top of porous substrates. They reported deposition of $(PSS/PAH)_{10}$ PEMs on the surface of an alumina membrane with 20-nm pores, with minimal PEM intrusion into the alumina.[99] Several groups effectively separated organic solvents from water via pervaporation through PEM skins on membranes.[96, 100, 101] Further illustrating the diversity of PEMs, various studies used the films as enzyme-containing biocatalytic reactors,[102, 103] as a platform for ion separations,[41-43] and as templates for forming nanostructures (e.g. nanotubes, nanorods, etc.).[99, 104-107]

This dissertation focuses in part on modifying membrane pores, not just the membrane surface, and LbL adsorption in confined geometries is often quite different from adsorption without constraints. Rubner and coworkers explored the differences between PEMs deposited on

flat substrates and those adsorbed within the confined spaces of nanochannels on a hybrid micro-/nanofluidic device.[89] They demonstrated that PEMs are ~1.5 times thicker on either wafer surfaces or the tops of the nanochannels (unconfined) compared to PEMs within the ≤ 220-nm nanochannels (confined).[89] Their work provided insight into several factors that affect LbL adsorption: 1. Confined spaces (≤220 nm dimensions) give rise to less growth than unconfined regions, especially at low salt concentrations that lead to electrostatic repulsion of like-charged polyelectrolytes; 2. Size-based exclusion of 70 kDa poly(styrene sulfonate) (PSS) and 56 kDa poly(allylamine) (PAH) (0.1 M NaCl, pH 4) requires pore diameters < 15 nm; 3. Monitoring films in a wet state is essential to understanding geometric constraints because films may swell by ~300% in water.[89] Rubner and coworkers attributed the decreased thickness of their films within the nanochannels to depletion of unbound PE. They suggest that a repulsive potential develops within the nanochannel during adsorption of the initial polyelectrolyte and prevents further adsorption.[89]

In contrast to Rubner's work, an earlier study found that $(PSS/PAH)_x$ films in 400-nm and 800-nm polycarbonate track-etched (PCTE) membranes were thicker within the pores by 43% and 61% than films on the surface of the membrane and on silicon wafers, respectively.[90] This study attributes thicker films within the pores to incomplete rinsing (i.e. not all of the unbound/loosely bound polymer is removed) and capillary forces giving rise to an increased (local) concentration of polymer within the pore. The authors also noticed less swelling within the pores, and the observed swelling was took nearly an hour, compared to 3 minutes for swelling on a flat surface.[90] The difference in growth in these studies and those of Rubner (above) may stem from hindered PE transport in the smaller pores employed by Rubner.[89, 90]

Demoustier-Champagne and coworkers grew (poly(vinylbenzylammonium chloride) (PVBAC)/PSS)$_{10}$ PEMs by flowing PVBAC and PSS solutions through 50-850 nm PCTE pores.[108] The (PVBAC/PSS)$_{10}$ films completely plugged the nanopores, which they attributed to entanglement of the polymer chains within the confined geometries.[108] In a later study, the same group showed that two modes of growth occur inside 100-500 nm PCTE pores.[109] LbL adsorption in 100 nm-diameter pores quickly gave rise to nanowires (solid PEM structures), whereas 500 nm pores commonly showed the formation of nanotubes (hollow structures) upon membrane dissolution. Moreover, with an increasing number of bilayers, films within 500-nm pores appeared to have thickening walls instead of forming a solid structure.[109] LbL-adsorption in pores with 200-nm diameters gave both hollow and filled PEM nanotubes, while 100-nm and 200-nm pores also exhibited a higher dependence of film thickness on ionic strength, as well as on the molecular weight of the PE used for deposition.[109] The authors suggest a two regime growth mode: 1. The pore diameter is much larger than the polyelectrolyte radius of gyration, so growth within the pores is similar to unconfined growth (i.e. growth on a wafer or membrane surface); and 2. Chains on opposite sides of the pore begin to interconnect, trapping polymer chains flowing past and completely plugging the pore.[109] In addition, drying may shrink the film by ~40%,[110] which could explain why solid nanostructures do not always appear in SEM images after membrane dissolution.

Arsenault and coworkers used silica colloid photonic crystals to show that PEM thicknesses depend on both the geometry of the substrate, as well as the surface morphology.[111] PEM growth between the 270-nm microspheres was ~500% less than growth on top of the spheres, which they attributed to hindered diffusion of the PE between the microspheres.[111] Ai, et al. grew flexible (PSS/PAH) nanotubes in sacrificial, 200-nm alumina membranes, and found

a dry PEM thickness within the pore of 17-27 nm per (PSS/PAH) bilayer.[106] This thickness is drastically higher than the 3.8 ± 0.3 nm/bilayer observed with PEMs deposited under similar conditions on flat substrates.[112]

Lazzara and colleagues used *in-situ* optical waveguide spectroscopy (OWS) to investigate the growth of PEMs containing 4th-generation dendrimer in 30-117-nm alumina pores.[113] They demonstrated inhibition of film growth well in advance of steric exclusion.[113] For example, growth inside a 97-nm pore essentially plateaued after adsorption of 10 bilayers, which would give ~20 nm of film on a flat surface. This suggests that although the pore was still ~55 nm in diameter, the dendrimers (~7 nm diameter)[105] no longer deposited inside the pores, whereas PEM growth on the surface of the membrane proceeded in a linear fashion.[113] Film growth within the pore also was more sensitive to ionic strength than unconfined film growth.[113] They suggest that differences in thickness for PEMs grown on flat substrates and in nm-scale pores stem from entrance effects. The pore entrance quickly narrows upon exposure to PE, giving rise to an enhanced electrostatic repulsion that decreases the availability of PE within the pore .[113]

These studies clearly demonstrate the challenges in controlled adsorption of PEMs in nanopores. Polymer entanglements may cause pore plugging, particularly when flowing polyelectrolytes through the pore. In diffusive transport through pores, PE exclusion may limit adsorption to the pore surface. As chapter 3 shows, deposition only near the pore entrance may lead to high selectivities without greatly limiting permeability. An understanding of the physics governing LbL film growth in confined geometries is important for exploiting such films for ion separations.

1.4. Electrophoretic ion separations

In addition to employing PEM-modified nanopores for ion separations, my research examines whether applied potentials across a microporous glass membrane can separate ions through countercurrent electrophoresis (CcE). Traditional capillary electrophoresis (CE) employs a large potential (several kV) across a microcapillary, causing ions to migrate through the capillary according to their electrical mobility. Gobie and Ivory first described CcE in 1990.[114] This technique employs solution flow opposite to the electric field (countercurrent) to enhance selectivity.[115] In batch-mode, the countercurrent flow causes the ions to reside in the electric field for longer periods of time, providing higher resolution than traditional CE.[115-117] Moreover, in some cases the countercurrent flow affords continuous separations where the applied potential selectively excludes specific analytes from the capillary.[118, 119] Figure 1.4 illustrates the differences between CE and CcE. Because this work employs CcE using microporous membranes, this section provides an introduction to electrophoretic separations.

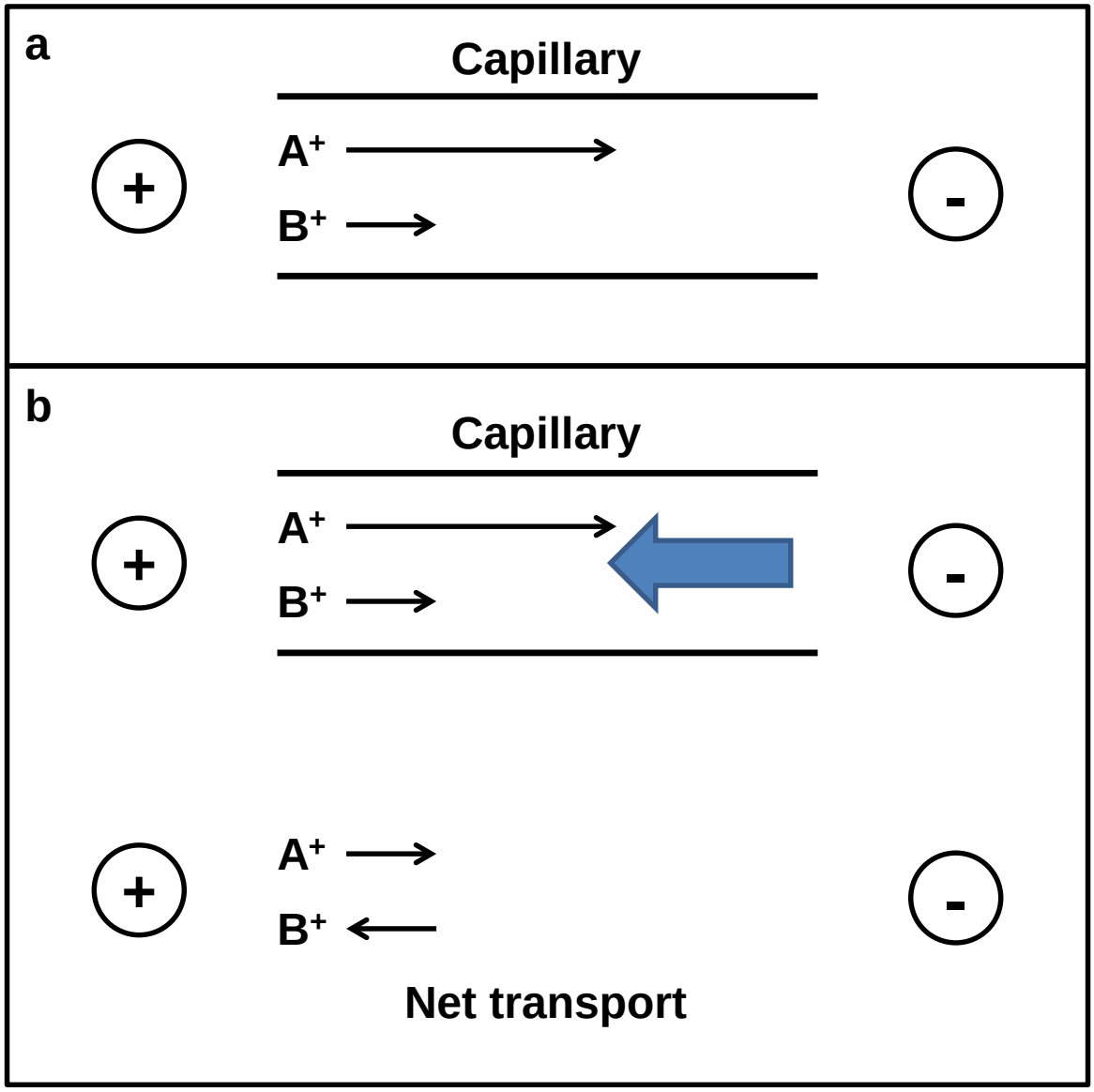

Figure 1.4. Vector representation of ion transport in (a) conventional CE and (b) CcE. The circles containing plus or minus signs indicate the polarity of the electrical potential. In CE (top diagram), ion A^+ separates from ion B^+ due to differences in their electrical mobilities (A^+ has a higher electrical mobility than B^+, and therefore moves faster in the electric field). In CcE, a flow (blue arrow) that opposes electrical migration forces the ions to reside in the capillary for an extended period of time, giving rise to higher resolutions. The vectors at the bottom of (b) reflect the effect of both flow and electromigration, which can lead to exclusion of the low-mobility ion, B^+ from the pore (adapted from B. Chankvetadze, et al., *Electrophoresis* 20(13), 2680-2685 (1999)).[116]

Applied electrical potentials across micro/nanoporous substrates have a long history in separation science. Jorgenson and coworkers pioneered the use of high-voltage (many kV) electrophoretic separations using silica capillaries with μm-scale diameters.[120, 121] They were

also instrumental in developing various coupled detection methods for CE,[122, 123] and were the first to use 2-dimensional LC-CE[124-127] and 3-dimensional SEC-LC-CE[128] to separate complex peptide mixtures (SEC-LC-CE is coupled size-exclusion chromatography-liquid chromatography-capillary electrophoresis). Coupling SEC upstream of LC-CE provides a molecular weight separation prior to entering the LC and CE columns. The LC separation occurs perpendicular to the CE separation, thus providing enhanced resolution.[124, 129, 130] In parallel with establishing multi-dimensional separation techniques, Culbertson and Jorgenson utilized CcE, which they call 'flow counterbalanced capillary electrophoresis,' to separate ions with electrical mobility differences of only 1 x 10^{-7} cm^2/s, an order of magnitude lower than electrical mobility differences that give rise to separations in CE.[115]

The Hayes group further developed 2-dimensional CcE techniques,[131] utilizing unique flow patterns and electric fields[132] to provide separation,[118, 133, 134] capture,[135, 136] and concentration of various biomolecules.[137, 138] For example, they selectively excluded charged dye molecules[118] and proteins[137] from a microcapillary in the presence of a countercurrent electric field, and adapted the technique to microfluidic chips.[139] Chen and coworkers utilized a homebuilt CcE instrument to exclude ions from a micropore and selectively passed individual amino acids through the pore while excluding others.[140] Chen's group also developed microfluidic chips for miniaturized electrophoresis.[141, 142]

1.5. Outline of this dissertation

This work has three aims: 1) assess the suitability of PEM-modified, nanoporous membranes for separating ions with different charges (e.g. K^+ and Mg^{2+}); 2) utilize these same membranes to separate ion of the same charge (e.g. Li^+ and Cs^+); and 3) develop new strategies

for high-throughput CcE using microporous membranes. Initially, I employed 30-nm and 50-nm pores in PCTE membranes to separate K^+ and Mg^{2+} or Br^- and SO_4^{2-} ions via electrostatic exclusion. Chapter 2 describes modification and characterization of PCTE membranes, and chapter 3 presents the ion separations. Examination of K^+/Mg^{2+} selectivities as a function of ionic strength along with modeling suggest that a narrow region near the pore inlet gives rise to selectivity. Chapter 4 describes monovalent ion separations that use the same membranes, but rely on streaming potentials to selectively slow the flux of more mobile ions. Although the monovalent separations showed selectivities of ~5, thereby validating the mechanism, concentration polarization at high flow rates will likely limit the utility of these separations.

Chapter 5 investigates whether a transmembrane potential can substitute for the streaming potential and lead to high selectivities in monovalent ion separations. These experiments employed a membrane consisting of fused glass capillaries with pore diameters of 5 μm and thicknesses of 2-3 mm. The relatively high diameter and thickness should make diffusion negligible compared to convection and enhance selectivities. However, ion rejection plateaus at high electric fields, so selectivities reach values only around 3. This limit in selectivity may arise from buffer depletion, concentration polarization, or nonuniformity of the electric field. In moving forward, our group will attempt to elucidate and overcome the factors that limit selectivity in these separations.

REFERENCES

REFERENCES

1. Tagliazucchi, M.; Calvo, E. J. *ChemPhysChem* **2010,** *11*, 2957-68.

2. Adusumilli, M.; Bruening, M. L. *Langmuir* **2009,** *25*, 7478-7485.

3. Lee, J. H.; Song, Y.-A.; Tannenbaum, S. R.; Han, J. *Analytical Chemistry* **2008,** *80*, 3198-3204.

4. Lee, J. H.; Song, Y.-A.; Han, J. *Lab on a Chip* **2008,** *8*, 596-601.

5. Kim, S. J.; Li, L. D.; Han, J. *Langmuir* **2009,** *25*, 7759-7765.

6. Whitworth, T. M.; Mariñas, B. J.; Fritz, S. J. *Journal of Membrane Science* **1994,** *88*, 231-241.

7. Cadotte, J.; Forester, R.; Kim, M.; Petersen, R.; Stocker, T. *Desalination* **1988,** *70*, 77-88.

8. Ouyang, L.; Malaisamy, R.; Bruening, M. L. *Journal of Membrane Science* **2008,** *310*, 76-84.

9. Rautenbach, R.; Gröschl, A. *Desalination* **1990,** *77*, 73-84.

10. Shu, L.; Waite, T. D.; Bliss, P. J.; Fane, A.; Jegatheesan, V. *Desalination* **2005,** *172*, 235-243.

11. Wadley, S.; Brouckaert, C. J.; Baddock, L. A. D.; Buckley, C. A. *Journal of Membrane Science* **1995,** *102*, 163-175.

12. Kim, D. H. *Desalination* **2011,** *270*, 1-8.

13. Estefan, S. F.; Awadalla, F. T.; Yousef, A. A. *Powder Technology* **1980,** *27*, 233-240.

14. Drioli, E.; Curcio, E.; Criscuoli, A.; Profio, G. D. *Journal of Membrane Science* **2004,** *239*, 27-38.

15. Kim, S. J.; Ko, S. H.; Kang, K. H.; Han, J. *Nature Nanotechnology* **2010,** *5*, 297-301.

16. Wang, D.-X.; Su, M.; Yu, Z.-Y.; Wang, X.-L.; Ando, M.; Shintani, T. *Desalination* **2005,** *175*, 219-225.

17. Bowen, W. R.; Mukhtar, H. *Journal of Membrane Science* **1996,** *112*, 263-274.

18. Levenstein, R.; Hasson, D.; Semiat, R. *Journal of Membrane Science* **1996,** *116*, 77-92.

19. Spiegler, K. S.; Kedem, O. *Desalination* **1966,** *1*, 311-326.

20. Fritzmann, C.; Löwenberg, J.; Wintgens, T.; Melin, T. *Desalination* **2007,** *216*, 1-76.

21. Amor, Z.; Bariou, B.; Mameri, N.; Taky, M.; Nicolas, S.; Elmidaoui, A. *Desalination* **2001,** *133*, 215-223.

22. Mani, K. N. *Journal of Membrane Science* **1991,** *58*, 117-138.

23. Melnik, L.; Vysotskaja, O.; Kornilovich, B. *Desalination* **1999,** *124*, 125-130.

24. Hong, S.; Elimelech, M. *Journal of Membrane Science* **1997,** *132*, 159-181.

25. Bowen, W. R.; Mohammad, A. W.; Hilal, N. *Journal of Membrane Science* **1997,** *126*, 91-105.

26. Van der Bruggen, B.; Schaep, J.; Wilms, D.; Vandecasteele, C. *Journal of Membrane Science* **1999,** *156*, 29-41.

27. Nyström, M.; Kaipia, L.; Luque, S. *Journal of Membrane Science* **1995,** *98*, 249-262.

28. Wang, X.-L.; Tsuru, T.; Nakao, S.-i.; Kimura, S. *Journal of Membrane Science* **1997,** *135*, 19-32.

29. Matsuura, T. *Desalination* **2001,** *134*, 47-54.

30. Sourirajan, S., *Reverse osmosis*. Academic Press: 1970.

31. Petersen, R. J. *Journal of Membrane Science* **1993,** *83*, 81-150.

32. Huang, C.; Xu, T.; Zhang, Y.; Xue, Y.; Chen, G. *Journal of Membrane Science* **2007,** *288*, 1-12.

33. Strathmann, H. *Desalination* **2010,** *264*, 268-288.

34. Childress, A. E.; Elimelech, M. *Journal of Membrane Science* **1996,** *119*, 253-268.

35. Tanaka, Y.; Moon, S.-H.; Nikonenko, V. V.; Xu, T. *International Journal of Chemical Engineering* **2012,** *2012*, 3.

36. Yeager, H. L.; Steck, A. *Journal of the Electrochemical Society* **1981,** *128*, 1880-1884.

37. Xu, T. *Journal of Membrane Science* **2005,** *263*, 1-29.

38. Simons, R. *Electrochimica Acta* **1984,** *29*, 151-158.

39. Verbrugge, M. W.; Hill, R. F. *Journal of the Electrochemical Society* **1990,** *137*, 886-893.

40. Decher, G. *Science* **1997,** *277*, 1232-1237.

41. Armstrong, J. A.; Bernal, E. E. L.; Yaroshchuk, A.; Bruening, M. L. *Langmuir* **2013,** *29*, 10287-10296.

42. Harris, J. J.; Stair, J. L.; Bruening, M. L. *Chemistry of Materials* **2000,** *12*, 1941-1946.

43. Hollman, A. M.; Bhattacharyya, D. *Langmuir* **2004,** *20*, 5418-5424.

44. Jin, W.; Toutianoush, A.; Tieke, B. *Applied Surface Science* **2005,** *246*, 444-450.

45. Liu, X.; Bruening, M. L. *Chemistry of Materials* **2003,** *16*, 351-357.

46. Foss, C. A.; Hornyak, G. L.; Stockert, J. A.; Martin, C. R. *The Journal of Physical Chemistry* **1994,** *98*, 2963-2971.

47. Gasparac, R.; Kohli, P.; Mota, M. O.; Trofin, L.; Martin, C. R. *Nano Letters* **2004,** *4*, 513-516.

48. Martin, C. R. *Science* **1994,** *266*, 1961-1966.

49. Maas, M.; Guo, P.; Keeney, M.; Yang, F.; Hsu, T. M.; Fuller, G. G.; Martin, C. R.; Zare, R. N. *Nano Letters* **2011,** *11*, 1383-1388.

50. C. Hulteen, J.; Martin, C. R. *Journal of Materials Chemistry* **1997,** *7*, 1075-1087.

51. Sapp, S. A.; Lakshmi, B. B.; Martin, C. R. *Template synthesis of bismuth telluride nanowires*; DTIC Document: 1998.

52. Sapp, S. A.; Mitchell, D. T.; Martin, C. R. *Chemistry of Materials* **1999,** *11*, 1183-1185.

53. Cepak, V. M.; Hulteen, J. C.; Che, G.; Jirage, K. B.; Lakshmi, B. B.; Fisher, E. R.; Martin, C. R. *Journal of Materials Research* **1998,** *13*, 3070-3080.

54. Cepak, V. M.; Martin, C. R. *The Journal of Physical Chemistry B* **1998,** *102*, 9985-9990.

55. Cepak, V. M.; Martin, C. R. *Chemistry of Materials* **1999,** *11*, 1363-1367.

56. Martin, C. R.; Nishizawa, M.; Jirage, K.; Kang, M.; Lee, S. B. *Advanced Materials* **2001,** *13*, 1351-1362.

57. Lee, S. B.; Martin, C. R. *Analytical Chemistry* **2001,** *73*, 768-775.

58. Kobayashi, Y.; Martin, C. R. *Analytical Chemistry* **1999,** *71*, 3665-3672.

59. Ugo, P.; Moretto, L. M.; Mazzocchin, G. A.; Guerriero, P.; Martin, C. R. *Electroanalysis* **1998,** *10*, 1168-1173.

60. Kececi, K.; Sexton, L. T.; Buyukserin, F.; Martin, C. R. *Nanomedicine* **2008,** *3*, 787-796.

61. Sexton, L.; Horne, L.; Martin, C., Biosensing with nanopores and nanotubes. In *Molecular- and nano-tubes*, Hayden, O.; Nielsch, K., Eds. Springer US: 2011; pp 165-207.

62. Martin, C. R.; Siwy, Z. S. *Science* **2007,** *317*, 331-332.

63. Siwy, Z. S.; Martin, C. R., Tuning ion current rectification in synthetic nanotubes. In *Controlled nanoscale motion*, Linke, H.; Månsson, A., Eds. Springer Berlin Heidelberg: 2007; Vol. 711, pp 349-365.

64. Choi, Y.; Baker, L. A.; Hillebrenner, H.; Martin, C. R. *Physical Chemistry Chemical Physics* **2006,** *8*, 4976-4988.

65. Harrell, C. C.; Siwy, Z. S.; Martin, C. R. *Small* **2006,** *2*, 194-198.

66. Jin, P.; Mukaibo, H.; Horne, L. P.; Bishop, G. W.; Martin, C. R. *Journal of the American Chemical Society* **2010,** *132*, 2118-2119.

67. Thakar, R.; Zakeri, R.; Morris, C. A.; Baker, L. A. *Analytical Methods* **2012,** *4*, 4353-4359.

68. Heins, E. A.; Siwy, Z. S.; Baker, L. A.; Martin, C. R. *Nano Letters* **2005,** *5*, 1824-1829.

69. Mara, A.; Siwy, Z.; Trautmann, C.; Wan, J.; Kamme, F. *Nano Letters* **2004,** *4*, 497-501.

70. Howorka, S.; Siwy, Z. *Chemical Society Reviews* **2009,** *38*, 2360-2384.

71. Siwy, Z. S. *Advanced Functional Materials* **2006,** *16*, 735-746.

72. Vlassiouk, I.; Siwy, Z. S. *Nano Letters* **2007,** *7*, 552-556.

73. Siwy, Z.; Heins, E.; Harrell, C. C.; Kohli, P.; Martin, C. R. *Journal of the American Chemical Society* **2004,** *126*, 10850-10851.

74. Siwy, Z.; Apel, P.; Baur, D.; Dobrev, D. D.; Korchev, Y. E.; Neumann, R.; Spohr, R.; Trautmann, C.; Voss, K.-O. *Surface Science* **2003,** *532–535*, 1061-1066.

75. Ramírez, P.; Apel, P. Y.; Cervera, J.; Mafé, S. *Nanotechnology* **2008,** *19*, 315707.

76. Ali, M.; Yameen, B.; Cervera, J.; Ramírez, P.; Neumann, R.; Ensinger, W.; Knoll, W.; Azzaroni, O. *Journal of the American Chemical Society* **2010,** *132*, 8338-8348.

77. Cervera, J.; Ramirez, P.; Mafe, S.; Stroeve, P. *Electrochimica Acta* **2011,** *56*, 4504-4511.

78. Lavalle, P.; Gergely, C.; Cuisinier, F. J. G.; Decher, G.; Schaaf, P.; Voegel, J. C.; Picart, C. *Macromolecules* **2002,** *35*, 4458-4465.

79. Hagel, L., Chapter 5 pore size distributions. In *Journal of Chromatography Library*, Dubin, P. L., Ed. Elsevier: 1988; Vol. Volume 40, pp 119-155.

80. Lorena Cortez, M.; De Matteis, N.; Ceolin, M.; Knoll, W.; Battaglini, F.; Azzaroni, O. *Physical Chemistry Chemical Physics* **2014,** *16*, 20844-20855.

81. Bain, C. D.; Claesson, P. M.; Langevin, D.; Meszaros, R.; Nylander, T.; Stubenrauch, C.; Titmuss, S.; von Klitzing, R. *Advances in Colloid and Interface Science* **2010,** *155*, 32-49.

82. Schlenoff, J. B.; Rmaile, A. H.; Bucur, C. B. *Journal of the American Chemical Society* **2008,** *130*, 13589-13597.

83. Bucur, C. B.; Sui, Z.; Schlenoff, J. B. *Journal of the American Chemical Society* **2006,** *128*, 13690-13691.

84. Glinel, K.; Jonas, A. M.; Laschewsky, A.; Vuillaume, P. Y., Internally structured polyelectrolyte multilayers. In *Multilayer Thin Films*, Wiley-VCH Verlag GmbH & Co. KGaA: 2003; pp 177-205.

85. Joanny, J.-F.; Castelnovo, M., Polyelectrolyte adsorption and multilayer formation. In *Multilayer Thin Films*, Wiley-VCH Verlag GmbH & Co. KGaA: 2003; pp 87-97.

86. Rubner, M. F., Ph-controlled fabrication of polyelectrolyte multilayers: Assembly and applications. In *Multilayer Thin Films*, Wiley-VCH Verlag GmbH & Co. KGaA: 2003; pp 133-154.

87. Schlenoff, J. B., Charge balance and transport in polyelectrolyte multilayers. In *Multilayer Thin Films*, Wiley-VCH Verlag GmbH & Co. KGaA: 2003; pp 99-132.

88. Mendelsohn, J. D.; Barrett, C. J.; Chan, V. V.; Pal, A. J.; Mayes, A. M.; Rubner, M. F. *Langmuir* **2000,** *16*, 5017-5023.

89. DeRocher, J. P.; Mao, P.; Han, J.; Rubner, M. F.; Cohen, R. E. *Macromolecules* **2010,** *43*, 2430-2437.

90. Lee, D.; Nolte, A. J.; Kunz, A. L.; Rubner, M. F.; Cohen, R. E. *Journal of the American Chemical Society* **2006,** *128*, 8521-8529.

91. Hollman, A. M.; Bhattacharyya, D. *Langmuir* **2002,** *18*, 5946-5952.

92. Ouyang, L.; Dotzauer, D. M.; Hogg, S. R.; Macanás, J.; Lahitte, J.-F.; Bruening, M. L. *Catalysis Today* **2010,** *156*, 100-106.

93. van Ackern, F.; Krasemann, L.; Tieke, B. *Thin Solid Films* **1998,** *327–329*, 762-766.

94. Quinn, R.; Laciak, D. V. *Journal of Membrane Science* **1997,** *131*, 49-60.

95. Krasemann, L.; Tieke, B. *Langmuir* **1999,** *16*, 287-290.

96. Krasemann, L.; Toutianoush, A.; Tieke, B. *Journal of Membrane Science* **2001,** *181*, 221-228.

97. Sullivan, D. M.; Bruening, M. L. *Chemistry of Materials* **2002,** *15*, 281-287.

98. Hong, S. U.; Malaisamy, R.; Bruening, M. L. *Langmuir* **2007,** *23*, 1716-1722.

99. Lee, D.; Cui, T. *Langmuir* **2011,** *27*, 3348-3354.

100. Lenk, W.; Meier-Haack, J. *Desalination* **2002,** *148*, 11-16.

101. Richau, K.; Schwarz, H. H.; Apostel, R.; Paul, D. *Journal of Membrane Science* **1996,** *113*, 31-41.

102. Wang, Y.; Yu, A.; Caruso, F. *Angewandte Chemie* **2005,** *117*, 2948-2952.

103. Wang, Y.; Caruso, F. *Chemistry of Materials* **2006,** *18*, 4089-4100.

104. Donath, E.; Sukhorukov, G. B.; Caruso, F.; Davis, S. A.; Möhwald, H. *Angewandte Chemie International Edition* **1998,** *37*, 2201-2205.

105. Kim, B.-S.; Lebedeva, O. V.; Kim, D. H.; Caminade, A.-M.; Majoral, J.-P.; Knoll, W.; Vinogradova, O. I. *Langmuir* **2005,** *21*, 7200-7206.

106. Ai, S.; Lu, G.; He, Q.; Li, J. *Journal of the American Chemical Society* **2003,** *125*, 11140-11141.

107. Sukhishvili, S. A. *Current Opinion in Colloid & Interface Science* **2005,** *10*, 37-44.

108. Alem, H.; Blondeau, F.; Glinel, K.; Demoustier-Champagne, S.; Jonas, A. M. *Macromolecules* **2007,** *40*, 3366-3372.

109. Roy, C. J.; Dupont-Gillain, C.; Demoustier-Champagne, S.; Jonas, A. M.; Landoulsi, J. *Langmuir* **2009,** *26*, 3350-3355.

110. Lösche, M.; Schmitt, J.; Decher, G.; Bouwman, W. G.; Kjaer, K. *Macromolecules* **1998,** *31*, 8893-8906.

111. Arsenault, A. C.; Halfyard, J.; Wang, Z.; Kitaev, V.; Ozin, G. A.; Manners, I.; Mihi, A.; Míguez, H. *Langmuir* **2004,** *21*, 499-503.

112. Harris, J. J.; Bruening, M. L. *Langmuir* **1999,** *16*, 2006-2013.

113. Lazzara, T. D.; Lau, K. H. A.; Abou-Kandil, A. I.; Caminade, A.-M.; Majoral, J.-P.; Knoll, W. *ACS Nano* **2010,** *4*, 3909-3920.

114. Gobie, W. A.; Ivory, C. F. *Journal of Chromatography A* **1990,** *516*, 191-210.

115. Culbertson, C. T.; Jorgenson, J. W. *Analytical Chemistry* **1994,** *66*, 955-962.

116. Chankvetadze, B.; Burjanadze, N.; Bergenthal, D.; Blaschke, G. *Electrophoresis* **1999,** *20*, 2680-2685.

117. McLaren, D. G.; Chen, D. D. Y. *Electrophoresis* **2003,** *24*, 2887-2895.

118. Meighan, M. M.; Keebaugh, M. W.; Quihuis, A. M.; Kenyon, S. M.; Hayes, M. A. *Electrophoresis* **2009,** *30*, 3786-3792.

119. Kenyon, S. M.; Weiss, N. G.; Hayes, M. A. *Electrophoresis* **2012,** *33*, 1227-1235.

120. Jorgenson, J. W. *TrAC Trends in Analytical Chemistry* **1984,** *3*, 51-54.

121. Walbroehl, Y.; Jorgenson, J. W. *Journal of Microcolumn Separations* **1989,** *1*, 41-45.

122. Lewis, K. C.; Jorgenson, J. W.; Kaufman, S. L. *Journal of Capillary Electrophoresis* **1996,** *3*, 229-235.

123. Chen, C.; Jeffery, D.; Jorgenson, J. W.; Moseley, M. A.; Pollack, G. M. *Journal of Chromatography B: Biomedical Sciences and Applications* **1997,** *697*, 149-162.

124. Larmann, J. P.; Lemmo, A. V.; Moore, A. W.; Jorgenson, J. W. *Electrophoresis* **1993,** *14*, 439-447.

125. Lemmo, A. V.; Jorgenson, J. W. *Analytical Chemistry* **1993,** *65*, 1576-1581.

126. Bushey, M. M.; Jorgenson, J. W. *Analytical Chemistry* **1990,** *62*, 978-984.

127. Moore, A. W.; Jorgenson, J. W. *Analytical Chemistry* **1995,** *67*, 3448-3455.

128. Moore, A. W.; Jorgenson, J. W. *Analytical Chemistry* **1995,** *67*, 3456-3463.

129. Evans, C.; Jorgenson, J. *Analytical and Bioanalytical Chemistry* **2004,** *378*, 1952-1961.

130. Hooker, T. F.; Jorgenson, J. W. *Analytical Chemistry* **1997,** *69*, 4134-4142.

131. Shi, H.; Hood, K. A.; Hayes, M. T.; Stubbs, R. S. *Journal of Proteomics* **2011,** *75*, 339-351.

132. Hayes, M. A.; Ewing, A. G. *Analytical Chemistry* **1992,** *64*, 512-516.

133. Pysher, M. D.; Hayes, M. A. *Analytical Chemistry* **2007,** *79*, 4552-4557.

134. Kenyon, S. M.; Meighan, M. M.; Hayes, M. A. *Electrophoresis* **2011,** *32*, 482-493.

135. Staton, S. J.; Jones, P. V.; Ku, G.; Gilman, S. D.; Kheterpal, I.; Hayes, M. A. *Analyst* **2012,** *137*, 3227-9.

136. Jones, P.; Staton, S. R.; Hayes, M. *Analytical and Bioanalytical Chemistry* **2011,** *401*, 2103-2111.

137. Meighan, M. M.; Vasquez, J.; Dziubcynski, L.; Hews, S.; Hayes, M. A. *Analytical Chemistry* **2010,** *83*, 368-373.

138. Polson, N. A.; Savin, D. P.; Hayes, M. A. *Journal of Microcolumn Separations* **2000,** *12*, 98-106.

139. Kenyon, S. M.; Weiss, N. G.; Hayes, M. A. *Electrophoresis* **2012,** *33*, 10.1002/elps.201100622.

140. McLaren, D. G.; Chen, D. D. Y. *Analytical Chemistry* **2004,** *76*, 2298-2305.

141. Liu, C.; Luo, Y.; Maxwell, E. J.; Fang, N.; Chen, D. D. Y. *Analytical Chemistry* **2011,** *83*, 8208-8214.

142. Liu, C.; Luo, Y.; Maxwell, E. J.; Fang, N.; Chen, D. D. Y. *Analytical Chemistry* **2010,** *82*, 2182-2185.

Chapter 2: Depositing and characterizing layer-by-layer polyelectrolyte multilayer films in polycarbonate, track-etched, nanoporous membranes

Portions of this chapter are being reproduced from JA Armstrong, EEL Bernal, AE Yaroshchuk, and ML Bruening. *Langmuir*, 29 (32), 10287-10296 (2013). The work is a collaboration with the group of Andriy Yaroshchuk.

2.1 Introduction

Many studies examined the unconstrained growth of layer-by-layer (LbL) films on flat substrates.[1-3] However, the LbL deposition in this work is unusual, in that it occurs in two different geometric regimes: 1) unconfined- on top of a membrane, from the bulk solution;[4-7] and 2) confined- inside of a nano- or micro-scale cylindrical pore.[8, 9] The unconfined regime allows free diffusion of polymer to and from the bulk solution to the surface of the membrane, most likely resulting in quite uniform films. In contrast, PEM adsorption in confined geometries (nm to μm pores) may yield thicker layers, and non-uniform thicknesses (e.g. thicker films near the pore opening, as well as a thickness gradient along the length of the pore).[9] Chapter 1 reviewed previous studies of PEM formation in membranes pores. This chapter describes our efforts to characterize the thickness of PEMs in membrane pores through hydraulic permeability measurements and SEM imaging. These characterization approaches are complementary because membrane permeability depends on the thickness of swollen films and models of convection, whereas electron microscopy yields more direct information but occurs in a vacuum with dry films. Membrane characterization is vital for understanding the selective transport described in subsequent chapters.

2.2 Membrane modification

2.2.1 PEM adsorption

We deposited PEMs in and on nanoporous, polycarbonate track-etched (PCTE) membranes using the LbL method, which includes exposing a surface to alternating solutions of polycations and polyanions (Figure 2.1).[1] Typically, each layer overcompensates the opposing surface charge, thereby allowing further deposition.[10] Rinsing between deposition steps removes incompletely adsorbed polyelectrolyte (PE).

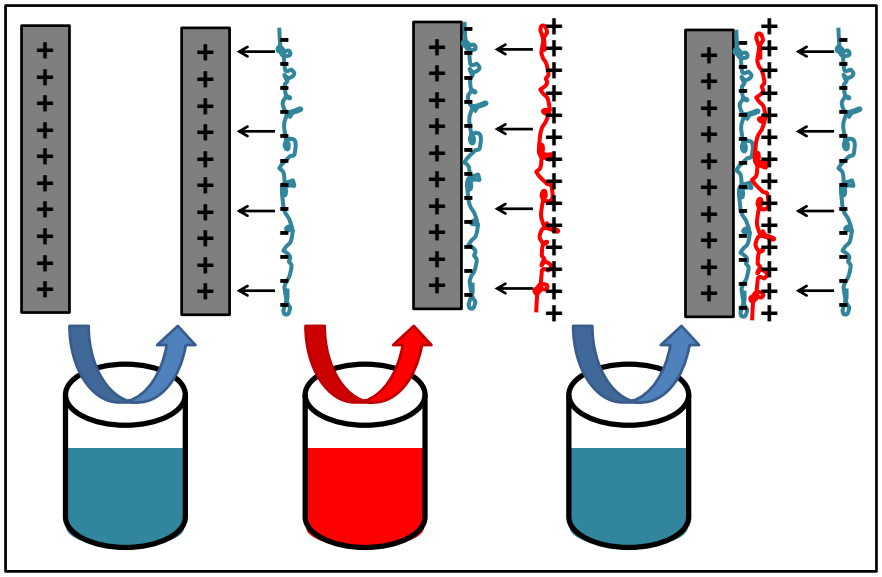

Figure 2.1. Alternating adsorption of polyanions and polycations on a substrate.[1] In this case, the polyanion electrostatically adsorbs to the positively charged surface. After a rinsing step, a polycation layer binds to the overcompensating negative charge, now present at the surface.[1] This process can be repeated to grow many bilayers of film. Note that the figure does not show the displacement of counterions that often drives adsorption of the extensive overlap that occurs between neighboring layers.

2.2.2 Materials, chemicals, and equipment

Nuclepore polycarbonate track-etched (PCTE) membranes with diameters of 25 mm and nominal pore sizes of 30 nm (cat. #110602) and 50 nm (cat. #110603) were purchased from Whatman. All solutions were prepared using deionized water (18.2 MΩ·cm, MilliQ). Solutions containing sodium poly(styrene sulfonate) (PSS, 70 kDa, Sigma-Aldrich) or protonated poly(allylamine) (PAH, 65 kDa, Sigma-Aldrich) in 1.0 M NaCl were adjusted to a pH of 4.5 using HCl and NaOH and subsequently filtered through 25 mm 0.45 μm membranes (Millipore, HNWP02500) prior to use. (Polymer concentrations are given with respect to the repeating unit.) An Amicon 8010 stirred cell (Millipore) connected to a stainless steel pressurized feed tank (Pope, Saukville, WI) was employed for both ion separations and modifications of PCTE membranes with polyelectrolyte films. During dead-end filtration of salt solutions, the magnetic bar in the Amicon cell was rotated using a Corning PC-420 stir plate to minimize concentration polarization, but stirring was not employed during polyelectrolyte adsorption. A steel microporous frit (Mott Corp., Farmington, CT, 1004170-01.020), which provides minimal resistance to flow, supported the membranes in the Amicon cell.

2.2.3 Layer-by-layer film deposition procedure

Prior to modification, the 30-nm PCTE membranes were mounted in the Amicon cell and compacted for 1 hour with deionized water at the highest pressures that would be employed during subsequent separations (210-414 kPa). The cell was emptied, and 3-4 mL of a solution containing 0.01 M PSS in 1.0 M NaCl at pH 4.5 was passed through the membrane at a flow rate of ~0.4 mL/min. PSS presumably adsorbs to polymer substrates via hydrophobic interactions, and our prior studies confirm PSS adsorption in bare polymer membranes.[11-13] Backflushing the membrane after PSS adsorption did not increase flow rate. Immediately after deposition of each

polyelectrolyte, the Amicon cell and membrane surface were rinsed with 40-60 mL of 1.0 M NaCl using a squirt bottle, and then 15-20 mL of 1.0 M NaCl was passed through the membrane to rinse the pores and remove loosely-bound polyelectrolyte. After rinsing, deposition of PAH occurred similarly (the deposition solution contained 0.01 M PAH in 1.0 M NaCl at pH 4.5). The pressures for polyelectrolyte depositions ranged from 70-350 kPa to maintain the ~0.4 mL/min flow rate because the membrane permeability decreased after polyelectrolyte adsorption. Modification of 50-nm PCTE membranes occurred at pressures of ~10-280 kPa, with 0.01 M polyelectrolyte in 0.5 M NaCl, and either deionized water or 0.5 M NaCl as rinsing solutions. These depositions used lower salt concentrations, which lead to lower film thicknesses that facilitate examination of selectivity as a function of pore size. The 50-nm membranes were not compacted prior to modification, and the rinse solution was not passed through the membrane. After modification, membranes were stored in Amicon cells filled with deionized water.

Prior to ion-transport experiments, 50-nm PCTE membranes were rinsed with deionized water from a squirt bottle. In the case of the 30-nm PCTE membranes, we also passed ~20 mL of deionized water through the membrane before examining ion transport. For subsequent separations, solutions containing different salt compositions were passed through the membrane under varying transmembrane pressures with continuous stirring.

2.3 Characterization of PEMs adsorbed in 50-nm PCTE membranes

2.3.1 Depositing multilayer PSS/PAH films to adjust the sizes of 50-nm pores in PCTE membranes

The well-defined, nearly cylindrical pores in polycarbonate track-etched (PCTE) membranes are attractive for fundamental studies of ion separations. Additionally, the low pore density (see Figure 2.2) limits solution flux to decrease concentration polarization effects. However, commercial vendors offer membranes with a limited range of pore diameters and no option for controlling the surface charge inside the pores. This research aims to vary both pore diameter and surface charge through adsorption of polyelectrolyte films, and in turn to control ion transport through these modified membrane pores.

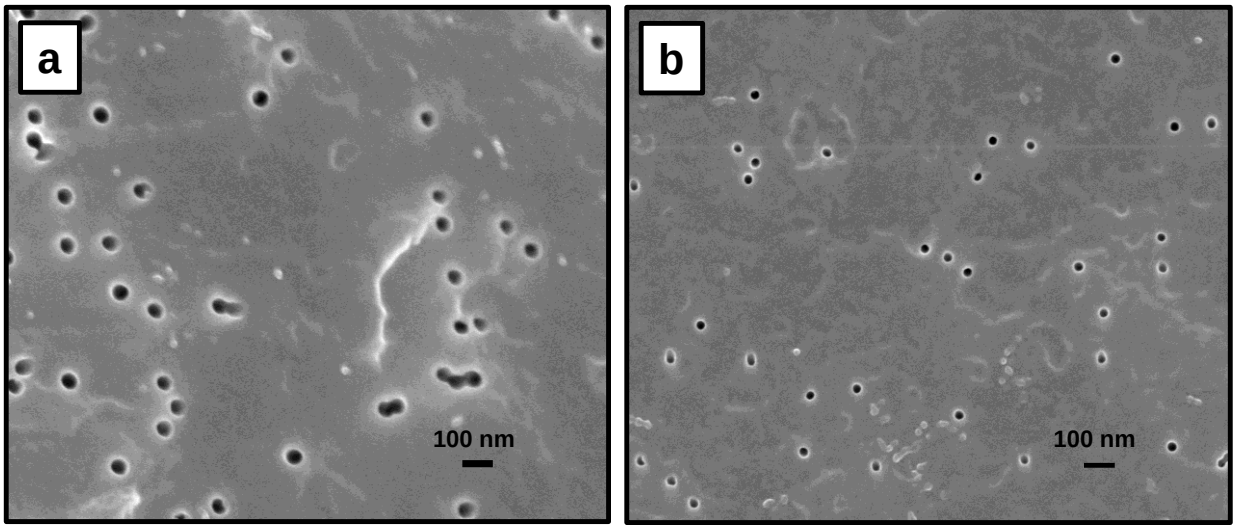

Figure 2.2. SEM images of track-etched polycarbonate membranes with nominal pore diameters of (a) 50 nm and 30 nm (b).

As mentioned in chapter 1, a number of studies examined modification of nanopores with PEMs. When using convection to force polyelectrolyte solutions through pores, films can be thicker than corresponding coatings on flat surfaces.[14] In an initial examination of $(PSS\text{-}PAH)_n$ deposition in nanopores, we modified the nominal 50-nm pores in PCTE membranes and examined flow rate as a function of the number of deposited layers. According to the Hagen-Poiseuille equation, the flow rate through a pore is proportional to the pore radius raised to the fourth power. Thus, we estimated the radii of the modified pores using Equation 2.1

$$r_2 = r_1 * \left(\frac{Q_2}{Q_1}\right)^{\frac{1}{4}} \quad (2.1)$$

where r_2 is the modified membrane's pore radius, r_1 is the bare membrane's pore radius, $Q_2$is the volumetric flow rate (normalized to the applied pressure) through the modified membrane, and Q_1 is the average volumetric flow rate (normalized to the applied pressure) determined from multiple measurements with 2 bare membranes.

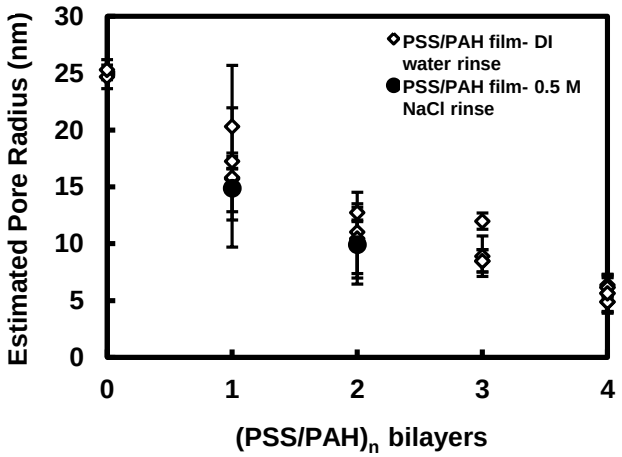

Figure 2.3. Average radii of pores in track-etched membranes (nominal 50 nm pores) before and after modification with $(PSS/PAH)_n$ bilayers, n=1-4. In membrane modification, rinsing occurred with either deionized (DI) water (open diamonds) or 0.5 M NaCl (filled circles). The radii were calculated with Equation 2.1 using solution fluxes normalized to the transmembrane pressure. Each symbol represents a different replicate membrane, and the error bars show the standard deviation of ~7 determinations of flow rate during passage of 0.5 mM $MgCl_2$, 0.5 mM KCl solutions through each membrane. The flux generally decreased with time.

Figure 2.3 shows the estimated pore radii for bare and $(PSS-PAH)_n$-modified PCTE membranes. We assumed that the average initial pore radius for several unmodified membranes was the nominal 25 nm. The average radius decreases monotonically with the number of adsorbed bilayers, and based on the decreases in pore radii, the thicknesses of the first and

second (PSS-PAH) bilayers are about 7 nm, whereas the combined thicknesses of the third and fourth bilayers are ~4-7 nm. The 7 nm thickness is for the initial bilayers is similar to prior measurements of PSS/PAH bilayer thicknesses on other substrates.[14] Less deposition in later bilayers is consistent with previous data that suggest that the surface charge decreases with the number of bilayers deposited in nanopores.[15] In fact, a 4-bilayer film with a thickness of 7 nm/bilayer cannot fit in a pore with a radius of 25 nm.

Several factors complicate these determinations of pore radius and film thickness. First, the pore density indicated by the membrane supplier is $(6.0 \pm 0.9) \times 10^{12}$ m^{-2}. However, a statistical analysis of 10 SEM images gave a ~30% higher pore density, $(7.9 \pm 1.2) \times 10^{12}$ m^{-2}. Using this latter value and the experimental hydraulic permeability of nominal 50 nm PCTE membranes ($(1.5 \pm 0.1) \times 10^{-9}$ m/(s Pa)), we calculate an average pore diameter of ~80 nm in the unmodified membrane. This is higher than both the manufacturer's stated value (45 ± 5 nm) and the average pore size in SEM images (~63 nm), perhaps because of a cigar-shaped pore geometry, as suggested previously.[16, 17] If we use 80 nm as the initial pore diameter, the thicknesses of $(PSS/PAH)_1$ and $(PSS/PAH)_2$ films would be 13 nm and 22 nm, respectively, or nearly twice the thickness values obtained by assuming the nominal diameter of 50 nm. In a few cases, we substituted a 0.5 M NaCl rinse for a deionized water rinse after deposition of each layer, as the rinse may affect the swelling of the outer layer.[18] Figure 2.3 suggests that changing the rinsing solution to 0.5 M NaCl may marginally increase the thickness of $(PSS/PAH)_1$ and $(PSS/PAH)_2$ films deposited in PCTE membranes, but the effect is not statistically significant.

As a second complication, the apparent increases in thickness after deposition of a PSS/PAH bilayer may reflect hydraulic resistance due to selective film adsorption near pore entrances (see chapter 3) or to a film that spans the pore surface. SEM images of membranes

modified with $(PSS/PAH)_2$ films suggest a >50% decrease in pore density compared to an unmodified membrane (Figure 2.4). Nevertheless, pores not visible in SEM images may still show hydraulic permeabilities similar to other pores if the film on the surface is thin enough to provide low hydraulic resistance. These membranes show minimal rejection of PAH during deposition of the second PSS/PAH bilayer, so at the very least nearly all flow goes through open pores. Finally, the image in Figure 2.4 shows some overlapping pores (indicated by red arrows), which could also affect calculations of average pore radii. However, Section 2.3.2 shows that the density of doublet pores is not sufficient to changed calculated pore radii by more than 2%.

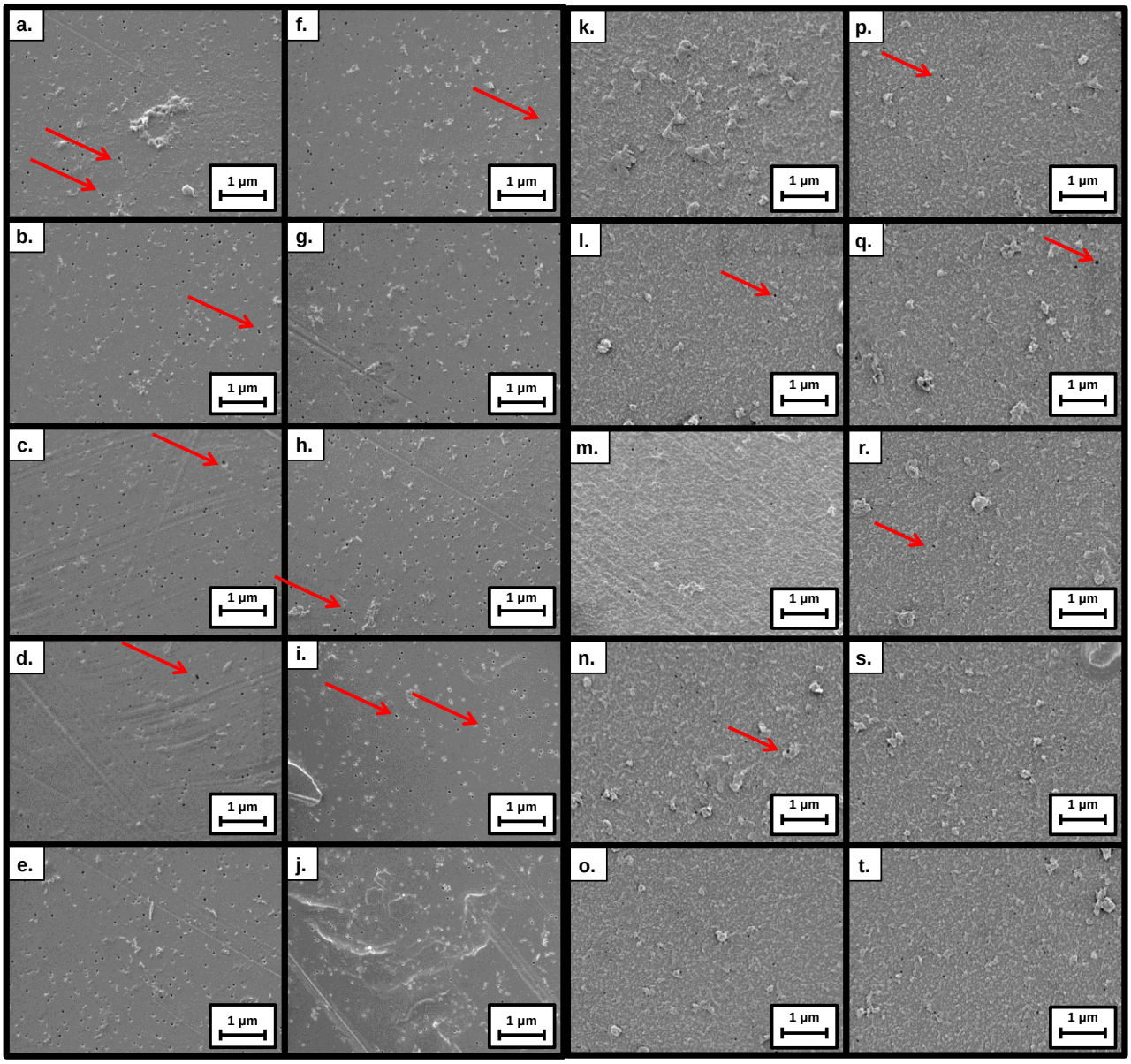

Figure 2.4. SEM images of track-etched membranes (nominal 50 nm pores) before (a-j) and after (k-t) modification with a $(PSS/PAH)_2$ film. Pores are clearly visible in both sets of images, but the number of visible pores decreases after film deposition. This may occur because the increase in roughness and decrease in pore size make the pores more difficult to image. Even if the pores are coated, the coating may be permeable, as during deposition of the second PAH layer, the polymer rejection was 21 ± 6% (PAH was also observed in the effluent rinse solution, following the deposition cycle). Hence nearly all the flow goes through pores that do not block PAH transport. Red arrows indicate the presence of suspected doublets.

2.3.2 Doublet pores in PCTE membranes

Despite the low porosity of track-etched membranes, some pore doublets are visible in SEM images of these membranes (see Figure 2.3 and 2.4). Due to the higher hydraulic permeability of doublet pores compared to single pores, the presence of the former might modify estimates of pore size based on hydraulic permeability (see Figure 2.5).

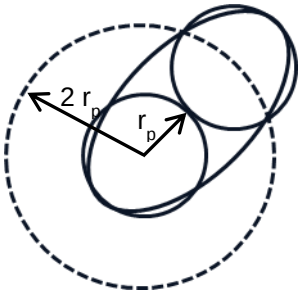

Figure 2.5. Drawing of overlapping pores and the ellipse employed to estimate the permeability of the doublet pore. The dotted circle encloses the area in which a second pore must reside to overlap with the center pore.

For a given pore, the probability of another pore residing close enough to form a doublet is equal to the ratio of the area of a circle with a radius of $2r_p$, where r_p is the radius of a single pore (see Figure 2.5), to the average membrane area per pore. This leads to the total doublet density, n_d, in Equation 2.2:

$$n_d = 2\pi r_p^2 n_p^2 \qquad (2.2)$$

where n_p is the etched track (pore) density, which is the reciprocal of the membrane area per pore. We approximate the doublet hydraulic permeability as that of an elliptical tube whose minor axis is equal to the single pore radius, and whose major axis is two times larger (Figure 2.5). (Note that this is likely an overestimation of hydraulic permeability as most doublets will show significant overlap of the single-pore constituents.) Such an elliptical pore has a hydraulic

permeability that is 16/5 that of a single pore with radius r_p.[19] Thus, considering both single and doublet pores, Equation 2.3. gives the total hydraulic permeability:

$$\chi = \frac{J_v}{\Delta p} = \frac{\pi r_p^4 n_p}{8\eta L}\left(1 + \frac{12}{5}\pi r_p^2 n_p\right) \quad (2.3)$$

The first fraction on the right-hand side of Equation 2.3 originates from the Hagen-Poiseuille equation, and the second term in the parentheses is the correction due to the increased permeability of elliptical doublets compared to two single pores. At pore densities of 7.9 x 10^{12}/m^2 with a pore radius of 40 nm, the relative increase in hydraulic permeability gives rise to only a 2% rise in the estimated pore size, which is well within the experimental error. This correction is even less important for smaller pores. Therefore, we neglect the presence of doublets.

2.4. Depositing and characterizing single bilayer PSS/PAH films in 30-nm PCTE membranes

PCTE membranes with 50-nm pores require adsorption of 3-4 (PSS/PAH) bilayers to decrease the pore radius ~70%. Deposition of such films employs 12-16 individual deposition steps (i.e. 2 polyelectrolyte depositions and their respective rinses for each bilayer deposited), whereas utilizing 30-nm PCTE membranes only requires a single polyelectrolyte bilayer to achieve a similar radius in a modified pore. In addition to minimizing modification time, volume of polyelectrolyte solutions, and waste generated when modifying each membrane, the use of 30-nm pores also decrease the variability in film structures and thicknesses (i.e. fewer adsorption steps and interfaces may lead to more reproducible films).

The average hydraulic permeability of membranes with nominal 30 nm pores was (1.0 ± 0.3) x 10^{-10} m/(s Pa). Using the value of 7.9 x 10^{12} pores/m^2 (obtained from SEM images), this

permeability implies an average pore diameter of 41 nm, although as mentioned above the pores may not have a uniform dimension along their length. Based on flow rates through the membrane the pore diameter decreases from 41 nm to ~37 nm after PSS adsorption.

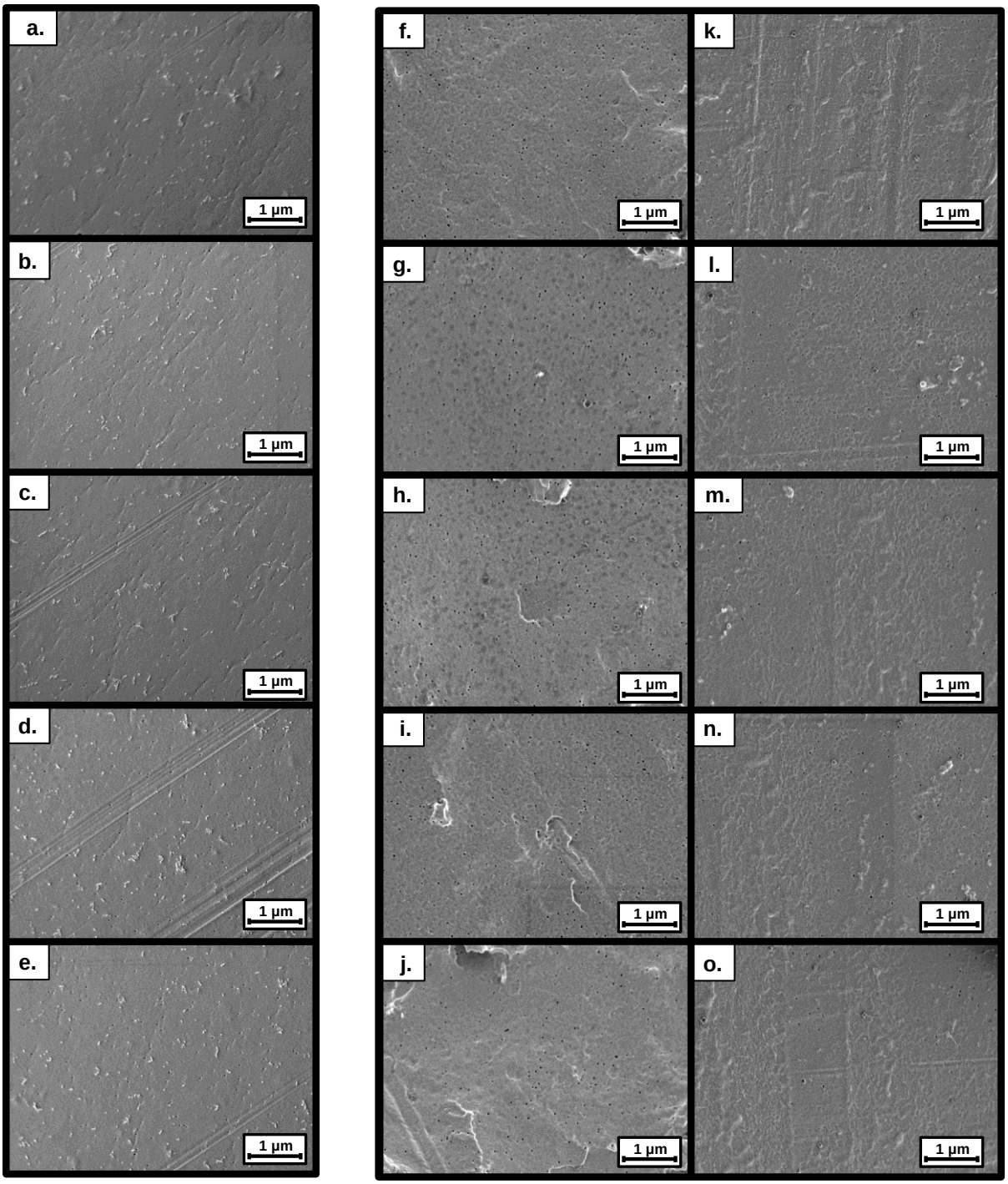

Figure 2.6. SEM images of track-etched membranes (nominal 30 nm pores) before (a-e) and after (f-o) coating with a PSS/PAH film. Pores in the membrane are clearly visible after the coating procedure. Rejection of PAH during deposition of this polymer was 15 ± 9% (Some PAH also appeared in the effluent rinse solution following the PAH deposition cycle).

Subsequent adsorption of a PAH layer decreases the pore diameter from ~37 nm to ~20 nm (calculated from hydraulic permeabilities). Note that if we assume the pore diameter in the bare membrane is the nominal 30 nm, the pore diameter after adsorption of a bilayer would be ~22 nm. This is essentially the same pore diameter that results from adsorption of 3 bilayers in the 50-nm pore. SEM images of these membranes show that pores are open after deposition of one PSS/PAH bilayer (Figure 2.6). Moreover, these membranes do not reject PAH significantly during deposition of the PSS/PAH bilayer.

2.5. Conclusions

Adsorption of polyelectrolytes in PCTE membranes with nominal 50-nm pores, gives film thicknesses of ~7 nm/bilayer for $(PSS\text{-}PAH)_1$ and $(PSS\text{-}PAH)_2$ films, while $(PSS\text{-}PAH)_3$ and $(PSS\text{-}PAH)_4$ films are only ~5.5 nm/bilayer thick. Based on prior work, the decrease in film thickness may stem from a decrease in the surface charge with increasing film thickness.[20] After successful and reproducible PEM adsorption in 50-nm PCTE membranes, we began modifying 30-nm membranes because they require adsorption of fewer polyelectrolyte bilayers to achieve a similar pore diameter. Moreover, adsorption of single layer or single bilayer films may lead to a different surface charge than adsorption of multilayers in constrained environments.

Analyses of SEM images and hydraulic permeability calculations suggest that (nominal) 30-nm PCTE membrane pores are actually ~41-nm in diameter. Based on flow rates through the membrane, the pore diameter decreases from ~41 nm to ~37 nm after PSS adsorption, and to ~20-nm after PAH adsorption. $(PSS\text{-}PAH)_1$ films are much easier to deposit than $(PSS/PAH)_3$ films because of fewer deposition steps. Moving forward, these PEM-modified 50-nm and 30-nm PCTE membranes will provide a framework for examining ion separations in charged nanopores.

REFERENCES

REFERENCES

1. Decher, G. *Science* **1997,** *277*, 1232-1237.

2. Schlenoff, J. B.; Ly, H.; Li, M. *Journal of the American Chemical Society* **1998,** *120*, 7626-7634.

3. Harris, J. J.; Bruening, M. L. *Langmuir* **1999,** *16*, 2006-2013.

4. Ouyang, L.; Malaisamy, R.; Bruening, M. L. *Journal of Membrane Science* **2008,** *310*, 76-84.

5. Krasemann, L.; Tieke, B. *Langmuir* **2000,** *16*, 287-290.

6. DeRocher, J. P.; Mao, P.; Han, J.; Rubner, M. F.; Cohen, R. E. *Macromolecules* **2010,** *43*, 2430-2437.

7. Harris, J. J.; Stair, J. L.; Bruening, M. L. *Chemistry of Materials* **2000,** *12*, 1941-1946.

8. Hollman, A. M.; Bhattacharyya, D. *Langmuir* **2004,** *20*, 5418-5424.

9. Alem, H.; Blondeau, F.; Glinel, K.; Demoustier-Champagne, S.; Jonas, A. M. *Macromolecules* **2007,** *40*, 3366-3372.

10. Schlenoff, J. B.; Dubas, S. T. *Macromolecules* **2001,** *34*, 592-598.

11. Malaisamy, R.; Bruening, M. L. *Langmuir* **2005,** *21*, 10587-10592.

12. Xu, F.; Wang, W. H.; Tan, Y. J.; Bruening, M. L. *Analytical Chemistry* **2010,** *82*, 10045-10051.

13. Dotzauer, D. M.; Dai, J. H.; Sun, L.; Bruening, M. L. *Nano Letters* **2006,** *6*, 2268-2272.

14. Powell, M. R.; Sullivan, M.; Vlassiouk, I.; Constantin, D.; Sudre, O.; Martens, C. C.; Eisenberg, R. S.; Siwy, Z. S. *Nature Nanotechnology* **2008,** *3*, 51-57.

15. Ali, M.; Yameen, B.; Cervera, J.; Ramírez, P.; Neumann, R.; Ensinger, W.; Knoll, W.; Azzaroni, O. *Journal of the American Chemical Society* **2010,** *132*, 8338-8348.

16. Duchet, J.; Legras, R.; Demoustier-Champagne, S. *Synthetic Metals* **1998,** *98*, 113-122.

17. Lee, S. B.; Martin, C. R. *Chemistry of Materials* **2001,** *13*, 3236-3244.

18. Feldoto, Z.; Varga, I.; Blomberg, E. *Langmuir* **2010,** *26*, 17048-17057.

19. Bird, R. B. Notes for the 2nd revised edition of transport phenomena. http://homepages.cae.wisc.edu/~klingen/che320/Notes081010-bookmarked.pdf (15 Dec).

20. Park, S. Y.; Rubner, M. F.; Mayes, A. M. *Langmuir* **2002,** *18,* 9600-9604.

Chapter 3: Monovalent/divalent ion separations with track etched membranes modified with polyelectrolyte multilayer films

Portions of this chapter were published in JA Armstrong, EEL Bernal, AE Yaroshchuk, and ML Bruening. *Langmuir*, 29 (32), 10287-10296 (2013). The Yaroshchuk group performed the theoretical calculations.

3.1. Introduction

Charged nanopores are attractive for separating monovalent and divalent ions via a more extensive electrostatic exclusion of the divalent ion from the pore (Figure 3.1). For example, a positively charged nanopore excludes Mg^{2+} ions more than K^+ ions, so pressure driven flow through the pore will give a permeate solution that is more depleted of Mg^{2+} than K^+. However, to achieve significant selectivity the nanopores must have high enough charge and small enough pore diameters for the electrical double layer to extend throughout the pore. Polyelectrolyte adsorption in nanopores can both enhance charge density and reduce pore size to increase monovalent/divalent ion selectivities in pressure-driven transport.[1]

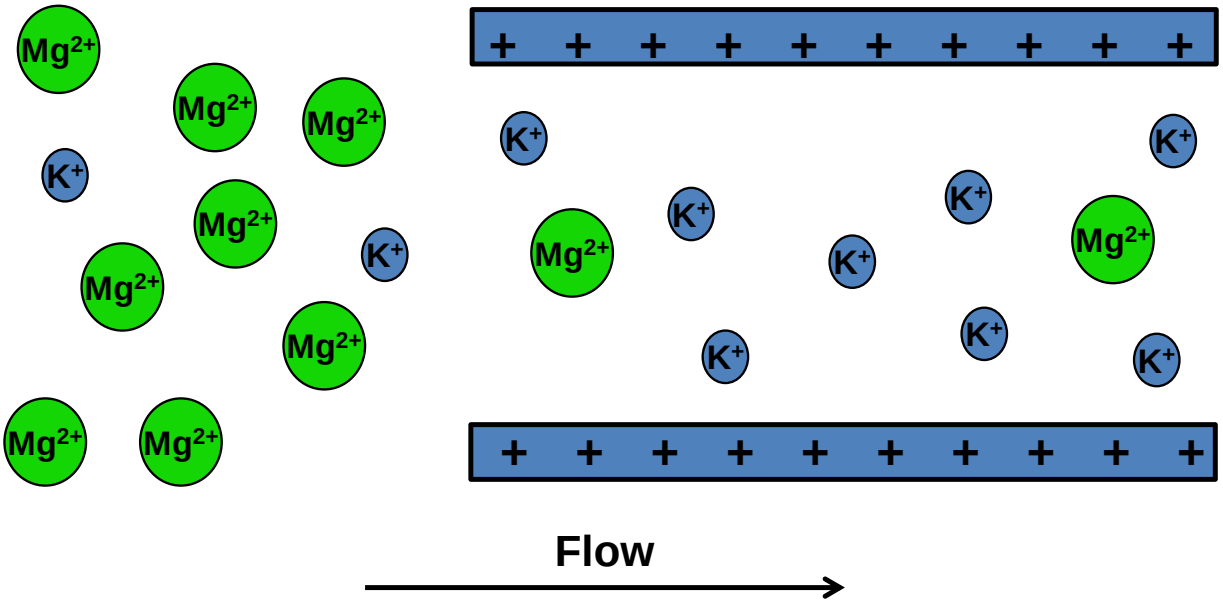

Figure 3.1. Separation of ions possessing different valence (anions are omitted for clarity). The positively charged membrane excludes Mg^{2+} more than K^+, which gives rise to selective permeation of K^+ over Mg^{2+}.

In addition to surface charge and pore diameter, ionic strength also affects ion-exclusion in nanopores because the electrical double layer thickness decreases with increasing ion concentrations.[2-4] Figure 3.2 shows a simulation of the electrostatic potential in charged, cylindrical nanopores for a surface charge of +10 mC/m^2, which is a conservative value for the charge density in pores modified with polyelectrolyte films (see below). Notably, at ionic strengths of around 2 mM, the potential is substantial throughout the pore, which should give rise to separation of monovalent and divalent ions. However, ion passage will vary dramatically with the ionic strength of the solution.[2-4]

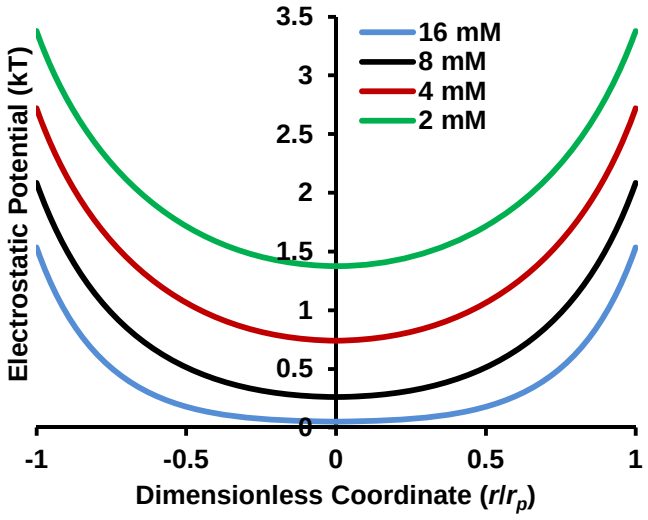

Figure 3.2. Radial distribution of electrostatic potential inside 25-nm diameter nanopores in equilibrium with a solution containing a 1:1 mixture of $MgCl_2$ and KCl. The distribution was obtained via numerical solution of the non-linearized Poisson-Boltzmann equation with the assumption of a surface charge density of +10 mC/m^2. A decrease in the ionic strength (indicated in the graph) gives a progressive disappearance of electrical potential in the central part of the pore, which will lead to less ion-exclusion and lower selectivities for monovalent over divalent ions during pressure-driven transport.[5]

This chapter examines charge-based separations of cations and anions. Initially, we deposited PSS/PAH multilayers in PCTE membranes with 50-nm pores to separate K^+ and Mg^{2+}. However, membranes with a single PSS/PAH bilayer deposited in 30-nm pores show higher selectivity than membranes with 50-nm pores modified with PSS/PAH multilayers. Using the $(PSS/PAH)_1$-modified, 30-nm membranes, we developed a relationship between ionic strength of the feed solution and K^+ and Mg^{2+} rejections (See Figure 3.6). Adsorbing a single layer of PSS in 30-nm pores generates negatively charged membranes that separate Br^- and SO_4^{2-}.

3.2. Ion separation procedure

Membranes were modified with PEMs as described in chapter 2. Filtration experiments were conducted in an Amicon 8010 stirred cell (See Figure 3.3). Pressurized feed solution flows

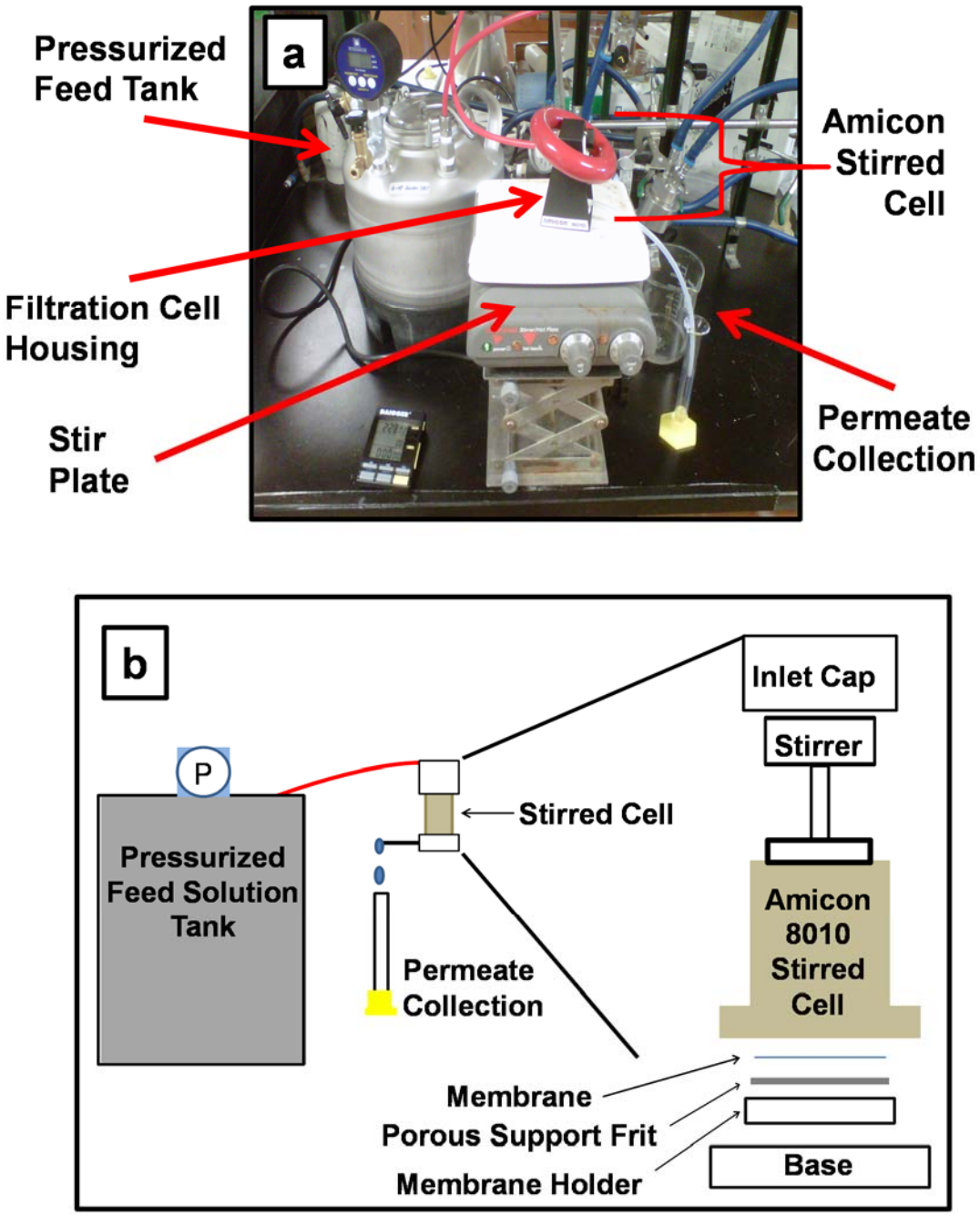

Figure 3.3. Dead-end filtration system. Image (a) is a photograph of the dead-end filtration system. Figure (b) shows the system components schematically, including an expanded view of the parts of the Amicon filtration cell. Note the diagram does not show the Amicon cell housing (the black frame in the photograph), which prevents the inlet cap from ejecting off of the cell under pressure. The picture also shows a red donut-

shaped ring around the cell housing; this lead ring holds the cell on the stir plate, to ensure continuous stirring.

from the feed tank, into the filtration cell, which contains a magnetic stir bar that spins continuously during separation experiments. The PCTE membranes rest on a porous steel frit that provides support but minimal resistance to flow. Filtration was conducted at 10-300 kPa for the 50-nm membranes, and 210-420 kPa for the 30-nm membranes, to provide flow rates of 0.1-1.0 mL/min.

For each dead-end filtration, 4 to 7 permeate aliquots with volumes of 2-3 mL were weighed to determine flux and subsequently analyzed using either flame atomic absorption/emission spectroscopy (Varian AA240, K^+, Mg^{2+}, Li^+, and Cs^+ analyses) or ion chromatography (Dionex ion chromatograph 2000i/SP with an Alcott 728 auto-sampler, acetate, Br^-, and SO_4^{2-} analyses). Data for the first permeate aliquot were discarded to allow for membrane rinsing and equilibration with the feed solution. For a given solute, rejection, *R*, was calculated using equation 3.1, where C_p and C_f are the solute concentrations in the permeate and feed, respectively.

$$R = 1 - \frac{C_p}{C_f} \tag{3.1}$$

Equation 3.2 defines the selectivity, α_B^A, for A over B. This equation can be simply expressed in terms of rejections as shown.

$$\alpha_B^A = \frac{C_{A,p}/C_{A,f}}{C_{B,p}/C_{B,f}} = \frac{1-R_A}{1-R_B} \tag{3.2}$$

During the separations, solution from the feed tank continuously replenished the Amicon cell to maintain a constant volume, but ion rejection by the membrane gradually increased the

feed concentration in the stirred, dead-end cell. To account for this increase, we determined the feed ion concentrations using equation 3.3 where $C_{f,N+1}$ is the concentration of a specific ion in

$$C_{f,N+1} = C_{f,N} + \frac{V_{p,N}}{17.5} * (C_{f,0} - C_{p,N}) \quad (3.3)$$

the Amicon cell at the start of permeate aliquot $N+1$, $C_{f,N}$ is the concentration in the Amicon cell at the start of the previous permeate aliquot, $V_{p,N}$ is the volume of permeate aliquot N (mL), $C_{f,0}$ is the initial feed concentration or concentration in the feed tank, $C_{p,N}$ is the concentration in permeate N, and 17.5 mL is the volume of the Amicon stirred cell. After calculating the feed concentrations at the start and end of each permeate aliquot, the average of these two values served as the feed concentration for calculating rejections and selectivities. In an experiment with around 90% rejection, the feed concentration approximately doubled during passage of 20 mL of solution through the membrane. In most cases, experiments involved passage of 10-20 mL of solution through the membrane. Analysis of the final feed solution in the stirred cell gave a concentration within 10% of the calculated final feed concentration.

3.3. K^+/Mg^{2+} separations in modified 50-nm membranes

Figure 3.4 illustrates a simulation of ion exclusion and shows the K^+/Mg^{2+} transport selectivity calculated by means of a standard space-charge model in the limiting case of negligible transmembrane diffusion.[6] Notably, selectivity increases with both decreasing pore size and decreasing ionic strength. Increasing selectivity corresponds to conditions that give rise to greater double layer thicknesses.

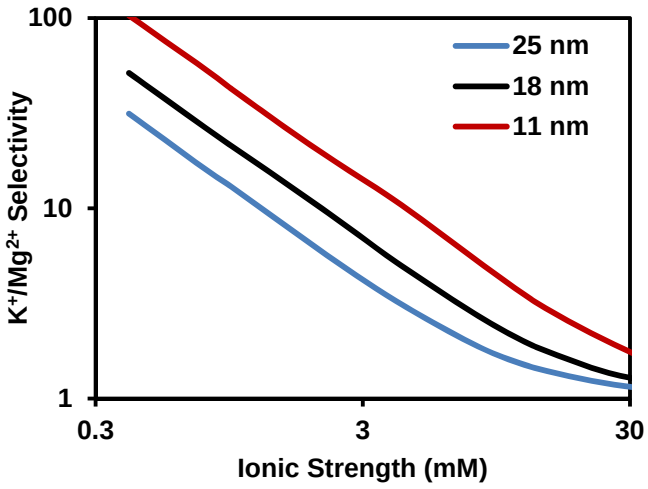

Figure 3.4. Simulated K^+/Mg^{2+} transport selectivity (1:1 feed composition) during pressure-driven flow in a charged nanopore as a function of feed ionic strength. The simulation assumes positively charged, cylindrical nanopores (surface-charge density of +10 mC/m^2), and different pore diameters are indicated in the figure. Similar behavior would occur with negatively charged nanopores and separation of divalent and monovalent anions.[5]

Figure 3.5 shows experimental K^+/Mg^{2+} selectivities in pressure-driven transport through PCTE membranes before and after modification of nominal 50-nm pores with $(PSS/PAH)_n$ films. For unmodified membranes, the K^+/Mg^{2+} selectivity is approximately 1. The native membrane should have a negative charge because the polycarbonate surface contains a low density of carboxylate groups. This negative charge might selectively attract Mg^{2+} into the pore, but the double layer should occupy a minimal fraction of the pore volume so selectivity is absent. K^+/Mg^{2+} selectivity increases to values as high as ~8 after deposition of $(PSS/PAH)_2$ and $(PSS/PAH)_3$ films, which terminate in positive charge, but then decreases for membranes containing $(PSS/PAH)_4$ coatings. Although the pore diameters decrease on going from a $(PSS/PAH)_3$-coated to a $(PSS/PAH)_4$-coated membrane (Figure 2.3), the K^+/Mg^{2+} selectivity decreases, suggesting that the positive surface charge decreases after adsorption of the fourth bilayer. Additionally, as the pore size becomes smaller, diffusion will become more significant compared to convection and decrease selectivity. Other studies also suggest that surface charge

may decrease after deposition of several PEMs in nanochannels.[7] Changing the rinsing solution during polyelectrolyte deposition from water to 0.5 M NaCl leads to a small increase in selectivity (Figure 3.5), perhaps because rinsing with the salt solution decreases the swelling of the outer PAH layer to give a higher charge density.[8]

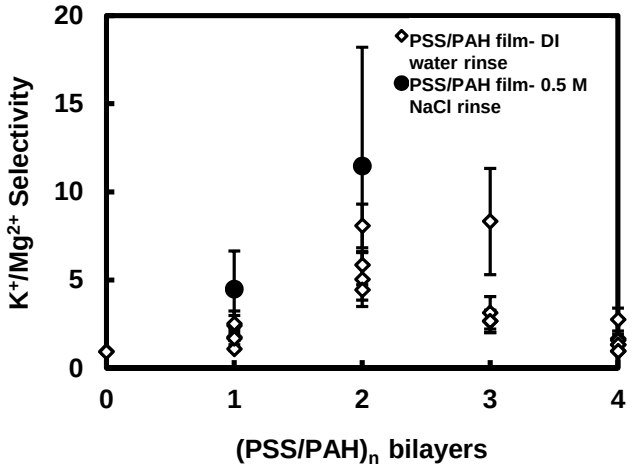

Figure 3.5. K^+/Mg^{2+} selectivities in track-etched membranes (nominal 50 nm pores) before and after modification with $(PSS/PAH)_n$ bilayers, n=1-4. In membrane modification, rinsing occurred with either deionized (DI) water (open diamonds) or 0.5 M NaCl (filled circles). In both figures, each symbol represents a different replicate membrane, and the error bars show the standard deviations of ~7 determinations of selectivity during passage of 0.5 mM $MgCl_2$, 0.5 mM KCl solutions through each membrane.[5] $(PSS/PAH)_n$ films were deposited from solutions containing 0.5 M NaCl (supporting electrolyte).

3.4. K^+/Mg^{2+} separations in modified 30-nm membranes

In an effort to decrease pore size without decreasing surface charge, we modified membranes containing nominal 30 nm-diameter pores with $(PSS/PAH)_1$ and $(PSS/PAH)_2$ films. Deposition of $(PSS/PAH)_2$ from 1.0 M NaCl (with 1.0 M NaCl rinses) decreases the flow rate >95%, showing that pores are essentially plugged after adsorption of 2 bilayers. Thus, we focused on depositing films with only one bilayer. During filtration of a 0.5 mM KCl, 0.5 mM

$MgCl_2$ feed solution through 30-nm PCTE membranes modified with $(PSS/PAH)_1$ films, the K^+/Mg^{2+} selectivity was typically >5. (The Mg^{2+} concentration in the permeate was less than 10 μM, the detection limit of the analysis, so the selectivity is likely much greater than 5.) Thus, the 30 nm pores with a single PSS/PAH bilayer give rise to selectivities comparable to those in 50 nm pores with multilayer films.

Because cation rejections stem from electrostatic exclusion, they should rapidly decrease with increasing solution ionic strength. Figure 3.6 shows K^+ and Mg^{2+} rejections as a function of ionic strength during filtration through nominal 30 nm pores modified with a single PSS/PAH bilayer. The K^+ rejection decreases more rapidly than the Mg^{2+} rejection with increasing ionic strength for both single salt and mixed salt experiments, but the K^+/Mg^{2+} selectivity also decreases, consistent with Figure 3.4. For example, K^+/Mg^{2+} selectivities based on single-salt measurements range from ~5 at ~20 mM ionic strength to ~12 with ~2 mM ionic strength. In mixed salt solutions, the selectivities range from ~2.5 at 50 mM total ionic strength to >10 at 8 mM ionic strength. More importantly, Mg^{2+} passage in mixed salt solutions is undetectable (permeate concentration <10 μM) at total ionic strengths <5 mM.

Notably, at low ionic strength the K^+ rejection is higher in the mixed salt solutions than in the single salt experiments with only KCl. At 2-3 mM ionic strength, K^+ rejection is only ~65% in the single-salt filtration, but ~85% in a mixed salt solution. This may imply that Mg^{2+} adsorption increases the surface charge in the membrane pore. Our previous measurements of streaming potential during flow of solutions over $(PSS/PAH)_n$ films also provide evidence for Mg^{2+} adsorption.[9]

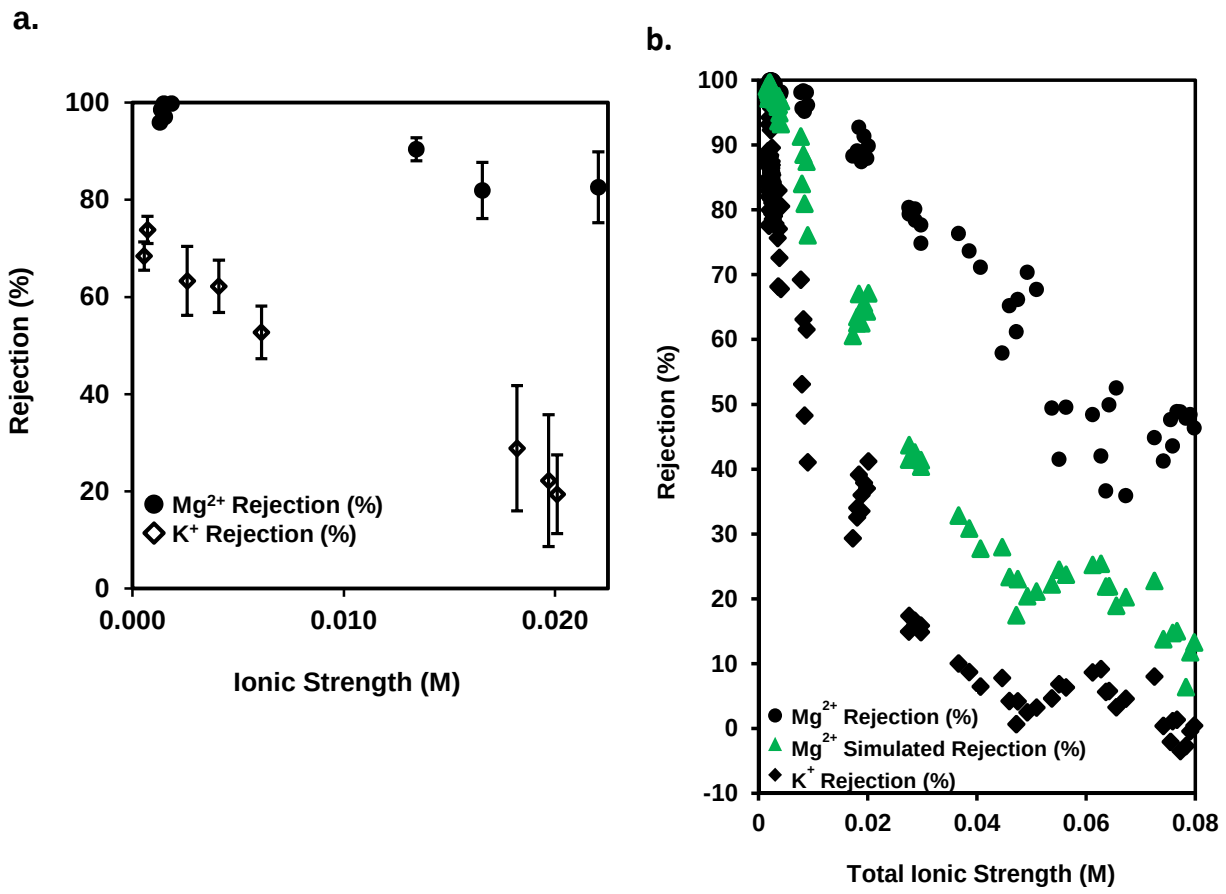

Figure 3.6. Rejections of K^+ (diamonds) and Mg^{2+} (circles) as a function of feed ionic strength during dead-end filtration through PCTE membranes that were modified with a $(PSS/PAH)_1$ film. Films were deposited from solutions containing 1.0 M NaCl, and rinsed with 1.0 M NaCl. Prior to each experiment, ~20 mL of DI H_2O was passed through the membrane. The aqueous feed solutions contained (a) single salts or (b) a mixture of KCl and $MgCl_2$. In (b) the green triangles show Mg^{2+} rejections predicted with the Poisson-Boltzmann equation and equation 3.10, assuming a pore diameter of 20 nm and the surface charge needed to give the K^+ rejection. (The discrepancy between simulated and experimental Mg^{2+} rejections likely results from constricted pores near the top of the membrane. See below for modeling with smaller pore diameters.) Prior to modification, the membranes had nominal 30 nm diameter pores. The mixed solutions initially contained equal concentrations of the two salts, and the average hydraulic permeability was 6.3×10^{-12} m/(s Pa).[5]

3.5. Modeling K^+/Mg^{2+} selectivities in membranes modified with $(PSS/PAH)_1$ films

To model ion fluxes in these films, we employed equation 3.4 where j_V is the

$$j_V \cdot c_{ip} = -P_i \cdot \left(\frac{dc_i}{dx} + Z_i c_i \frac{d\varphi}{dx}\right) + j_V \cdot \tau_i \cdot c_i \qquad (3.4)$$

transmembrane volume flux, c_{ip} is the ion concentration in the permeate, P_i is the ionic permeability (including the partitioning coefficients), c_i is the ion concentration in the so-called virtual (or reference) solution, Z_i is the ion charge, φ is the electrostatic potential in this solution, and τ_i is the ion transmission coefficient. The virtual solution is defined as a solution that could be in thermodynamic equilibrium with a given point inside the nanopore.[10] The first term on the right side of equation 3.4 gives ion flux due to diffusion and electromigration, whereas the second term describes convective ion flux. As demonstrated previously, for long straight nanopores,[11] equations 3.5 and 3.6 describe the coefficients P_i and τ_i, where Γ_i represents the local ion partition coefficient inside the nanopores and the brackets $\langle \quad \rangle$ and $\langle \quad \rangle_c$ denote simple

$$P_i \equiv D_i \langle \Gamma_i \rangle \tag{3.5}$$

$$\tau_i \equiv \langle \Gamma_i \rangle_c \tag{3.6}$$

cross-sectional averaging and liquid-velocity-profile-weighted cross-sectional averaging, respectively. For the assumed cylindrical pore geometry:

$$\langle \Gamma_i \rangle \equiv 2 \int_0^1 dr \cdot r \cdot exp\big(-Z_i \varphi(r)\big) \tag{3.7}$$

$$\langle \Gamma_i \rangle_c \equiv 4 \int_0^1 dr \cdot r \cdot (1 - r^2) \cdot exp\big(-Z_i \varphi(r)\big) \tag{3.8}$$

where $\varphi(r)$ is the dimensionless electrostatic potential, which we find from the solution of the Poisson-Boltzmann equation. The approach of equations 3.4-3.8 is a thermodynamically consistent implementation of a classical space-charge model, which originates from the seminal studies by Dresner and Osterle et al.[12-15] The appendix describes how our collaborators numerically solved the Poisson-Boltzmann equation and equation 3.4 for a system with 3 ions using a specified pore diameter and surface charge.

Initially, we examined whether diffusion makes a significant contribution to transport. Using the approximate expression in equation 3.9,[16]

$$Pe \approx 0.58 \cdot r_p^2(nm) \cdot a_s(nm) \cdot \Delta P(MPa) \quad (3.9)$$

the Péclet number, *Pe*, for the K^+/Mg^{2+} separations with $(PSS/PAH)_1$-modified nominal 30 nm membranes (r_p=10 nm, a_s is the hydrodynamic diameter of the ion, and ΔP =0.4 MPa) is around 3. This value is large enough for the ion rejections to reach their reflection coefficients, *i.e.*, ion transport by diffusion is small compared to that by convection and electromigration, so virtual ion concentrations are essentially the feed concentrations and practically the same throughout the pore. In mixtures with a common counter-ion (*e.g.*, $KCl/MgCl_2$ with a positively charged membrane) with increasing Péclet number the ion rejections tend to their zero-current reflection coefficients, σ_i.[11] For a given ion:

$$\sigma_i \equiv 1 - \tau_i + \frac{\rho t_i}{F Z_i c_i} \quad (3.10)$$

where ρ is the so-called electrokinetic charge density defined as

$$\rho \equiv F \sum_j^n Z_j c_j \tau_j \quad (3.11)$$

and t_i is the ion transport number defined as

$$t_i \equiv \frac{Z_i^2 c_i P_i}{\sum_j^n Z_j^2 c_j P_j} \quad (3.12)$$

As rejection is essentially the reflection coefficient, equation 3.10 shows that ion rejections occur because the electrostatic potential within the charged pore gives rise to low partition coefficients and small transmission coefficients, τ_i. The third term on the right hand side of equation 3.10 corresponds to electromigration and shows that streaming potentials tend to decrease rejections for K^+ and Mg^{2+} in positively charged pores. However, the contribution of this term is roughly as small as the ion transmission coefficient, τ_i, if the exclusion is high so that the transport number for the rejected ion is low.

Assuming that adsorption of a film reduces the pore diameter uniformly throughout the membrane thickness (pore length), the average hydraulic permeability of $(PSS/PAH)_1$-modified membranes (6.3×10^{-12} m/(s Pa) implies a modified-pore diameter of ~20 nm. Using this pore size, the only parameter needed to fit the reflection coefficient using equation 3.10 (for all three ions) and the Poisson-Boltzmann distribution is the surface-charge density. We estimated the surface charge from the experimental K^+ rejections and subsequently calculated the corresponding Mg^{2+} rejections. Thus, in Figure 3.6b the relative trends in calculated Mg^{2+} rejection (triangles) follow trends in the experimental K^+ rejection (diamonds). However, Figure 3.6b shows that the experimental Mg^{2+} rejections (circles) are systematically higher than the calculated Mg^{2+} rejections. Alternatively, one could fit the surface charge using the Mg^{2+} rejections and show that the experimental K^+ rejections are lower than calculated values.

One possible reason why a single surface charge density cannot account for both Mg^{2+} and K^+ rejections is that polyelectrolyte adsorption significantly modifies only a zone near the pore entrance.[17] Thus, the pore diameter in these entrance zones would be considerably smaller than the value estimated from the hydraulic permeability by assuming a homogeneous modification. If this is the case, one cannot determine the entrance zone pore size from hydraulic permeabilities because the effective length of the modified zone is unknown. However, since simultaneous experimental rejections of both K^+ and Mg^{2+} are available for each filtration condition with mixed salt solutions, one can simultaneously fit both pore size and the surface-charge density to the experimental data. The fitted pore diameter should represent the entrance zone, which controls partitioning.

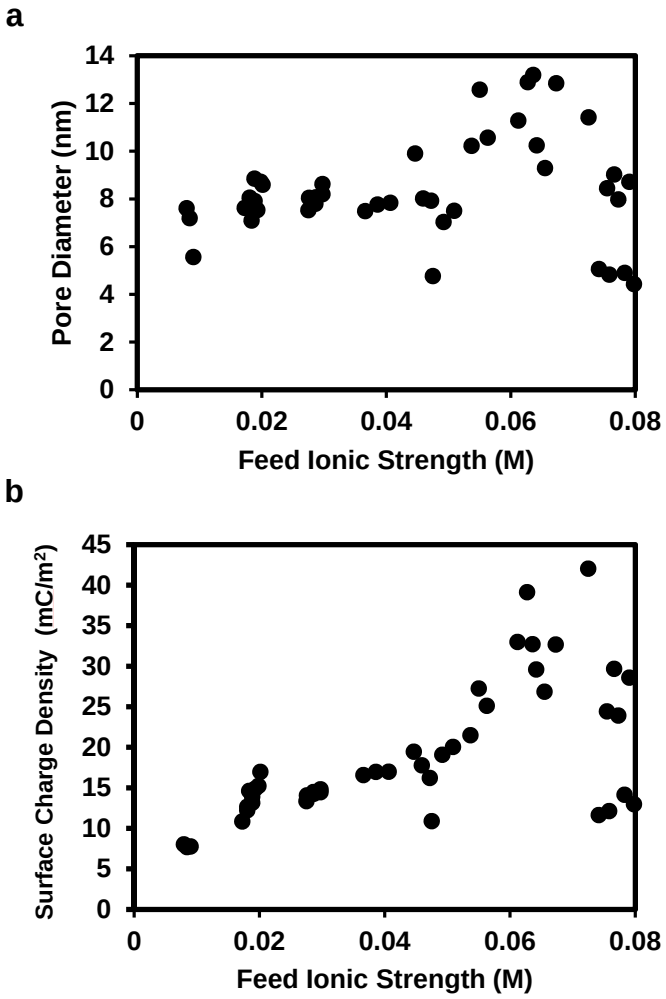

Figure 3.7. Pore diameters (a) and surface charge densities (b) calculated from measured K^+ and Mg^{2+} rejections in Figure 3.6b. The values were calculated by simultaneously fitting rejections of both ions through numerical solution of transport equations with a subroutine for calculating ion permeabilities and ion transmission coefficients via numerical solution of the non-linearized Poisson-Boltzmann equation (see the appendix at the end of the this chapter for details).[5]

Figure 3.7a shows the results of such fitting. In this case *Pe* is not large enough for the zero-current reflection coefficient to approximate rejection, so we numerically solved both the Poisson-Boltzmann equation and equation 3.4. The average pore diameter is 8.4 nm (standard deviation of 2.1 nm for n=45), which is much smaller than the ~20 nm value estimated from the hydraulic permeability. Moreover, as we would expect the estimated pore diameter does not vary

significantly with the ionic strength of the feed solution. With this low diameter, the value of *Pe* could be small enough that diffusion is significant. At low trans-membrane volume flows in the presence of doubly charged ions, trans-membrane electric fields of diffusion origin may accelerate the flux of singly charged ions to give low or even negative rejections of the singly charged coions (e.g. K^+). Notably, sometimes the measured K^+ rejections were slightly negative (see the highest ionic strengths in Figure 3.6b).

Figure 3.7b shows the fitted surface charge densities. They have reasonable magnitudes of several tens of mC/m^2, and surface charge appears to increase with increasing feed ionic strength, which would be consistent with Mg^{2+} adsorption as discussed above. However, the scatter in the data prevent a firm conclusion in this regard. The corresponding values of zeta-potentials (or pore-surface electrostatic potentials) are in the range of 45-50 mV, which is consistent with previous measurements of PSS/PAH zeta potentials.[1, 9, 18-21]

Using the average pore diameter of 8.4 ± 2.1 nm and the hydraulic permeability, we estimated the effective thickness of the modified entrance zone as 180 nm. (We assumed the rest of the membrane was not modified and calculated the entrance zone length using a series resistance model.) However, given the uncertainty in the pore diameter, the entrance zone thickness could range from 40 nm to 255 nm. These thicknesses seem reasonable if after initial adsorption of polymer chains near the entrance, electrostatic or size based exclusion prevents further modification.[17] Fully extended PAH chains (M_w=70,000) have lengths around 20-30 nm. A narrow, short entrance region is attractive for obtaining the high ion selectivities associated with low pore diameters while still maintaining a reasonable flux.

3.6. Br^-/SO_4^{2-} separations in modified 30-nm membranes

Similar to the K^+/Mg^{2+} separations achieved in Figure 3.6b, membranes modified with a single PSS layer show moderate Br^-/SO_4^{2-} selectivities (Table 3.1). Pores in the bare track-etched membrane have a negative surface charge that results in a Br^-/SO_4^{2-} selectivity of 1.9 ± 0.3, but adsorption of PSS leads to increases in rejection, presumably because of both a decrease in pore diameter and a small increase in surface charge.

Membrane	Br^- %Rejection	SO_4^{2-} %Rejection	Br^-/SO_4^{2-} Selectivity
Bare	**16 ± 3**	**54 ± 8**	**1.9 ± 0.3**
$(PSS)_1$-modified	**48 ± 8**	**83 ± 6**	**3.4 ± 0.8**

Table 3.1. Br^- and SO_4^{2-} rejections and Br^-/SO_4^{2-} selectivities during dead-end filtration through bare and PSS-modified track-etched membranes (30 nm pores prior to modification). The feed solutions initially contained 0.5 mM NaBr and 0.5 mM Na_2SO_4, and the transmembrane pressure was 414 kPa. The uncertainty values are the standard deviations of a total of 6 permeate measurements on two different membranes, for both the bare and modified membrane experiments.[5]

The average hydraulic permeability of membranes with nominal 30 nm pores was (1.0 ± 0.3)x10^{-10} m/(s Pa). Using the value of 7.9 x 10^{12} pores/m^2 (obtained from SEM images), this permeability implies an average pore diameter of 41 nm, although as mentioned above the pores may not have a uniform dimension along their length. Based on flow rates through the membrane, the pore diameter decreases from 41 nm to ~37 nm after PSS adsorption. Sulfate rejections in PSS_1-modified membranes are lower than Mg^{2+} rejections in $(PSS/PAH)_1$-modified membranes, which may reflect either Mg^{2+} adsorption that increases the positive charge in $(PSS/PAH)_1$-modified membranes, or a smaller pore size after adsorption of PAH.

3.7. Summary

PEM-modified, PCTE membranes separate monovalent and divalent ions, and transport selectivities depend on ionic strength, consistent with a selectivity mechanism based on exclusion of divalent ions from the electrical double layer. Notably, we achieved a permeate solution with no detectable Mg^{2+} at ionic strengths <5 mM. Compared to single-salt experiments, the higher K^+ rejection in mixed-salt solutions suggests Mg^{2+} incorporation within the PEM film to increase surface charge and K^+ rejection. In addition to the monovalent/divalent cation separations, $(PSS)_1$-modified membranes achieved monovalent/divalent anion selectivities of 3.4 ± 0.8. Simulations suggest that the K^+ and Mg^{2+} rejections in mixed salt solutions imply a narrow region near the pore entrance that enhances selectivity.

APPENDIX

APPENDIX

The basics of the space-charge model used in this section date back to the 1960s.[14, 15] However, the original version of the model was developed only for the particular case of straight capillaries/pores because a specific procedure was used for the separation of electrostatic potential into components dependent solely on the axial and transversal coordinates. Later on, it became clear that the possibility of such separation was due to the existence of local thermodynamic equilibrium at the length scale of the capillary/pore diameter,[11, 22, 23] which made possible the analysis of more complex geometries.[24] Owing to the local equilibrium, the ion-transport problem below can be conveniently formulated in terms of a virtual (or reference) solution that could be in thermodynamic equilibrium with a given cross-section inside the capillary/pore. Contrary to the previous studies, we use the model for the description of ion transfer in a mixture with three ions of different charges. For the range of pore sizes/electrolyte concentrations encountered in this study, none of the known approximations (small potentials, large potentials, non-overlapped diffuse parts of electric double layers) is applicable for the description of the ion distribution inside pores. Therefore, we solve numerically both the non-linearized Poisson-Boltzmann equation and the ion-transport problem.

Equation A3.1 describes transport of a given ion inside the charged nano-pores,

$$j_V \cdot c_{ip} = -P_i \cdot \left(\frac{dc_i}{dx} + Z_i c_i \frac{d\varphi}{dx}\right) + j_V \cdot \tau_i \cdot c_i \qquad \text{(A3.1)}$$

where j_V is the trans-membrane volume flux, τ_i is the ion transmission coefficient, c_{ip} is the ion concentration in the permeate, c_i is the ion concentration in the virtual (or reference) solution, φ is the electrostatic potential in this solution, and P_i is the ionic permeability (including the partitioning coefficients).

As demonstrated previously,[11] for long straight nano-pores, equations A3.2 and A3.3 describe the coefficients P_i and τ_i

$$P_i \equiv D_i\langle\Gamma_i\rangle \tag{A3.2}$$

$$\tau_i \equiv \langle\Gamma_i\rangle_c \tag{A3.3}$$

where Γ_i represents the local ion partition coefficient (along the radial coordinate) inside the nano-pores and the brackets $\langle\ \ \rangle$ and $\langle\ \ \rangle_c$ mean simple cross-section averaging and liquid-velocity-profile-weighted cross-sectional averaging, respectively. For the assumed cylindrical pore geometry,

$$\langle\Gamma_i\rangle \equiv 2\int_0^1 dr\cdot r\cdot exp\big(-Z_i\varphi(r)\big) \tag{A3.4}$$

$$\langle\Gamma_i\rangle_c \equiv 4\int_0^1 dr\cdot r\cdot(1-r^2)\cdot exp\big(-Z_i\varphi(r)\big) \tag{A3.5}$$

where $\varphi(r)$ is the dimensionless electrostatic potential, which we find from the solution of the Poisson-Boltzmann equation (equation A3.6)

$$\Delta\varphi = -\lambda^2\sum_i^n \frac{Z_i+\prod_j^n Z_j\cdot\left(\frac{C}{I}\right)}{\prod_{j\neq i}^n(Z_i-Z_j)}\cdot exp(-Z_i\varphi) \tag{A3.6}$$

formulated here for an arbitrary electrolyte mixture and in terms of total virtual ion concentration, *C*, and double virtual ionic strength, *I*, introduced below; the coordinate is scaled on the pore radius, r_p. Equation A3.7 defines λ^2, which

$$\lambda^2 \equiv \frac{F^2 I\cdot r_p^2}{\varepsilon\varepsilon_0 RT} \tag{A3.7}$$

is the squared ratio of pore radius to the Debye screening length. The boundary conditions to the Poisson-Boltzmann equation are

$$\left.\frac{\partial\varphi}{\partial r}\right|_{r=0} = 0 \tag{A3.8}$$

$$\left.\frac{\partial\varphi}{\partial r}\right|_{r=1} = \frac{\sigma F r_p}{\varepsilon\varepsilon_0 RT} \tag{A3.9}$$

where σ is the surface-charge density.

Now, let us consider a three-ion system. Transformation of equation (A3.1) leads to

$$-Pe \cdot c_{ip} \cdot \rho_i = \frac{dc_i}{dx} + Z_i c_i \frac{d\varphi}{dx} - Pe \cdot \rho_i \cdot \tau_i \cdot c_i \quad \text{(A3.10)}$$

$$Pe \equiv \frac{j_V}{P_3} \quad \text{(A3.11)}$$

$$\rho_i \equiv \frac{P_3}{P_i} \quad \text{(A3.12)}$$

where P_3 is the membrane permeability to the common ion.

Multiplying equation A3.10 by Z_i^k and summing over all the ions gives

$$-Pe \cdot k_k = \frac{dA_k(x)}{dx} + A_{k+1}(x) \cdot \frac{d\varphi}{dx} - Pe \cdot \mathrm{T}_k(x) \quad \text{(A3.13)}$$

where

$$k_k \equiv \sum_i^3 Z_i^k \rho_i \, c_{ip} \quad \text{(A3.14)}$$

$$A_k(x) \equiv \sum_i^3 Z_i^k c_i \, (x) \quad \text{(A3.15)}$$

$$\mathrm{T}_k(x) \equiv \sum_i^n Z_i^k \rho_i \tau_i c_i \, (x) \quad \text{(A3.16)}$$

$\mathrm{T}_k(x)$ are linear combinations of sought-for virtual ion concentrations. Due to the electric neutrality of the virtual solution

$$A_1(x) \equiv 0 \quad \text{(A3.17)}$$

Therefore,

$$\frac{dA_0(x)}{dx} = Pe \cdot (\mathrm{T}_0(x) - k_0) \quad \text{(A3.18)}$$

$$\frac{d\varphi}{dx} = Pe \cdot \frac{\mathrm{T}_1(x) - k_1}{A_2(x)} \quad \text{(A3.19)}$$

$$\frac{dA_2(x)}{dx} = Pe \cdot \left(-k_2 + A_3(x) \cdot \frac{k_1 - \mathrm{T}_1(x)}{A_2(x)} + \mathrm{T}_2(x) \right) \quad \text{(A3.20)}$$

For 3-ion systems, $A_3(x)$ is not linearly independent and can be expressed as

$$A_3(x) \equiv \prod_i^3 Z_i \cdot A_0(x) + \sum_i^3 Z_i \cdot A_2(x) \quad \text{(A3.21)}$$

By substituting equation A3.21 into equations A3.18 and A3.20, we obtain

$$-\frac{dI}{dx} = Pe \cdot \left\{k_2 - k_1 \cdot \left(\sum_i^3 Z_i + \prod_i^3 Z_i \cdot \frac{C(x)}{I(x)}\right) - \left[\mathrm{T}_2(x) - \mathrm{T}_1(x) \cdot \left(\sum_i^3 Z_i + \prod_i^3 Z_i \cdot \frac{C(x)}{I(x)}\right)\right]\right\} \tag{A3.22}$$

$$-\frac{dC}{dx} = Pe \cdot \left(k_0 - \mathrm{T}_0(x)\right) \tag{A3.23}$$

where we have denoted

$$I(x) \equiv A_2(x) \tag{A3.24}$$

$$C(x) \equiv A_0(x) \tag{A3.25}$$

Evidently, C is the total virtual ion concentration and I is two times the virtual ionic strength.

The functions $\mathrm{T}_k(x)$ can be presented as linear combinations of $I(x)$ and $C(x)$.

$$\mathrm{T}_k(x) \equiv \mathrm{T}_{kC} \cdot C(x) + \mathrm{T}_{kI} \cdot I(x) \tag{A3.26}$$

$$-\frac{dI}{dx} = Pe \cdot \left\{k_2 - k_1 \cdot \left(\sum_i^3 Z_i + \prod_i^3 Z_i \cdot \frac{C(x)}{I(x)}\right) - \left[(\mathrm{T}_{2C} - \sum_i^3 Z_i \cdot \mathrm{T}_{1C} - \mathrm{T}_{1I} \cdot \prod_i^3 Z_i) \cdot C(x) + (\mathrm{T}_{2I} - \sum_i^3 Z_i \cdot \mathrm{T}_{1I}) \cdot I(x) - \mathrm{T}_{1C} \cdot \prod_i^3 Z_i \cdot \frac{C(x)^2}{I(x)}\right]\right\} \tag{A3.27}$$

Furthermore, we can show that

$$\mathrm{T}_{2C} \equiv \mathrm{T}_{1I} \cdot \prod_i^3 Z_i \tag{A3.28}$$

$$\mathrm{T}_{1C} \equiv \prod_i^3 Z_i \cdot \mathrm{T}_{0I} \tag{A3.29}$$

Therefore,

$$-\frac{dI}{dx} = Pe \cdot \left\{k_2 - [k_1 - \mathrm{T}_{0I} \cdot \prod_i^3 Z_i \cdot C(x)] \cdot \left(\sum_i^3 Z_i + \prod_i^3 Z_i \cdot \frac{C(x)}{I(x)}\right) + T_{DI} \cdot I(x)\right\} \tag{A3.30}$$

$$-\frac{dC}{dx} = Pe \cdot \{k_0 - [\mathrm{T}_{0C} \cdot C(x) + \mathrm{T}_{0I} \cdot I(x)]\} \tag{A3.31}$$

where we have denoted

$$\mathrm{T}_{0I} \equiv \sum_i^3 \frac{\rho_i \tau_i}{\prod_{j \neq i}^3 (Z_i - Z_j)} \equiv \frac{\rho_1 \tau_1}{(Z_1 - Z_2)(Z_1 - Z_3)} + \frac{\rho_2 \tau_2}{(Z_2 - Z_1)(Z_2 - Z_3)} + \frac{\rho_3 \tau_3}{(Z_3 - Z_1)(Z_3 - Z_2)} \tag{A3.32}$$

$$T_{DI} \equiv \sum_i^3 \frac{\rho_i \tau_i Z_i \sum_{j \neq i}^3 Z_j}{\prod_{j \neq i}^3 (Z_i - Z_j)} \equiv \frac{\rho_1 \tau_1 Z_1 (Z_2 + Z_3)}{(Z_1 - Z_2)(Z_1 - Z_3)} + \frac{\rho_2 \tau_2 Z_2 (Z_1 + Z_3)}{(Z_2 - Z_1)(Z_2 - Z_3)} + \frac{\rho_3 \tau_3 Z_3 (Z_1 + Z_2)}{(Z_3 - Z_1)(Z_3 - Z_2)} \tag{A3.33}$$

$$\mathrm{T}_{0C} \equiv \sum_i^3 \frac{\rho_i \tau_i \prod_{j\neq i}^3 Z_j}{\prod_{j\neq i}^3 (Z_i - Z_j)} \equiv \frac{\rho_1 \tau_1 Z_2 Z_3}{(Z_1 - Z_2)(Z_1 - Z_3)} + \frac{\rho_2 \tau_2 Z_1 Z_3}{(Z_2 - Z_1)(Z_2 - Z_3)} + \frac{\rho_3 \tau_3 Z_1 Z_2}{(Z_3 - Z_1)(Z_3 - Z_2)} \quad \text{(A3.34)}$$

$$k_0 = C_p \cdot \left[\frac{\rho_1 Z_2 Z_3}{(Z_1 - Z_2)(Z_1 - Z_3)} + \frac{\rho_2 Z_1 Z_3}{(Z_2 - Z_1)(Z_2 - Z_3)} + \frac{\rho_3 Z_1 Z_2}{(Z_3 - Z_1)(Z_3 - Z_2)}\right] + I_p \cdot \left[\frac{\rho_1}{(Z_1 - Z_2)(Z_1 - Z_3)} + \frac{\rho_2}{(Z_2 - Z_1)(Z_2 - Z_3)} + \frac{\rho_3}{(Z_3 - Z_1)(Z_3 - Z_2)}\right] \quad \text{(A3.35)}$$

$$k_1 = C_p \cdot Z_1 Z_2 Z_3 \left[\frac{\rho_1}{(Z_1 - Z_2)(Z_1 - Z_3)} + \frac{\rho_2}{(Z_2 - Z_1)(Z_2 - Z_3)} + \frac{\rho_3}{(Z_3 - Z_1)(Z_3 - Z_2)}\right] + I_p \cdot \left[\frac{Z_1 \rho_1}{(Z_1 - Z_2)(Z_1 - Z_3)} + \frac{Z_2 \rho_2}{(Z_2 - Z_1)(Z_2 - Z_3)} + \frac{Z_3 \rho_3}{(Z_3 - Z_1)(Z_3 - Z_2)}\right] \quad \text{(A3.36)}$$

$$k_2 = C_p \cdot Z_1 Z_2 Z_3 \left[\frac{Z_1 \rho_1}{(Z_1 - Z_2)(Z_1 - Z_3)} + \frac{Z_2 \rho_2}{(Z_2 - Z_1)(Z_2 - Z_3)} + \frac{Z_3 \rho_3}{(Z_3 - Z_1)(Z_3 - Z_2)}\right] + I_p \cdot \left[\frac{Z_1^2 \rho_1}{(Z_1 - Z_2)(Z_1 - Z_3)} + \frac{Z_2^2 \rho_2}{(Z_2 - Z_1)(Z_2 - Z_3)} + \frac{Z_3^2 \rho_3}{(Z_3 - Z_1)(Z_3 - Z_2)}\right] \quad \text{(A3.37)}$$

where C_p and I_p are the values of total ion concentration and double ionic strength in the permeate (both known from experiment).

We numerically solved both the system of equations A3.30-A3.31 and the non-linearized Poisson-Boltzmann equation using Matlab™. We varied the values of pore radius and surface-charge density iteratively until the feed concentrations of both Mg^{2+} and K^+ matched the experimental value. These calculations used the bulk diffusion coefficients of ions, namely, $D_{Mg^{2+}} = 0.71 \cdot 10^{-9}\, m^2/s$, $D_{K^+} = 1.96 \cdot 10^{-9}\, m^2/s$ and $D_{Cl^-} = 2.04 \cdot 10^{-9}\, m^2/s$.

REFERENCES

REFERENCES

1. Egueh, A. N. D.; Lakard, B.; Fievet, P.; Lakard, S.; Buron, C. *Journal of Colloid and Interface Science* **2010,** *344*, 221-227.

2. Daiguji, H.; Yang, P. D.; Majumdar, A. *Nano Letters* **2004,** *4*, 137-142.

3. Nishizawa, M.; Menon, V. P.; Martin, C. R. *Science* **1995,** *268*, 700-702.

4. Swaminathan, V. V.; Gibson, L. R.; Pinti, M.; Prakash, S.; Bohn, P. W.; Shannon, M. A. *Journal of Nanoparticle Research* **2012,** *14*, 951-1-951-15.

5. Armstrong, J. A.; Bernal, E. E. L.; Yaroshchuk, A.; Bruening, M. L. *Langmuir* **2013,** *29*, 10287-10296.

6. Yaroshchuk, A. E. *Advances in Colloid and Interface Science* **2008,** *139*, 150-173.

7. Ali, M.; Yameen, B.; Cervera, J.; Ramírez, P.; Neumann, R.; Ensinger, W.; Knoll, W.; Azzaroni, O. *Journal of the American Chemical Society* **2010,** *132*, 8338-8348.

8. Feldoto, Z.; Varga, I.; Blomberg, E. *Langmuir* **2010,** *26*, 17048-17057.

9. Ouyang, L.; Malaisamy, R.; Bruening, M. L. *Journal of Membrane Science* **2008,** *310*, 76-84.

10. Yaroshchuk, A. E. In *Transport properties of nano-porous track-etched membranes in electrolyte solutions*, Nanopores for Bioanalytical Applications: Conference Proceedings, London, 2012; Edel, J.; Albrecht, T., Eds. Royal Society of Chemistry: London, 2012; pp 93-98.

11. Yaroshchuk, A. E. *Advances in Colloid and Interface Science* **2011,** *168*, 278-291.

12. Dresner, L. *Journal of Physical Chemistry* **1963,** *67*, 1635-1641.

13. Dresner, L. *Journal of Physical Chemistry* **1965,** *69*, 2230-2238.

14. Morrison, F. A.; Osterle, J. F. *Journal of Chemical Physics* **1965,** *43*, 2111-2115.

15. Gross, R. J.; Osterle, J. F. *Journal of Chemical Physics* **1968,** *49*, 228-234.

16. Yaroshchuk, A. E. *Journal of Membrane Science* **2000,** *167*, 149-161.

17. Lazzara, T. D.; Lau, K. H. A.; Abou-Kandil, A. I.; Caminade, A.-M.; Majoral, J.-P.; Knoll, W. *ACS Nano* **2010,** *4*, 3909-3920.

18. Adamczyk, Z.; Zembala, M.; Kolasińska, M.; Warszyński, P. *Colloids and Surfaces A: Physicochemical and Engineering Aspects* **2007,** *302*, 455-460.

19. Adamczyk, Z.; Zembala, M.; Warszyński, P.; Jachimska, B. *Langmuir* **2004,** *20*, 10517-10525.

20. Qi, S. R.; Li, W. Y.; Zhao, Y.; Ma, N.; Wei, J.; Chin, T. W.; Tang, C. Y. Y. *Journal of Membrane Science* **2012,** *423*, 536-542.

21. Schwarz, B.; Schönhoff, M. *Langmuir* **2002,** *18*, 2964-2966.

22. Yaroshchuk, A. E. *Advances in Colloid and Interface Science* **1995,** *60*, 1-93.

23. Shilov, V. N. *Colloids and Surfaces A: Physicochemical and Engineering Aspects* **1998,** *142*, 375-379.

24. Zholkovskij, E. K.; Masliyah, J. H.; Shilov, V. N.; Bhattacharjee, S. *Advances in Colloid and Interface Science* **2007,** *134–135*, 279-321.

Chapter 4: Monovalent ion separations utilizing track-etched membranes modified with multilayer polyelectrolyte films

Portions of this chapter were published in JA Armstrong, EEL Bernal, AE Yaroshchuk, and ML Bruening. *Langmuir*, 29 (32), 10287-10296 (2013).

4.1. Introduction

The previous chapter described separations of K^+ and Mg^{2+} or Br^- and SO_4^{2-} using flow through charged nanopores. This chapter focuses on more challenging separations between ions with the same charge. Surprisingly, the same membranes described in chapters 2 and 3 can effect these separations, but the mechanism relies on streaming potentials and differences in ion mobilities,[1] rather than exclusion of divalent ions.[2-4] Again, PEMs provide surface charge,[5] which gives rise to streaming potentials as well as control over the pore diameters. Below, I first describe the separation mechanism, and then provide the procedural details and data for the separations.

4.2. Mechanism for streaming potential-based separation of ions with the same charge

Charged capillaries exclude ions with the same charge to the same extent, so selective transport between two different monovalent ions is not feasible via electrostatic exclusion. However, when the pore surface charge is opposite in sign to the ions of interest, transmembrane streaming potentials enable separation of ions with different electrical mobilities.[6]

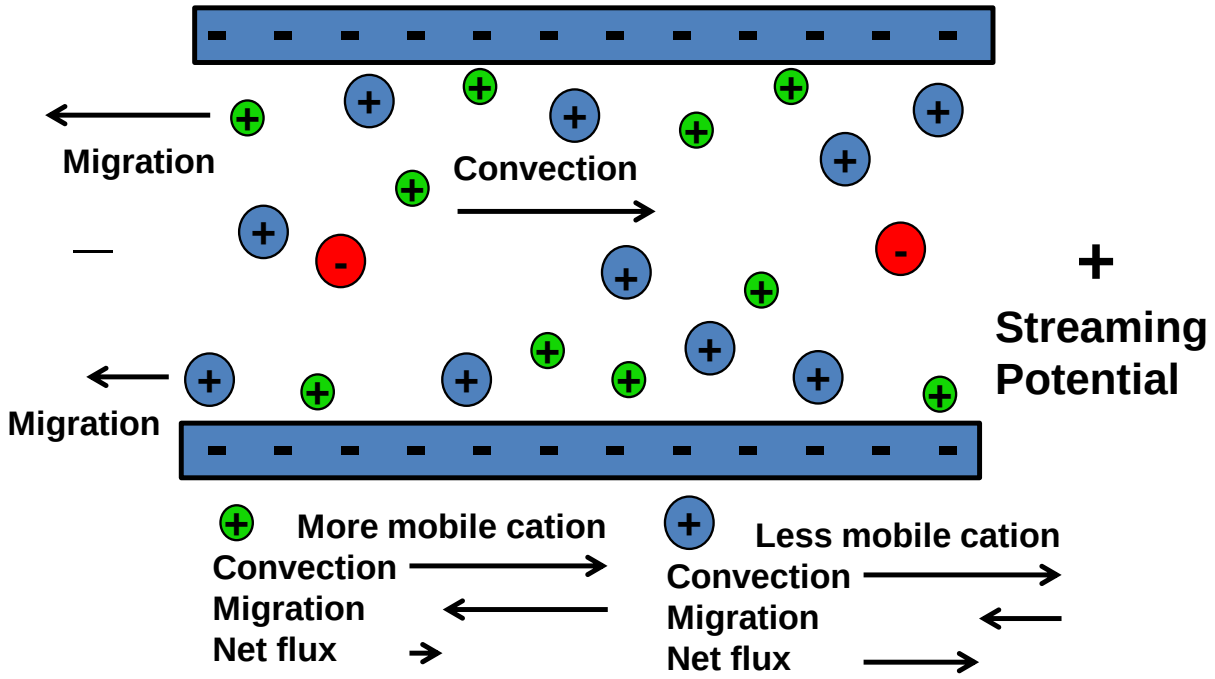

Figure 4.1. Schematic diagram of selective permeation of a less mobile cation during convective flow through a negatively charged nanopore. Partial exclusion of anions from the pore results and pressure-driven flow result in a streaming potential that retards transport of cations, but especially the more mobile cation. This image assumes diffusive transport is negligible.[6]

Consider the separation illustrated in Figure 4.1 where Cs^+ and Li^+ are the more and less mobile cations, respectively. The negatively charged capillary excludes anions and attracts Li^+ and Cs^+ equally. Applying a transmembrane pressure forces the solution to flow through the pore, and thus generates a streaming potential due to excess cations in the double layer. This streaming potential decreases cation transport and enhances anion transport to achieve zero current. Even though the two cations possess the same electrical charge, the difference in mobilities causes Cs^+ and Li^+ ions to traverse the membrane at different rates.[6] (The mobilities of Cs^+ and Li^+ at infinite dilution are 8.0×10^{-4} and 4.0×10^{-4} $cm^2/(V\ s)$, respectively.)[7] The higher rate of electrical migration in the negative direction (i.e. toward the feed side of the membrane)

of Cs^+ compared to Li^+, yields selective transport of Li^+ over Cs^+. The same mechanism also describes selective transport of homovalent anions, although the charge on the membrane, and therefore the sign of the streaming potential, will be reversed. These separations are most effective at low ionic strengths, which give rise to high streaming potentials.

4.3. Separation of ions with the same charge

4.3.1. Membrane preparation and filtration experiments

The 30-nm PCTE membranes used in these studies were modified as described in chapters 2 and 3. Separations of Cs^+ and Li^+ employ $(PSS)_1$-modified 30-nm PCTE membranes, whereas anion separations require positively charged, $(PSS\text{-}PAH)_1$-modified, 30-nm PCTE membranes. Filtration experiments were conducted with the apparatus described in chapter 3.

4.3.2. Li^+/Cs^+ separations in $(PSS)_1$-modified, 30-nm membranes

As mentioned above, streaming potentials resulting from flow through negatively charged membranes should lead to higher rejections of Cs^+ than Li^+. Table 4.1 shows the monovalent cation rejections during dead-end filtration of solutions containing Li_2SO_4 and Cs_2SO_4. For these filtrations, bare and $(PSS)_1$-modified membranes, both of which are negatively charged, give similar monovalent ion rejections, and Li^+/Cs^+ selectivities of ~3.3. We employ divalent (SO_4^{2-}) rather than monovalent counterions to enhance anion exclusion from the membrane and, hence, streaming potentials. The similar behavior of the two membranes is reasonable if SO_4^{2-} exclusion is high in both cases. Moreover, the flow rate is ~50% higher through the bare than the PSS-modified membrane. Higher flow rates will minimize the influence of diffusion, which counteracts the selectivity from electrical migration. Thus, the

higher flow rate through the bare membrane may offset the effect of greater SO_4^{2-} exclusion from the PSS-modified pores.

Membrane	Li^+ Rejection (%)	Cs^+ Rejection (%)	Li^+/Cs^+ Selectivity
Bare	20 ± 13	72 ± 10	3.2 ± 0.9
PSS_1-modified	10 ± 11	72 ± 11	3.4 ± 0.7

Table 4.1. Monovalent ion rejections and Li^+/Cs^+ selectivities during dead-end filtration through bare and PSS_1-modified track-etched membranes (nominal 30 nm pores prior to modification). The feed solutions contained 1.5 mM Li_2SO_4 and 1.5 mM Cs_2SO_4, and the pressure employed during filtration was 414 kPa. The uncertainty values are the standard deviations of a total of 12 permeate measurements on two different membranes.

4.3.3. Br^-/Acetate separations in $(PSS\text{-}PAH)_1$-modified, 30-nm membranes

Similar to the Li^+ and Cs^+ separations described in the previous section, we employ PEM-modified, 30-nm PCTE membranes to separate anions. Figure 4.2 shows the streaming potential mechanism for anion separations. Table 4.2 shows no acetate/Br^- selectivity in the negatively charged bare membrane, but coating the membranes with PSS/PAH leads to a selectivity around 6. In these experiments, the larger (and thus less mobile) acetate ions pass through the membrane at a higher rate than the Br^- ions, as expected. Thus, these experiments confirm the streaming potential-based mechanism of separation. In principle, higher selectivities are possible at higher flow rates, but concentration polarization will limit selectivity at some point.

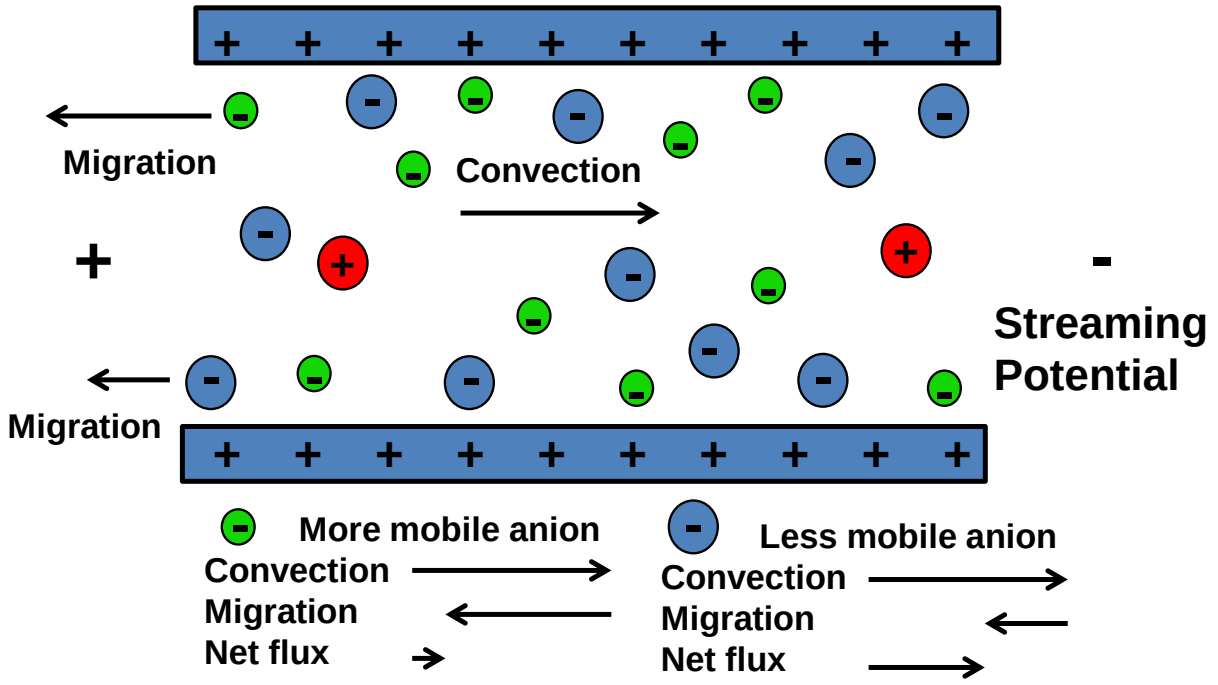

Figure 4.2. Schematic diagram of selective permeation of a less mobile anion during convective flow through a positively charged nanopore. Partial exclusion of cations from the pore results in a streaming potential that retards transport of anions, but especially the more mobile anion. This image assumes diffusive transport is negligible.[2]

Membrane	$Acetate^-$ Rejection (%)	Br^- Rejection (%)	$Acetate^-/Br^-$ Selectivity
Bare	50 ± 18	48 ± 14	1.0 ± 0.1
$(PSS\text{-}PAH)_1$-modified	13 ± 10	80 ± 11	5.7 ± 2.8

Table 4.2. Monovalent ion rejections and $acetate^-/Br^-$ selectivities during dead-end filtration through bare and $(PSS\text{-}PAH)_1$-modified, track-etched membranes (nominal 30 nm pores prior to modification). The feed solutions contained 0.5 mM $Mg(Acetate)_2$ and 0.5 mM $MgBr_2$. The pressure employed during filtration was 414 kPa. The uncertainty values are the standard deviations of a total of 12 permeate measurements on two different membranes.

4.4. Summary

Separations of ions with the same charge in modified, 30-nm PCTE membranes give rise to cation selectivities of ~3 and anion selectivities of ~6. We employed divalent counterion salts

(e.g. SO_4^{2+}-salts for cations and Mg^{2+}-salts for anions), as they should give rise to higher streaming potentials. Although the ion-transport selectivities are not as high as the selectivities described in chapter 3, the separations are considerably more difficult. Tuning separations for either cations or anions occurs very simply through polyelectrolyte adsorption (i.e. PEMs terminated with polyanions enable separation of Cs^+ and Li^+, whereas PEMs terminating with polycations enable separation of Br^- and acetate). Higher selectivities may result from either greater surface charge densities or faster flow rates, but concentration polarization will limit selectivity.

REFERENCES

REFERENCES

1. Yaroshchuk, A. E. In *Transport properties of nano-porous track-etched membranes in electrolyte solutions*, Nanopores for Bioanalytical Applications: Conference Proceedings, London, 2012; Edel, J.; Albrecht, T., Eds. Royal Society of Chemistry: London, 2012; pp 93-98.

2. Hollman, A. M.; Bhattacharyya, D. *Langmuir* **2004,** *20*, 5418-5424.

3. Krasemann, L.; Toutianoush, A.; Tieke, B. *Journal of Membrane Science* **2001,** *181*, 221-228.

4. Harris, J. J.; Stair, J. L.; Bruening, M. L. *Chemistry of Materials* **2000,** *12*, 1941-1946.

5. Decher, G., Fuzzy Nanoassemblies: Toward Layered Polymeric Multicomposites. *Science* **1997,** *277* (5330), 1232-1237.

6. Armstrong, J. A.; Bernal, E. E. L.; Yaroshchuk, A.; Bruening, M. L., Separation of Ions Using Polyelectrolyte-Modified Nanoporous Track-Etched Membranes. *Langmuir* **2013,** *29* (32), 10287-10296.

7. Vanýsek, P., Ionic Conductivity and Diffusion at Infinite Dilution. In *CRC Handbook of Chemistry and Physics.* , 93rd ed.; Haynes, W. M., Ed. CRC Press: Boca Raton, FL, 2012-2013; pp 5-77-5-79.

Chapter 5: Monovalent ion separations using cross-flow filtration through microfluidic glass discs and an applied transmembrane electrical potential

5.1. Introduction

Chapter 4 demonstrated a selectivity of ~5 between monovalent ions during dead end-filtration through charged membrane pores. Those separations relied on the formation of a streaming potential to selectively reject ions with higher electrophoretic mobilities (Figure 4.1). As equation (5.1) shows, the electrophoretic velocity, v_i, is the product of the

$$v_i = \mu_i E \tag{5.1}$$

electrophoretic mobility, μ_i, and the electric field, E. Assuming a uniform electric field, because $\mu_{K^+} \cong 2\mu_{Li^+}$, the K^+ rejection, R_{K^+}, should be about twice the Li^+ rejection, R_{Li^+}. (Rejection should be proportional to the electrophoretic velocity counter to the transmembrane solution flux.) Equation 5.2 implies that selectivity will increase as the ion rejections increase and $(1 - R_{K^+})$ becomes small.

$$\alpha_{K^+}^{Li^+} = \frac{1-R_{Li^+}}{1-R_{K^+}} \tag{5.2}$$

Unfortunately, high rejections require high streaming potentials, which occur at high flow rates that give rise to concentration polarization.

Whenever rejection occurs, concentration polarization appears because convection continually brings ions to the membrane surface, and only some of these ions pass through the membrane (Figure 5.1). The concentration of a given ion will increase at the membrane surface to achieve a steady state, such that the net flux to the membrane surface is equal to the net flux through the membrane (equation 5.3). In equation 5.3, for a given ion,

$$J_{conv}^{soln} + J_{diff}^{soln} + J_{migr}^{soln} = J_{conv}^{mem} + J_{diff}^{mem} + J_{mig}^{mem} \tag{5.3}$$

J_{conv}^{soln}, J_{diff}^{soln}, and J_{migr}^{soln} are the convective, diffusive and electromigration fluxes, respectively, in the feed solution, and J_{conv}^{mem}, J_{diff}^{mem}, J_{mig}^{mem} are the corresponding terms in the membranes. Attainment of high selectivities in CcE requires that $J_{mig}^{mem} >> J_{diff}^{mem}$ because the diffusive and electromigration fluxes will occur in opposite directions and both of these fluxes are proportional to ion mobility. However, the high flow rates that increase streaming potentials to enhance J_{mig}^{mem} also enhance J_{diff}^{mem} through concentration polarization.

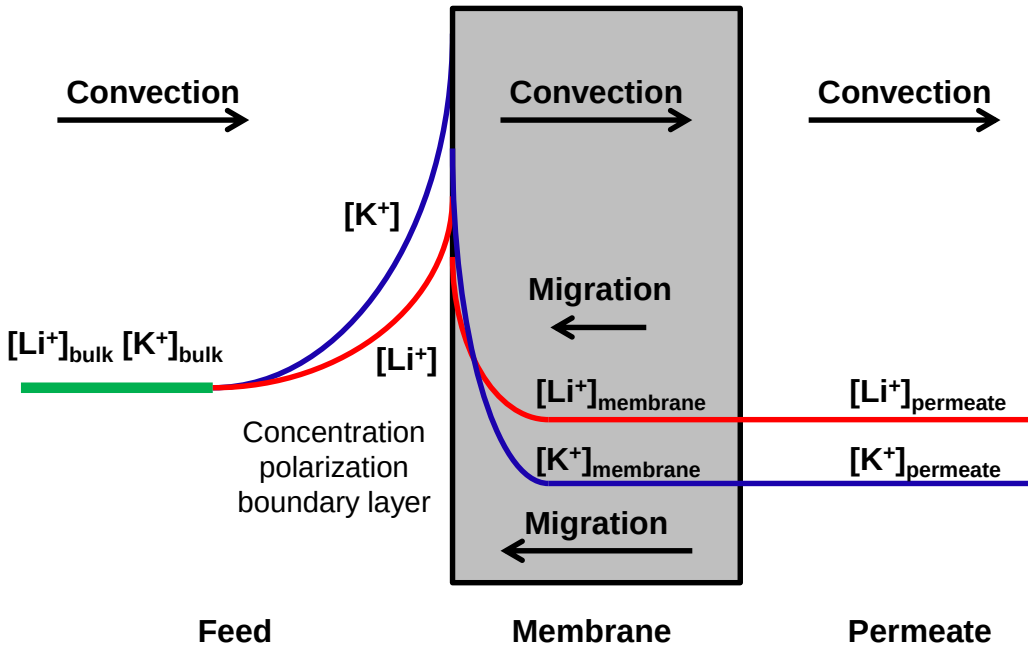

Figure 5.1. Qualitative concentration profiles of Li^+ and K^+ during continuous separation via CcE. The ions possess the same concentrations in the bulk (feed) solution, but the difference in their electrical mobilities gives rise to higher Li^+ concentrations within the membrane, and selective permeation of Li^+ over K^+. The electrical potential at the permeate side of the membrane is positive with respect to the feed side.

Cross-flow filtration (Figure 5.2), wherein feed solution flows across the membrane surface (i.e. tangentially), decreases the thickness of the stagnant layer near the membrane

surface, and thus limits concentration polarization by increasing the rate of diffusion away from the surface toward the feed. Lower ion concentrations at the membrane surface should also limit

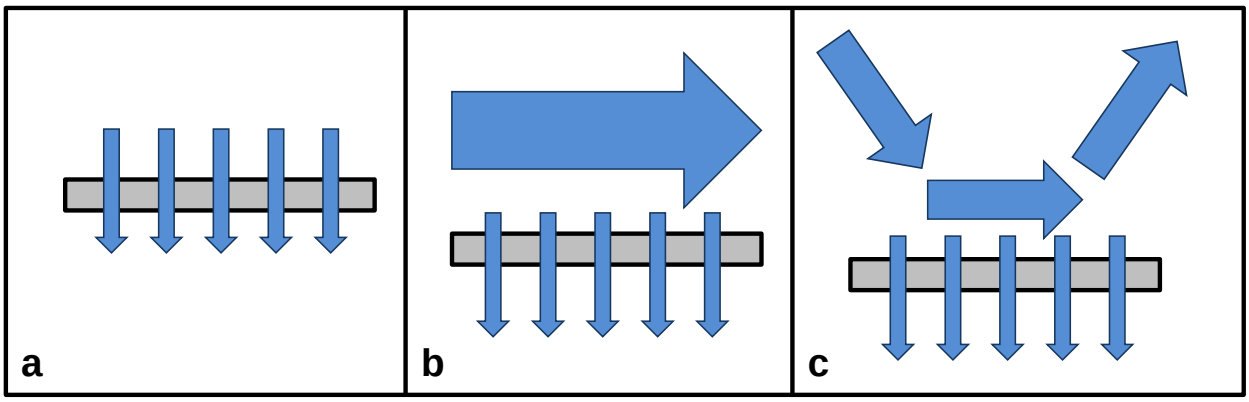

Figure 5.2. Dead-end (a) and cross-flow (b) filtration modes. The gray rectangle represents the membrane, and the blue arrows represent pressure-driven solution flow. Dead-end filtration utilizes pressure to flow solution through the membrane, and rejected species accumulate on the top surface of the membrane. Cross-flow filtration passes solution across the top surface of the membrane, and a fraction of this fluid goes through the membrane. The tangential flow limits the thickness of the boundary layer at the membrane surface to limit accumulation of rejected species. Figure (c) shows the approximate flow pattern in the device used in this work, where flow impinges on the membrane surface, flows across the membrane, and leaves the cell at an angle to the surface. This configuration gives a complicated cross-flow pattern.

transmembrane diffusion (toward the permeate), which is proportional to the concentration gradient. However, the low thickness (< 10 μm) and small pore diameters of PCTE membranes still make it difficult to achieve negligible transmembrane diffusive flux to obtain high ion-transport selectivities. Moreover, these membranes are quite fragile and cross-flow filtration is difficult to apply.

This chapter describes our efforts to enhance the separation of monovalent ions through application of transmembrane potentials during cross-flow filtration through membranes made from fused glass capillaries. These membranes offer several advantages over PCTE membranes. First, the thickness is 2-3 mm, which should reduce the transmembrane concentration gradient to decrease diffusion. Second, the 5-μm pore size in these membranes leads to high convective fluxes to decrease the significance of diffusion compared to convection. However, the rapid

flow in these membranes requires a strong electric field to reject ions (e.g. ≥100 V/cm), which we can only achieve through applied potentials. The mechanism in these separations is thus essentially countercurrent electrophoresis (Figure 5.3).[1-4] The convective velocity of Li^+ and K^+ ions is the same, while the (counterflow) electrical migration velocity of K^+ is ~twice that of Li^+. The flow of solution through the micropores combined with electrical migration gives rise to

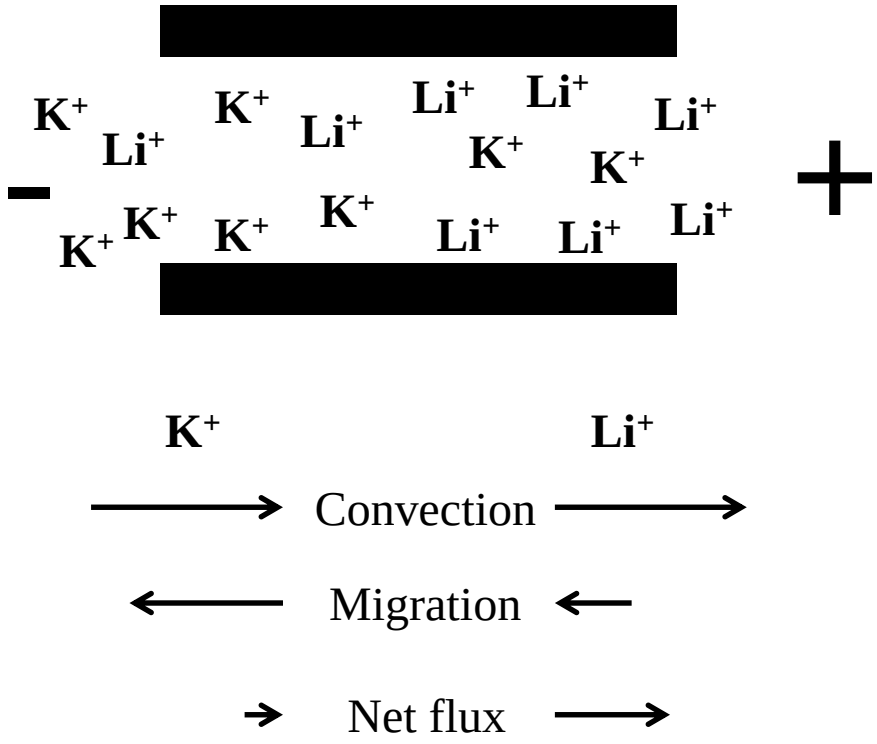

Figure 5.3. Separation of monovalent ions with an electrical potential applied across a micropore. The flow of feed solution (convection) moves the Li^+ and K^+ through the pore at the same rate. The transmembrane potential decreases transport of the more-mobile K^+ twice as much as it decreases the less-mobile Li^+. Flow through the pore gives rise to a permeate solution enriched in Li^+ and depleted of K^+, and, thus, the micropore provides $\alpha_{K^+}^{Li^+}$. Low salt concentrations (e.g. 0.25 mM Li_2SO_4 and 0.25 mM K_2SO_4) minimize the electrical current, which will reduce heat generation and changes in pH near electrodes. Anions are omitted for clarity.

permeate solution enriched in Li^+ over K^+, providing $\alpha_{K^+}^{Li^+}$. In principle, the highest selectivities in these separations will occur when the electromigration of K^+ is essentially balanced by convection to give nearly zero flux. At the potentials required for such separations, Li^+-rejection will also be substantial (~50% if the mobility of the two ions differ by a factor of 2). Application of even higher potentials should further increase rejection of Li^+, and decrease its recovery.

These separations require a membrane with a uniform pore size that gives consistent transmembrane solution velocities across the membrane area. Otherwise, a potential that gives high rejection in one pore may give moderate rejection in another. Additionally, the pore size should be 5 μm or less, so radial diffusion can keep solutions in pores well mixed and overcome the dispersion of velocities in laminar flow.[5-7] As we show below, the glass capillary membranes from Collimated Holes, Inc.™ fulfill this requirement. Thus, this chapter investigates Li^+/K^+ separations in glass capillary membranes as a function of cross-flow, transmembrane potential and transmembrane flow rate.

5.2. Materials and methods

5.2.1. Microporous glass capillary discs

Borosilicate glass capillary discs were purchased from Collimated Holes, Inc. (CHI). The discs possess ~50% porosity, 2-3 mm thicknesses (787-0010, 2 mm, and 787-0011, 3 mm), and a diameter of 30 mm. As mentioned above, the well-defined micropores with 5-μm diameters provide uniform transmembrane flow velocity profiles and still allow radial mixing within the pore to overcome the distribution of convective velocities that result from laminar flow. Figure 5.4 illustrates the high aspect ratio (height:pore diameter) and narrow pore-size distribution of the disc. The disc's pores are 5 μm in diameter, and the disc height is 2-3 mm

(indicating aspect ratios of ~500). The discs were fabricated via a proprietary technique, but they are essentially a homogeneous collection of capillary tube bundles.

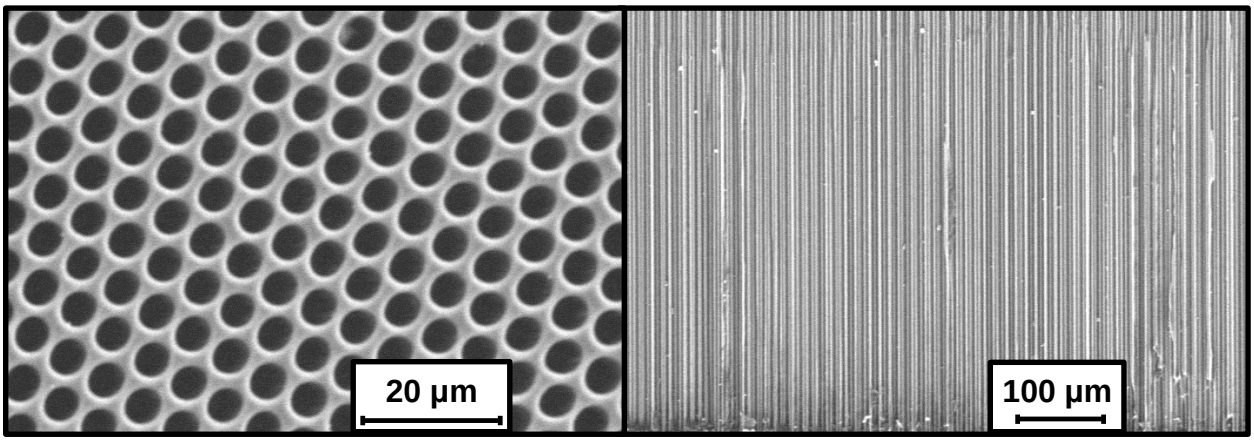

Figure 5.4. CHI microporous glass discs possess uniform pore sizes (<5% dispersion in diameters). The micrograph at left shows the honeycomb-like structure and pore uniformity in a top-down view. The image at right shows a cross-section of the same disc after fracturing. Images were obtained via a JEOL 6610LV scanning electron microscope (the glass discs are uncoated).

5.2.2. Fabrication of a cross-flow filtration cell that allows application of transmembrane electrical potentials

The design of the cross-flow filtration cell (see Figure 5.5) was adapted from a previously described nanofiltration cell.[8] The cell, which was fabricated by Michigan State University's machine shop, houses the CHI glass disc and contains permeable electrodes for applying electrical potentials. Nylon shells provide a housing for connectors and electrode assemblies.

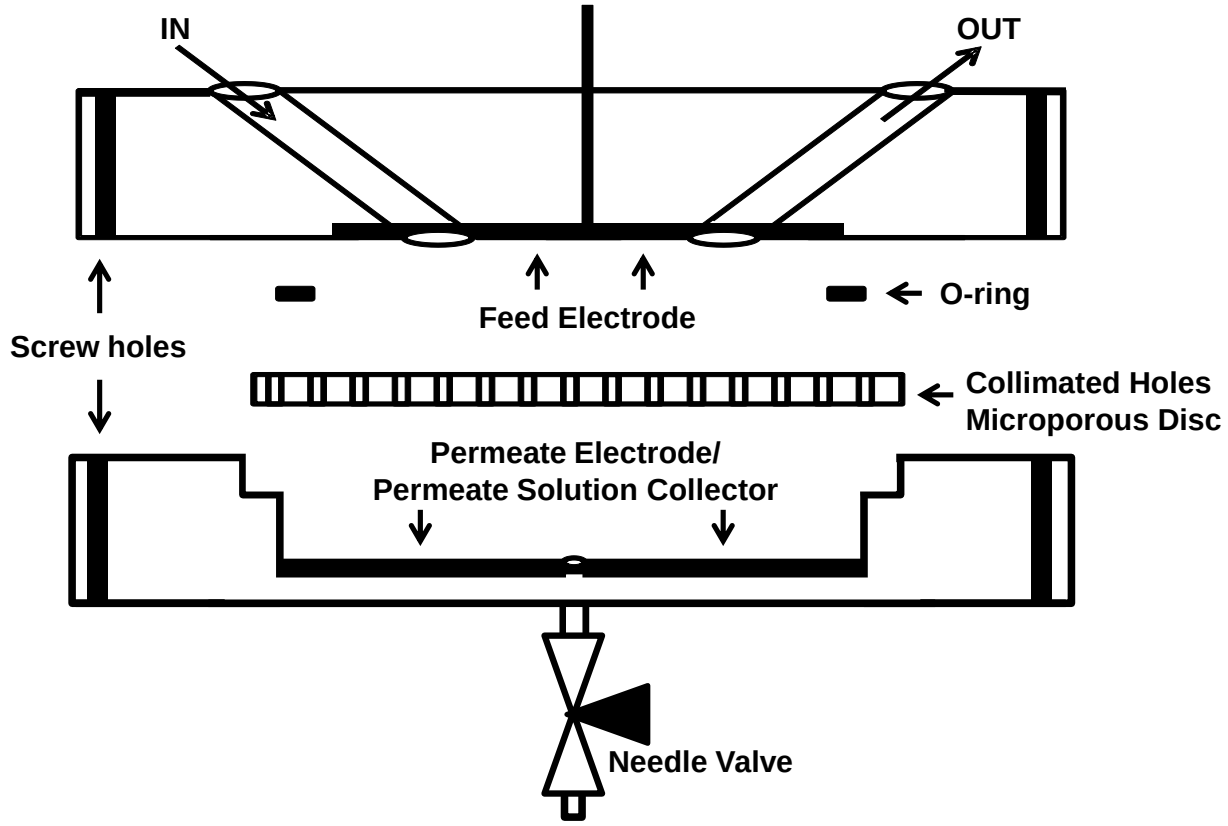

Figure 5.5. Top and bottom section of a cross-flow filtration cell. The top (feed) section has two cross-flow ports (inlet and outlet) traversing the stainless steel disc electrode; all of which reside in a Nylon shell. The bottom (permeate) section is similar to the top, but only has a single flow outlet. The permeate collector is welded to a steel drainage tube, which allows collection of the permeate. A needle valve attached to the drainage tube regulates flow rate. The CHI glass disc is sandwiched between the cell halves, and sealed to the top half with an O-ring and four screws through the Nylon shells.

The glass disc sits on the ledge in the lower half of the cell, underneath an O-ring that seals the membrane to the top half of the assembly.

The feed electrode (Figure 5.6) allows pressurized solution to flow across the top of the membrane, while also providing a nearly homogeneous electrode surface. Conversely, the permeate electrode is simply a steel disc with a centralized hole. A hollow steel tube welded to

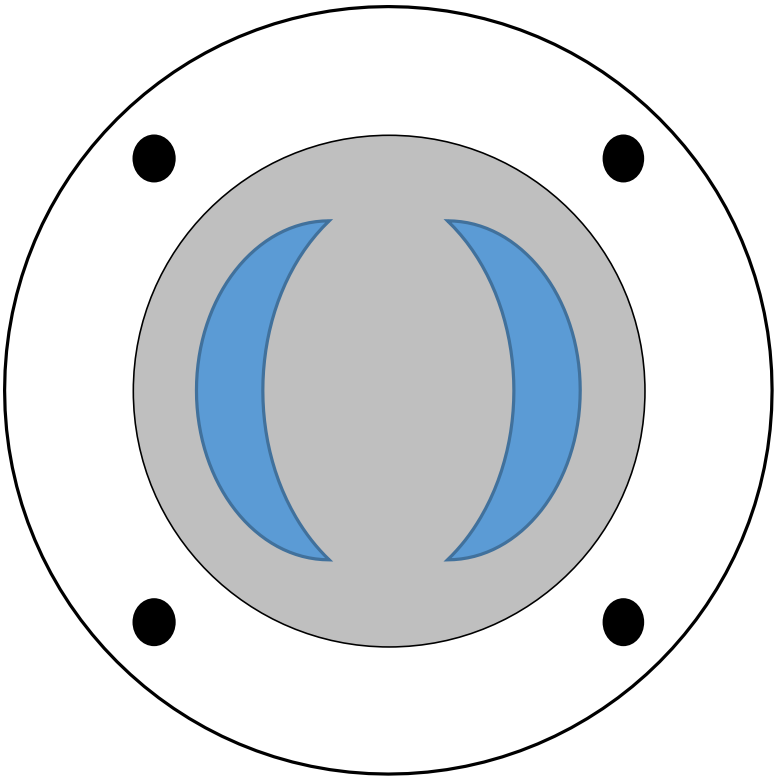

Figure 5.6. Schematic of the (feed) electrode/flow jet assembly, located inside the top of the cross-flow cell. Blue crescents represent the flow ports. Flow exits the inlet port (left side) at an angle (not shown) to help prevent regions of stagnant flow. The outlet port (right side) is not angled, but open and moon-shaped, to minimize resistance to flow. The black circles represent the screw holes that fasten together the cell halves.

the bottom electrode collects the permeate solution. Both electrode assemblies are press-fit into their respective cell-half outer assemblies.

5.2.3. Apparatus for cross-flow filtration with an applied potential

The cell containing the CHI disc is inserted into a filtration system, as shown in Figure 5.7. Feed solution flows from the pressurized feed tank, through a circulating pump, and across the filtration cell. Using a DC power supply (not shown in Figure 5.7), up to -500 V (feed electrode minus the permeate electrode) is applied across the disc while the solution circulates

across the feed surface and partly permeates the disc. The retentate solution is recirculated, while permeate solution is gathered for analysis. Rejection analyses are completed as described

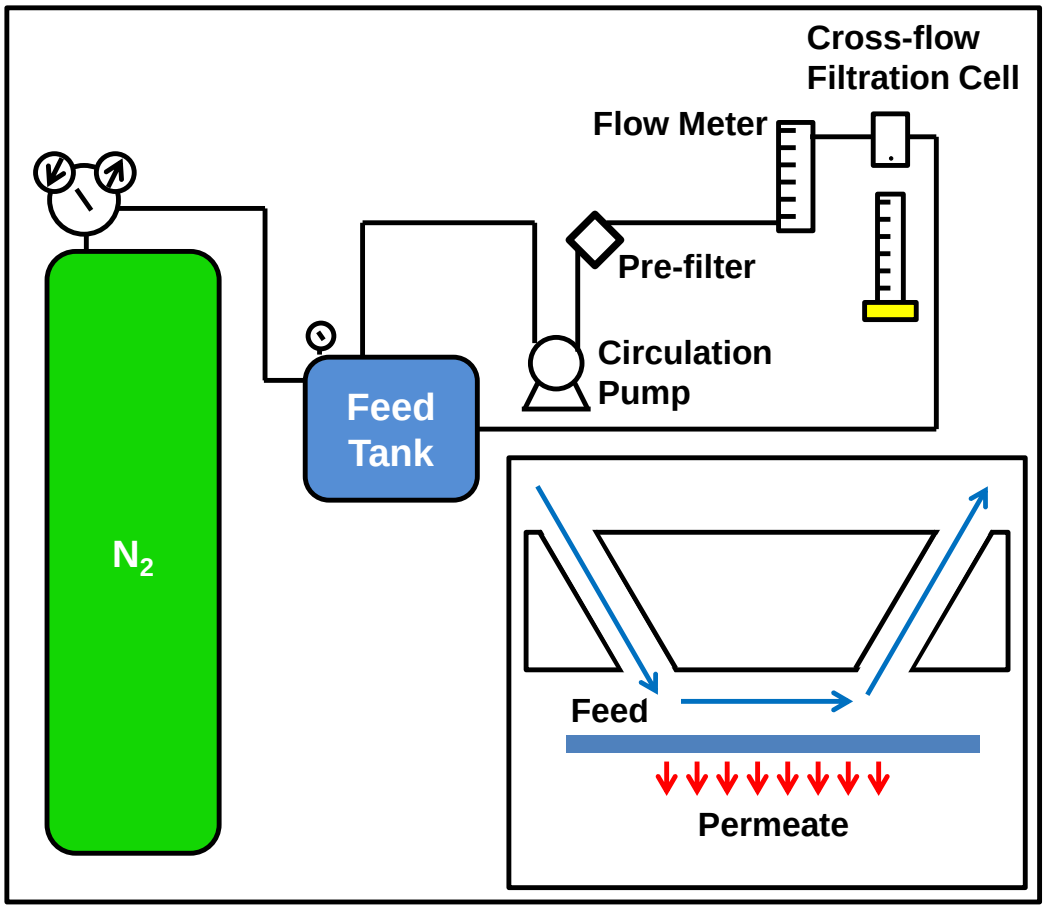

Figure 5.7. Schematic drawing of the cross-flow filtration system. A pressurized feed solution goes through a circulating pump, then through a prefilter (to remove particles >100 µm), and is measured with a flow meter. Upon exiting the flow meter, the solution enters the filtration cell, flows across the top of the membrane contained within the cell, and exits back to the feed tank. The inset shows the feed solution's path through the cell. A transmembrane pressure drives feed solution through the membrane, while the cross-flow cell ensures the feed solution is constantly replenished; thereby limiting concentration gradients that form once filtration takes place.

in chapters 3 and 4. An ammeter (not shown) is connected in series with the power supply.

5.2.4. Chemicals

The feed solution contains Li_2SO_4, K_2SO_4, and 4-(2-Hydroxyethyl)piperazine-1-ethanesulfonic acid (HEPES). Tetrabutylammonium hydroxide (TBA-OH) was used to adjust the feed solution to pH 7. All chemicals were used as purchased from Fisher Scientific. Low ionic strength feed solutions were employed to limit the current required for high rejections. A zwitterionic, low conductivity buffer (0.06 mS/cm at 200 mM)[9] was used to limit buffer electrophoresis in an effort to ensure the presence of buffer throughout the system and to keep the electric field homogeneous throughout the system.

5.2.5. Cross-flow separations under a transmembrane electrical potential

Cross-flow separations with an applied potential were conducted in the homebuilt system shown in Figures 5.5 and 5.7. The system pressure ranged from 30-210 mbar (N_2), and the feed tank was filled with 4 L of 0.25 mM Li_2SO_4, 0.25 mM K_2SO_4, in 15 or 20 mM HEPES buffer. The solution pH was adjusted to 7 with TBA-OH. Particulates >100 μm were removed via a prefilter (Mott Corp.) in the filtration system. The glass disc was placed inside of the filtration cell, and sealed between cross-flow feed and dead-end permeate cell-halves (see Figure 5.5). The distance between the electrodes is ~6 mm, and the O-ring exposes 6.16 cm^2 of membrane area. Aliquots of 20 mL were taken from the feed solution for analysis, both before and after each experiment. Separations were initiated as described in section 5.2.3. After removing air from the system, and allowing the feed solution to freely flow through the disc, an electrical potential was applied via an external power supply. Permeate collection commenced ~5 minutes after the potential was applied. Permeate solutions were weighed on an analytical balance to

provide flow rates. Cation concentrations were determined using atomic absorption spectroscopy, as described in chapter 3.

5.3. Results and Discussion

5.3.1. K^+/Li^+ separations utilizing applied potentials in a cross-flow filtration cell

Preliminary experiments used 15 mM HEPES buffer and -20 V (feed electrode minus permeate electrode), and gave strong pH shifts (e.g. the permeate solution pH was ~2) within the filtration cell. This suggests that the buffer was overwhelmed by proton generation at the permeate electrode. Additionally, rust-like fouling covered the disc's pores, thereby reducing the flow rate (e.g. >50% decrease in permeability over the course of the 4 h experiment). Figures 5.8 and 5.9 show the extent of the fouling.

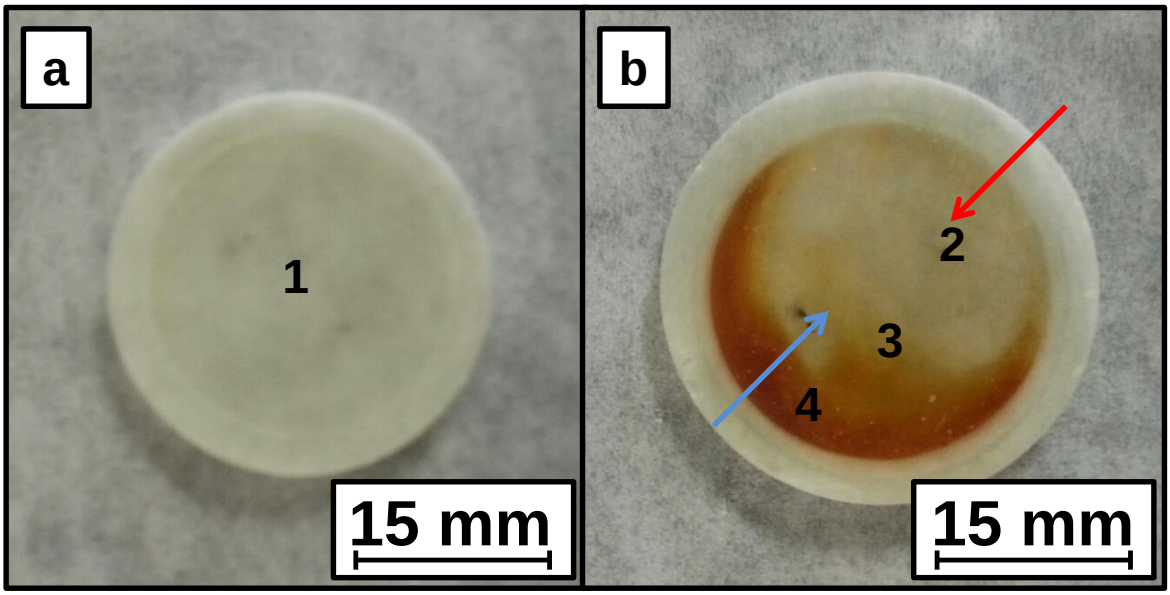

Figure 5.8. Photographs of the feed-solution side of the CHI disc (a) before and (b) after cross-flow filtration with an applied potential of -20 V for 1.5 h. The foulant appears most strongly in regions near, but not directly underneath, the outlet port (blue arrow), and least near the inlet port (red arrow). Nitric acid solution (50% v/v) removes the fouling.

The asymmetry of the fouling suggests that there is severe nonuniform flow on the feed side of the disc, as well as a stagnant region surrounding the outlet flow jet. The rust may form due to generation of OH^- at the negative electrode on the feed side of the membrane. In an effort to limit fouling, I increased the HEPES concentration to 20 mM (again adjusted to pH 7 with TBA-OH) and the cross-flow rate from ~3-15 L/h.

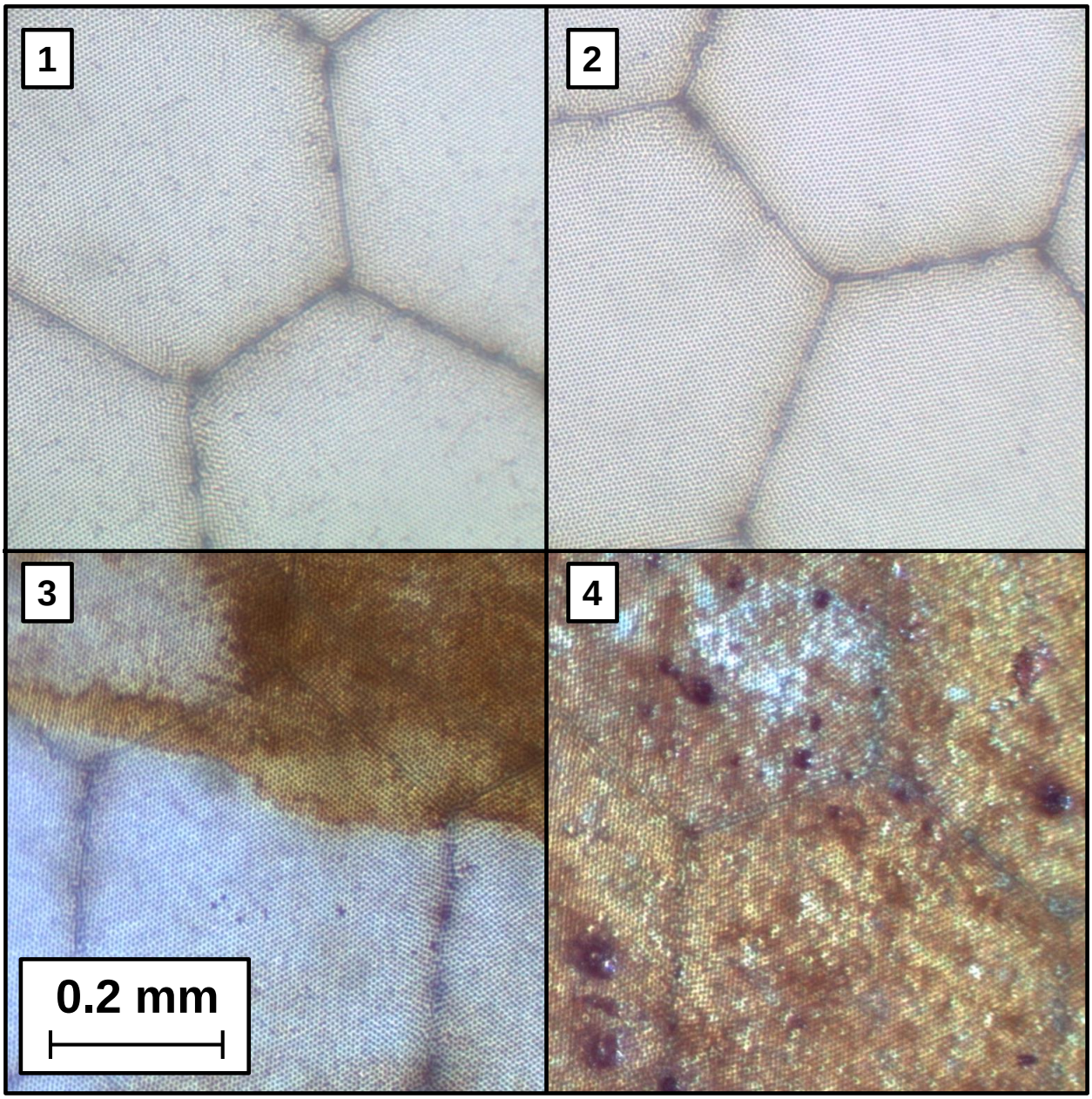

Figure 5.9. Light microscope images of the CHI disc (1) before and (2-4) after cross-flow filtration under an applied potential of -20 V for 1.5 h. The numbers on the photographs in Figure 5.8 correspond to the expanded regions in the micrographs in this figure. Micrographs 2-4 illustrate the difference between regions of the disc that experience high and low flow (i.e. cross-flow). Image (2) is a relatively clean portion of the fouled disc, directly underneath the inlet flow jet. Image (3) is from an area where the foulant begins to appear. This region is between the flow jets, but ~5 mm from the disc's center. Image (4) shows a heavily fouled portion of the disc, just beyond the area underneath the outlet flow jet, which is presumably the area of the disc with the most stagnant flow. The disc regions most fouled are those areas furthest from the inlet flow jet, likely indicating that much of the feed side of the disc has stagnant flow.

In these studies, we conducted an initial cross-flow filtration and subsequently doubled the pressure and voltage (simultaneously). As Table 5.1 shows, doubling the pressure doubled the flow rate, indicating a similar permeability for both filtration conditions (i.e. fouling is not

P (bar)	E (V)	I (mA)	Li^+ rejection (%)	K^+ rejection (%)	$\alpha_{K^+}^{Li^+}$	Permeability (cm^3/cm^2 h bar)
0.07	-20	8.5 ± 1.1	51.8 ± 3.4	67.7 ± 4.9	1.51 ± 0.14	220 ± 35
0.14	-40	16.5 ± 1.6	50.4 ± 9.9	66.7 ± 9.7	1.54 ± 0.20	212 ± 53

Table 5.1. Filtration results of 0.25 mM Li_2SO_4 and 0.25 mM K_2SO_4 feed solution, with 20 mM HEPES buffer (TBA-OH pH-adjusted). Doubling the pressure and voltage now provides similar rejections of both ions, as well as a constant permeability.

severely blocking the pores). The doubling of current after doubling the potential also indicates similar permeabilities (conductivity does not change), and the combination of doubled voltage and doubled transmembrane flow rate does not significantly change the rejection of either ion, as expected for the constant ratio of current to transmembrane flow rate. Moreover, after disassembling the filtration cell, the disc showed no significant visible fouling. Remarkably, only a 25% increase in buffer concentration was sufficient to overcome the fouling. Indeed, the average permeate pH was 6.2 ± 0.6 at the higher buffer concentration. The low $\alpha_{K^+}^{Li^+}$ values, however, show the need for further investigation and development to improve selective transport.

I employed a higher voltage (-60 V) in an attempt to enhance $\alpha_{K^+}^{Li^+}$. The ion and buffer concentrations were the same as in Table 5.1. Figure 5.10 shows rejection versus normalized current (i.e. the current divided by flux, where flux is the flow rate divided by the exposed membrane external area of 6.16 cm^2) for this higher voltage separation, which lasted >6 hours.

Over the course of the experiment, the current passing through the membrane dropped from ~25 mA to ~5 mA, due to the loss of permeability. For example, at 0.07 bar the first 5 permeates during which -60 V was applied demonstrated an average permeability of 318 ± 107 $cm^3/(cm^2$ h bar), and the last 5 permeates (~4 hours later)with the same applied voltage showed

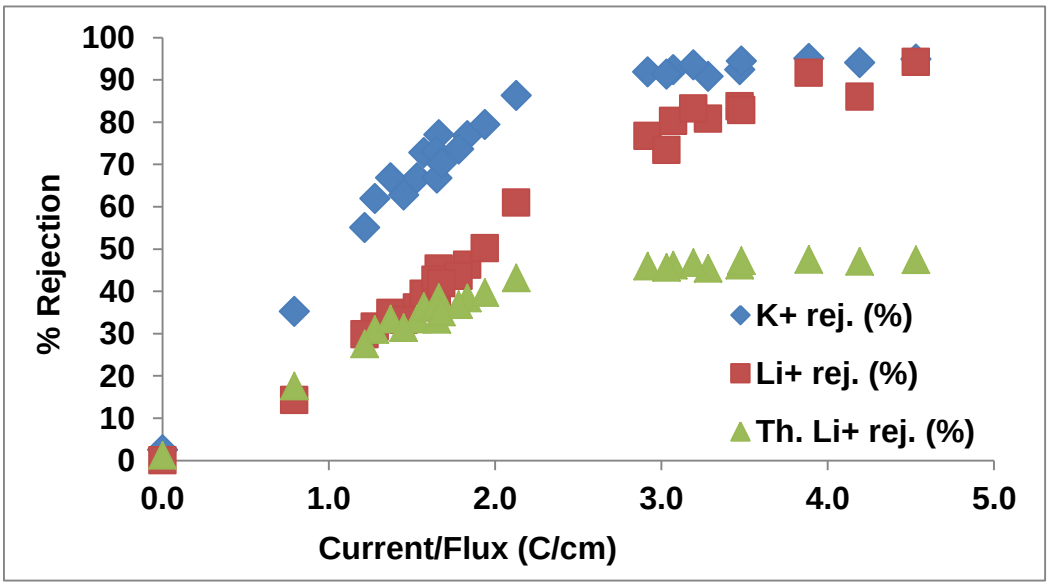

Figure 5.10. Plot of K^+ rejection (blue diamonds) and Li^+ rejection (red squares) as a function of current normalized by flux area (C/cm), during cross-flow filtration of 0.25 mM Li2SO4, 0.25 mM K2SO4, in 20 mM HEPES buffer with a feed electrode – permeate electrode potential of 60 V. The figure also shows the theoretical Li^+ rejection (green triangles), which is simply half of the K^+ rejection, based on the ratio of the mobilities of the two ions.

permeabilities of 3 ± 1 $cm^3/(cm^2$ h bar). I adjusted the pressure between 0.03 and 0.14 bar to keep the flow rate >0.5 mL/min, but current decreased with time to give a lower value of current/flux in later measurements. The current/flux ratio should reflect the ratio of convective velocity to the electrophoretic velocity if the fraction of current carried by the individual ions does not change. The loss of permeability, and thus current, are likely results of significant

fouling of the glass disc. After removing the disc from the cell, fouling similar to that shown in Figures 5.8 and 5.9 appeared on the disc's surface.

Despite the fouling, with K^+ rejections < 80%, the Li^+ rejection is about half that for K^+, as we hoped. Moreover, the rejection increases with the ratio of current to flow rate. This is reasonable, as higher ratios suggest higher ratios of electrophoretic to convective transport. However, permeate solutions with K^+ rejections >90% show Li^+ rejections that are higher than the anticipated $\left\{\frac{R_{K^+}}{2}\right\}$. In fact, Li^+ rejections start to converge with K^+ rejection at ~90% K^+ rejection. Unfortunately, this prevents attainment of the high $\alpha_{K^+}^{Li^+}$ values that we hoped to see. The highest selectivities obtained in this experiment were ~3.

The convergence of K^+ and Li^+ rejections at high flow rates suggest that there are regions of the membrane with a low electric field, a high concentration polarization, or a high flow rate such that rejection is low in those regions. Given the nonuniformity of fouling, a region with high concentration polarization that gives rise to a limit in rejection is certainly possible. Overcoming this challenge will require a completely redesigned filtration cell. The pore size appears very uniform across the membrane surface, so we do not think that the flow rate through the membrane is non-uniform. It is possible that the electric field is not uniform, but we would expect that higher currents/flow rate would eventually yield a rejection near 100% if the challenge is achieving higher electric field in specific regions. Thus, future work may need to focus on redesigning the filtration cell.

High current to flow rate ratios also give rise to a buffer depletion. Though the HEPES buffer is zwitterionic, and therefore of low mobility, a combination of strong electric fields and low flow rates may lead to proton and hydroxide generation at the permeate electrode that overwhelms the buffer. The permeate pH values range from 7.0 at a current to flux ratio of 1.22

C/cm to 5.0 for a current to flux ratio of 4.55 C/cm. Protons are much more mobile than the buffer, so pH gradients in the system will give nonuniform electric field that may lead to limited rejections. Increasing the buffer concentration may help to overcome this problem, but higher buffer concentration also increases conductivity to give higher current and more proton generation.

5.4. Conclusions

Cross-flow filtration with an applied potential gives R_{K^+} values that are about twice those for R_{Li^+}, when R_{K^+} < 80%. This agrees well with rejection based on electrophoresis of the two ions. However, rejections of Li^+ and K^+ ions begin to converge at rejections >90%, which prevents realization of $\alpha_{K^+}^{Li^+} > 3$. Moreover, R_{K^+} plateaus and does not approach 100%, even when the current to flux ratio increases. This may stem from regions of stagnant cross-flow that give rise to high concentration polarization. Images of fouled membranes are consistent with regions of stagnant flow near the cross-flow outlet. Thus, future work should focus on developing new cell designs that yield more uniform cross flow. Buffer depletion may also lead to non-uniform electric fields. However, we already employ a low-conductivity buffer to limit current, and increasing buffer concentration will increase current and thus may not overcome buffer depletion.

REFERENCES

REFERENCES

1. Culbertson, C. T.; Jorgenson, J. W. *Analytical Chemistry* **1994,** *66*, 955-962.

2. Chankvetadze, B.; Burjanadze, N.; Bergenthal, D.; Blaschke, G. *Electrophoresis* **1999,** *20*, 2680-2685.

3. McLaren, D. G.; Chen, D. D. Y. *Electrophoresis* **2003,** *24*, 2887-2895.

4. Gobie, W. A.; Ivory, C. F. *Journal of Chromatography A* **1990,** *516*, 191-210.

5. Rose Jr, D. J.; Jorgenson, J. W. *Journal of Chromatography A* **1988,** *447*, 117-131.

6. Jorgenson, J. W.; Lukacs, K. D. *Analytical Chemistry* **1981,** *53*, 1298-1302.

7. Leonard, E.; Jørgensen, S. *Annual Review of Biophysics and Bioengineering* **1974,** *3*, 293-339.

8. Stanton, B. W.; Harris, J. J.; Miller, M. D.; Bruening, M. L. *Langmuir* **2003,** *19*, 7038-7042.

9. Kelly, A. E.; Ou, H. D.; Withers, R.; Dötsch, V. *Journal of the American Chemical Society* **2002,** *124*, 12013-12019.

Chapter 6: Summary and future work

6.1. Summary

The primary goal of this work was to better understand ion transport through nanoporous and microporous membranes, with an eye toward controlling selective ion transport. Progressing from the separation of monovalent and divalent ions (e.g. K^+ and Mg^{2+}) to more difficult separations of monovalent ions (e.g. Li^+ and Cs^+), this work demonstrated selective ion transport through several different mechanisms.

Chapter 1 presented an overview of the various methods currently used to separate ions (e.g. electrophoresis and membrane-based separations). Membrane separations provide an attractive alternative to other techniques, primarily because they often operate continuously rather than in a batch mode. Additionally, tailoring of surface chemistry can optimize membranes for a desired separation. The research described in this dissertation exploited both of these assets of the membranes. In addition to continuous operation over several hours, PEM-modified membranes separated several different types of ions after appropriate surface modifications. For example, a polyanion-capped (i.e. negatively charged) membrane pore enables separation of anions of different valence. The same membrane can separate monovalent cations, although via a different mechanism. Simple adsorption of an additional polycation layer in the aforementioned membranes enables separation of cation of different valence, as well as monovalent anions.

Chapter 2 described the deposition of PEMs in nanoporous, track-etched membranes. PEM adsorption affords control over both pore size and surface charge, thereby ensuring that the electrical double layer exists throughout the nanopores to enable ion separations. A single

(PSS/PAH) bilayer within 30-nm pores gives rise to monovalent/divalent ion selectivities comparable to those resulting from several (PSS/PAH) bilayers in 50-nm pores. The adsorption of fewer bilayers (within the 30-nm pores) saves time and conserves resources during membrane preparation. Subsequent chapters employed these membranes to separate various monovalent ions.

Chapter 3 described the separation of monovalent and divalent ions. Initially, we adsorbed positively-charged PEMs in 50-nm PCTE membranes, and employed these membranes to separate K^+ and Mg^{2+} with a selectivity of ~10. However, 30-nm membranes with $(PSS/PAH)_1$ films are easier to prepare and equally selective. As expected, at high ion concentrations, the rejections of both K^+ and Mg^{2+} decrease because the double layer becomes thinner. However, solutions with < 5 mM ionic strength exhibited essentially 100% Mg rejections (the Mg^{2+} concentration in the permeate was below the method detection limit). Moreover, K^+ rejections increased on the presence of Mg^{2+}, which we attribute to the Mg^{2+}-adsorption within the PEM and increased surface charge. Finally, we separated Br^- and SO_4^{2-} with a PSS_1-modified, 30-nm PCTE membrane, to validate the exclusion mechanism for anions. The average Br^-/SO_4^{2-} selectivity was 3.4 ± 0.8 for 0.5 mM NaBr and 0.5 mM Na_2SO_4. The low selectivity in this case likely stems from a relatively large pore.

Membranes modified with PEMs can also separate monovalent ions via a streaming potential mechanism, which is the subject of chapter 4. In these separations, flow through a negatively charged membrane yields a positive (permeate) streaming potential. This positive potential retards the transport of a more mobile cation to a greater extent than transport of a less mobile ions. Thus, $(PSS)_1$-modified, 30-nm PCTE membranes enabled Li^+ and Cs^+ separation, whereas $(PSS\text{-}PAH)_1$-modified membranes separated acetate$^-$ and Br^-. Cation selectivities were

~3 for 1.5 mM Li_2SO_4 and 1.5 mM Cs_2SO_4 solutions, while anion selectivities were ~6 for 0.5 mM $Mg(Acetate)_2$ and 0.5 mM $MgBr_2$ solutions. The streaming potential method gave only modest selectivities and required low ion concentrations. Chapter 5 described our efforts to employ an applied potential to enhance selectivities in monovalent ion separations. We designed a cross-flow filtration cell with porous electrodes to both decrease boundary layer thicknesses and concentration polarization and allow application of large electric fields. With the appropriate potentials, the cell afforded some separation of K^+ and Li^+, but the average selectivities were ~3. Moreover, the rejection of both ions plateaued near 90% at sufficiently high current to flow rate ratios. Buffer depletion or nonuniform cross-flow or electric fields may lead to membrane areas with low rejection and prevent high selectivities.

6.2. Future work

Future monovalent ion separations with applied potentials should aim to achieve a more uniform cross-flow to minimize local concentration polarization. Moreover, cross-flow on the permeate side of the membrane may help to overcome buffer depletion. As in chapter 3 with the K^+ and Mg^{2+} separations, theoretical simulations may help to elucidate issues such as coupled transport, non-uniformities in the electric field, and flow pattern issues associated with the cell design. The section below describes preliminary efforts to create a dual cross-flow cell.

6.2.1. Fabrication of a dual cross-flow (DCF) filtration cell

The dual cross-flow (DCF) cell applies the design of the feed side of the prior cell (chapter 5) onto the permeate side (Figure 6.1). A rotary pump on the feed side of the DCF cell circulates buffered feed solution across the top membrane surface, whereas a peristaltic pump on

the permeate side passes fresh buffer solution across the bottom of the membrane and the anode, where the solution is then collected for analysis. Importantly, the feed solution recirculates, but the permeate solution passes across the bottom surface of the membrane and is collected to provide ion transport data as a function of time. To avoid too great a dilution of the permeate for subsequent analysis, the flow rate on the permeate side is much lower than that of the feed side. The separation mechanism is the same as described in chapter 5 (i.e. CcE).

Using drafting software and 3-dimensional printing, I designed the DCF cell frame and flow paths. Once the frame was printed, electrodes similar those used in the previous cell's feed side were installed into both halves of the DCF cell. Again, a Collimated Holes, Inc.™ (CHI) capillary disc was the preferred membrane. The membrane is sealed between the cell halves, while feed solution circulates through the feed cell-half and buffer flow across the permeate cell-half. The porous electrodes allow potentials to be applied. Figure 6.1 diagrams the DCF cell.

The DCF cell was installed in a filtration system similar to the one described in chapter 5. The only differences were the addition of a permeate buffer reservoir and a peristaltic pump for

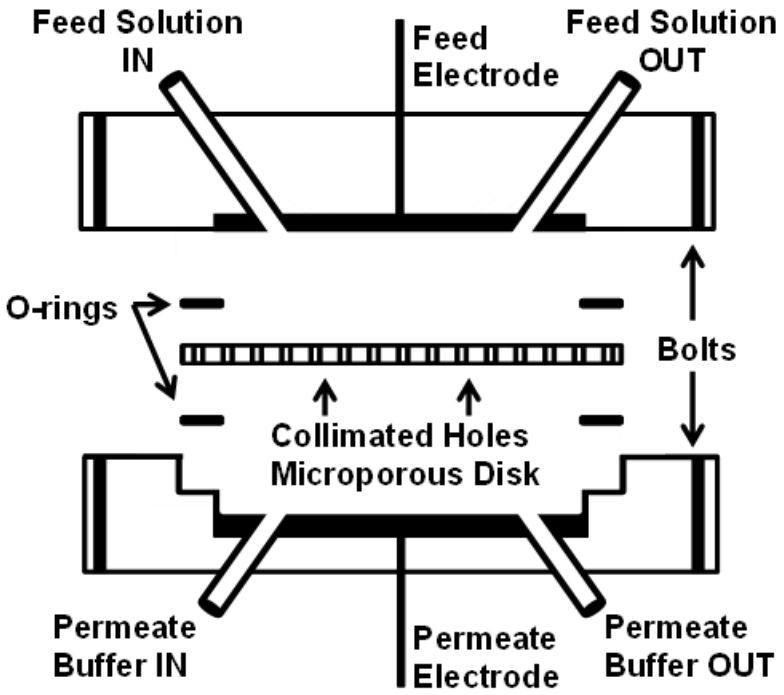

Figure 6.1. Diagram of the top and bottom sections of a DCF cell. The top (feed) section has two cross-flow ports (inlet and outlet) traversing the stainless steel disc electrode; all of which is contained within a plastic shell. The bottom (permeate) section is nearly a mirror image of the top half, but with the addition of a step in the shell wall to support the CHI glass disc. The disc is sandwiched between O-rings, and the DCF cell halves are sealed together via 4 bolts around the perimeter of the cell.

Pumping buffer solution through the permeate cell-half (Figure 6.2). An external power supply provides up to -500 V across the membrane.

The DCF cell may solve buffer depletion issues; however, its obvious disadvantage is the dilution of the permeate. The K^+/Mg^{2+} separations described in chapter 3 challenged the instrumental detection limits for ion rejections >90%. Therefore, moving to system in which the permeate ions are immediately diluted may cause issues with analysis for rejections >90%, especially so for high permeate buffer flows. Unfortunately, I only competed very preliminary

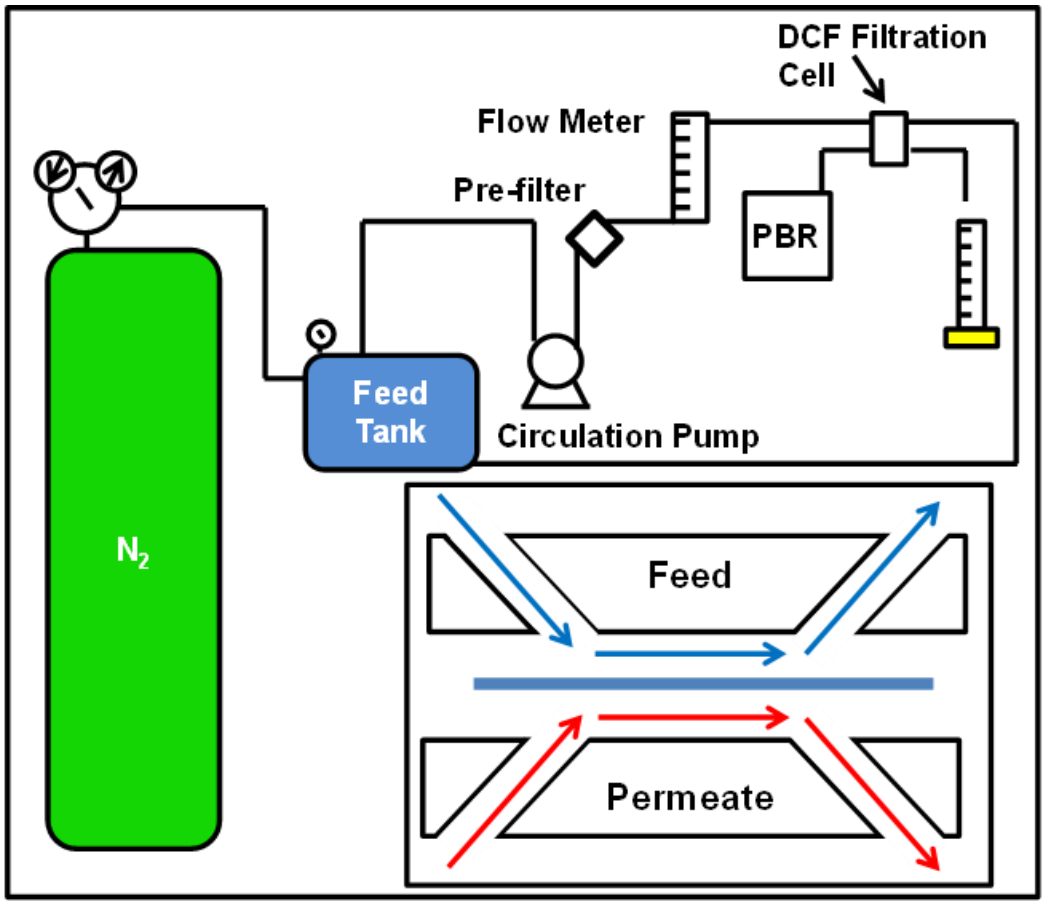

Figure 6.2. Diagram of the filtration system used with the DCF cell. A pressurized feed solution goes through a circulating pump, then through a prefilter (to remove particles >100 µm), and is measured with a flow meter. Upon exiting the flow meter, the solution enters the filtration cell, flows across the top of the membrane contained within the cell, and exits back to the feed tank. Similarly, permeate buffer solution is pumped from the permeate buffer reservoir (PBR), across the membrane's permeate surface, and exits into a permeate collection vessel. The inset shows the paths of the feed solution (blue) and permeate buffer (red) through the cell. A transmembrane drives feed solution through the membrane while the DCF cell ensures the feed solution and permeate buffer are constantly replenished; thereby minimizing concentration gradients that form during filtration.

work with the DCF filtation system and have no data to report. However, future work in ion separations will likely focus upon the DCF cell, as well as on theoretical ion-transport studies.